Light-Matter Interactions in Transition-Metal Dichalcogenides

by

Rahul Gogna

A dissertation submitted in partial fulfillment
of the requirements for the degree of
Doctor of Philosophy
(Applied Physics)
in The University of Michigan
2021

Doctoral Committee:

Professor Hui Deng, Chair
Assistant Professor Parag Deotare
Professor Stephen Forrest
Professor L. Jay Guo
Professor Mackillo Kira

Rahul Gogna
rgogna@umich.edu
ORCID iD: 0000-0001-9984-194X

ACKNOWLEDGEMENTS

First, I want to thank Professor Hui Deng for being an excellent advisor over the last several years. Her support and guidance throughout the process of this degree has been invaluable, and I'm very grateful for the range of interesting projects she's given me the opportunity to work on during my time here.

I would also like to thank my Doctoral Committee members: Assistant Professor Parag Deotare, Professor Stephen Forrest, Professor Jay Guo and Professor Mackillo Kira for taking the time to be on my committee and providing valuable feedback and suggestions for improving this dissertation.

I also have to thank my lab-mates, who have made working in the group a fun and productive experience. I particularly have to thank Long Zhang, who patiently taught me how to perform optical experiments, and who collaborated closely with me on a number of the projects which will be discussed in this dissertation. I'd also like to thank Zhaorong Wang and Jason Horng for their mentorship as well. It has been a joy to work alongside the current and graduated members of the group: Jiaqi Hu, Eunice Paik, Glenn Leung, Yingyu Lai, Tim Chou, Seonghoon Kim, Tyler Hill, and Adam Katcher. I've also enjoyed the short time I've worked with the newest group members, Lingxiao Zhou, Adam Alfrey, Yuze Liu, and Nathan Lydick, and I wish them the best of luck on their future research in the group.

Finally, I want to thank my family, especially my Mom and Dad, for always being there for me and helping and supporting me throughout this process. Their constant

support and encouragement in everything that I do has been incredibly important to me, and I wouldn't be where I am today without them.

TABLE OF CONTENTS

LIST OF FIGURES

Figure

ABSTRACT

Transition Metal Dichalcogenides (TMDCs) have recently become a very popular topic of research due to their wide range of novel optical properties. Many of these materials feature excitons with large oscillator strengths and binding energies, making them an attractive choice as a material for exploring exciton-polariton physics. TMDCs are also very versatile, and can be combined with each other to form arbitrary combinations of materials that can have interesting, tunable properties that change depending on how the heterostructures are constructed. In this thesis, we will look at several different projects concerning light-matter coupling in TMDCs.

First, we numerically calculate the properties of photonic crystals designed to exhibit guided-mode resonances for the purposes of achieving strong coupling with evanescently coupled group VI TMDC monolayers. We detail the optimization of these devices, and show that particular attention needs to be paid to the thickness of the device to ensure maximum exciton-photon coupling. We also demonstrate that the in-plane patterning makes these devices suitable for on-chip integration, and that they have more interesting dispersion properties compared to standard optical cavities. These numerical results of strong coupling are corroborated by experimental results which show that this type of platform can indeed support polaritons at both cryogenic and room temperatures, making this the first demonstration of all-dielectric photonic crystal polaritons created with TMDCs.

This is followed by numerical results detailing a dual-band photonic cavity designed to have independently tunable resonances, for coupling to multiple different emitters in a single layer of active material, in contrast to standard types of cavities whose modes are not independently tunable. The cavity combines a traditional Fabry-Pérot type cavity with a guided-mode resonance type cavity, and the two modes both have electric field distributions that strongly couple to the active material at the center of the cavity, a result which is generally not possible with standard optical cavities.

Then, we present experimental results showing highly valley-polarized emission from hBN encapsulated $MoSe_2/WSe_2$ heterobilayers. The emission has two prominent peaks, one of which has the standard optical selection rule and one of which has a flipped optical selection rule, and both exhibit high valley polarization. These results are presented alongside some numerical calculations about the electronic and optical properties of TMDC heterobilayers.

Finally, we present experimental results, supported by numerical calculations, which demonstrate for the first time that the group VII material ReS_2 is capable of supporting self-hybridized polaritons, which manifest as a splitting of the exciton absorption. The high background index of the material results in an effective optical cavity that is formed by the ReS_2/Air and ReS_2/substrate (Au or Sapphire) interfaces. We fully characterize the polarization resolved absorption, and present transfer matrix calculations which are in excellent agreement with the experimental results, making this the first demonstration of self-hybridized polaritons in group VII materials.

CHAPTER I

Introduction

The ability to control and manipulate light is critical to modern technology. Major advances in light sources, such as the invention of LEDs and lasers, have led to revolutionary advances in modern technology, with far-reaching applications such as energy-efficient consumer lighting, medical treatments (such as vision restoration), industrial-grade precision laser cutting, and high-bandwidth communication, to name a few. Other types of optoelectronic devices, such as solar cells, offer a promising path forward to the generation of renewable energy.

These revolutionary technologies have all been enabled by progress in the fundamental research on new materials, optics and photonics. Given the importance of generating and controlling light to most of these modern-day technologies, there is always a continued interest in advancements of optical materials which can further enable lower power consumption, smaller device footprints, and novel applications which aren't currently practical. A group of materials that has recently garnered a large amount of interest as a promising system for a wide range of optoelectronic applications are two-dimensional materials, specifically the transition metal dichalcogenides (TMDCs).

1.1 Two-Dimensional Semiconductors

In 2010, it was discovered that monolayer MoS_2 is a direct bandgap semiconductor[71], which attracted an enormous amount of attention due to it's potential as an optical material. This, and the other TMDCs, have been shown to have a variety of properties, such as large exciton binding energies and oscillator strengths, that make them attractive candidates for exploring exciton physics at room temperature[56]. In addition to their suitability for room-temperature operation, other interesting properties, such as valley-polarized emission[93], make them a very attractive material to study, and a significant amount of work has been done on studying these materials in order understand and make use of their diverse range of optical properties that are not commonly found in other semiconductors.

These materials are held together in the out-of-plane direction by weak van der Waals forces, which allows them to be easily exfoliated and integrated with arbitrary photonic structures as well as other two-dimensional materials. The ability to integrate these materials with arbitrary photonic structures allows for an unprecedented level of flexibility compared to conventional semiconductors, which generally do not have this level of easy integration, since factors such as lattice matching must be considered when designing the devices.

Integrating these optical materials with photonic devices is interesting for several reasons: it can allow us to produce essential nanophotonic components such as nanolasers, it allows us to modify and tune the properties of the photonic structure (for example, by inducing a phase shift in the underlying optical mode of a waveguide), and finally, it allows us to explore interesting coupled light-matter states such as exciton-polaritons.

A variety of different photonic devices integrated with TMDCs have been demonstrated to date, many of which take advantage of not only the ease of integration but also the additional interesting optical properties of the TMDCs. For example, it has been demonstrated[33] that a single monolayer of WS_2 integrated with a silver nanowire (acting as a waveguide) can serve as a direction coupler, where the helicity of the incident light can be used to control which direction the emission of the WS_2 monolayer couples to, with one circular polarization being coupled to one direction, and the opposite polarization coupling to the other direction. Beyond this, the ease of integration can enable the development of practical optical devices, such as nanolasers. This has been demonstrated in several different configurations, for example in[91] where the photonic cavity was an L3 photonic crystal defect cavity. The defect cavity was fabricated, and the monolayer was simply exfoliated on top in order to couple it to the confined mode of the photonic crystal. Lasing has also been demonstrated using a TMDC monolayer integrated into a whispering gallery mode resonators[92]. In addition to lasing with intralayer excitons, it can also be demonstrated with interlayer excitons[64], where the relevant excitonic state is an interlayer exciton formed between the two layers in a heterobilayer. This type of laser was demonstrated using a photonic crystal, similar in design to the one we will explore later in this thesis for a different application of establishing strong coupling. TMDCs have also been coupled into integrated photonic circuits, such as waveguides coupled to microring resonators[87], and integrated Mach-Zehnder interferometers[18].

Combining multiple TMDCs into heterostructures further opens up the possibilities for engineering the properties of these materials. For example, structures such as moiré heterobilayers have been predicted to be one way of creating tunable optical properties, such as tunable interlayer excitons[90]. By varying the different proper-

ties of the heterostructure, such as the type of materials used and the twist angle between them, a range of different properties can be realized which aren't available in the monolayers alone.

1.2 Exciton-Polaritons

A particularly interesting direction which has attracted a lot of excitement is the prospect of creating exciton-polaritons in TMDCs, with the eventual goal of achieving Bose-Einstein condensation at room temperature. Exciton-polaritons are a hybridized system of an exciton strongly coupled to a photon[19], which are capable of supporting a diverse range of phenomena such as BEC-enabled low-threshold lasing[42][20][10], all-optical control of quantum fluids[73], and designer lattices with customized properties, such as topological states[45]. Most work on polaritons has used more traditional materials, but there has been a significant amount of work done on exciton-polaritons in TMDCs in recent years, particularly with demonstrating strong coupling in a variety of different materials coupled to different types of cavities[50, 95, 49, 21, 83, 8]. These polaritons have been demonstrated at both low temperatures and at room temperature. The cavities which are typically used for strong coupling have several drawbacks, as they generally are Fabry-Pérot type cavities which require either an open-cavity configuration, which has reduced coupling strength and is bulky for practical applications, or a closed-cavity configuration, which can risk damaging the material. In addition, some of these cavities are made with metals which provide enhanced field confinement relative to dielectric mirrors at the cost of increased losses, which can be detrimental to the device performance (particularly when considering the eventual goal of achieving condensation). A cavity which fully takes advantage of the properties of TMDCs would allow for easy

integration without requiring additional growth after transfer, while simultaneously allowing for strong enough coupling to establish polaritons at room temperature. It should also be all-dielectric, to enable low-losses operation compared to plasmonic structures. Finally, it is always useful to have additional tunability in shaping the polarization and dispersion properties of the optical mode, beyond what can be accomplished in a standard Fabry-Pérot cavity.

The work which has been done on polaritons in two-dimensional materials demonstrates that these materials are easily integrated with a wide variety of photonic structures in order to enter the strong-coupling regime, but the goal of achieving room-temperature condensation has proved difficult. It was only this year that a group first demonstrated condensation at room temperature using WS_2 [98]. This represents a big step forward in this field, and points towards to possibility of enabling demonstrations of many of the useful properties of BECs in polaritons at room temperature.

The cavities which have been looked at in the literature typically focus on coupling a single optical mode to a single excitonic state in the material, but due to the fact that these materials often support several different excitonic states with a variety of different energy spacings (in addition to the extra states which can be created by coupling multiple materials together into heterostructures), it is also possible to use cavities designed specifically for the purpose of coupling to two states at once, if both the frequency and electric field distribution of the cavity can be simultaneously controlled for two modes. While this is typically difficult to do with standard optical cavities, it is possible to realize such a structure by integrating multiple types of cavities into a single hybrid device that supports resonances that originate from more than one physical process, such as a Fabry-Pérot type mode for one resonance,

and a guided-mode resonance for the second.

In addition, the realm of polaritronic physics in TMDCs has mostly been restricted to group VI TMDCs: MoS_2, $MoSe_2$, WSe_2, and WS_2. There are, however, a large number of TMDC materials with interesting optical properties that fall outside the category of group VI materials, such as the group VII materials $ReSe_2$ and ReS_2, in which polaritronic physics has not yet been deeply explored. This is an interesting system to look at for polaritronic physics because the polaritons will inherit the unique underlying properties of the excitons which are not found in other types of TMDCs, such as a pair of linearly polarized non-degenerate states and highly-visible Rydberg states, which could pave the way to applications which aren't possible with the group VI materials.

A large part of this thesis will be about our efforts to expand the range of possible polariton systems that can be studied in TMDCs by designing and measuring polaritons using cavities and materials which go beyond the usual choice of group VI monolayers coupled to Fabry-Pérot cavities, with the goal of enabling new types of interesting applications and phenomena to be explored.

1.3 Outline of Thesis

This thesis is organized as follows: first, we will review the relevant background on transition metal dichalcogenides in chapter 2. Then, we will review light-matter coupling in semiconductors in chapter 3, specifically focusing on the coupling of excitons to cavity photons and the strong-coupling regime. Following this, we will explore the design of photonic crystals for strong-coupling to monolayer transition metal dichalcogenides, a novel platform for polaritons which is particularly suitable for TMDCs. We will present both computational designs as well as experimental ver-

ification that establishes these photonic crystals as a viable platform for polaritons, with many benefits over traditional cavity designs. Then we will look at the designs of dual-band cavities which have added flexibility over traditional cavity designs, and which are capable of coupling to multiple excitonic states at once while simultaneously maintaining a confined field distribution at the material location, a task which is difficult to do with traditional optical cavities. This is followed by experimental measurements of the valley-polarized emission and theoretical calculations of the electronic and optical properties of TMDC heterobilayers. Finally, we will experimentally and computationally demonstrate the existence of self-hybridization in ReS_2 flakes, where the flakes of material act as optical cavities which modify the excitons optical signature, resulting in a splitting of the underlying exciton peaks.

CHAPTER II

Transition Metal Dichalcogenides

2.1 Introduction

One of the most exciting discoveries of the past decade for solid-state physics has been the discovery of two-dimensional semiconductors. In 2010, it was reported that the transition metal dichalcogenide (TMDC) MoS_2 was a direct-bandgap semiconductor when mechanically exfoliated into monolayers[71], which made it the first two-dimensional material reported which had compelling optical properties. Prior to this, other two-dimensional materials had been discovered, but had limited usefulness in terms of their optical properties. The most well-known example is graphene, a two-dimensional arrangement of carbon atoms, which was discovered to be able to be easily experimentally synthesized via mechanical exfoliation in 2004[40]. Graphene is a very interesting material in its own right, but lacks many properties which would make it a particularly useful optical material. In particular, it is a semi-metal[1], i.e. it has no bandgap.

Following the discovery of monolayer MoS_2, there has been a large amount of interest in exploring the space of TMDCs, and two-dimensional materials more generally, which have a variety of properties that makes them a testbed for exploring problems in condensed matter physics, and a potentially useful class of materials for

developing next-generation photonic and optical technologies. TMDCs span a broad range of materials, any material of the form MX_2, where M is a transition metal and X is a chalcogen. Here we will primarily be interested in the group VI and group VII TMDCs, where the transition metal is from group VI (Mo and W) or group VII (Re). In the following sections we will review the properties of both groups of materials.

2.2 Group VI TMDCs

2.2.1 Structural and Electronic Properties

The arrangement of atoms in a typical group VI TMDC monolayer is shown in Fig. 2.1. The atoms are arranged in a hexagonal lattice, and are bound out-of-plane by weak van der Waals forces. This is a key feature which allows for the material to be easily mechanically exfoliated in order to isolate individual monolayers of the material, as well as for the individual monolayers to be combined in arbitrary combinations to form heterostructures, without have to worry about any practical considerations which would be required when creating heterostructures of more conventional semiconductors, such as lattice matching[30].

The electronic band structure for these materials features an indirect bandgap in their bulk phase, which changes to a direct bandgap when thinned to a monolayer [71] (although there is some controversy over how strictly true this is in some materials. For example, in WSe_2 it has been suggested that the band gap is actually indirect with a transition at the Q point of the conduction band when the monolayer is unstrained [38]).

The direct bandgaps are located at the K/K' points in the Brillouin zone, and feature a spin-orbit splitting at the K/K' points, with the valence band splitting being particularly large in the WX_2 materials, on the order of 0.5 eV[56]. The band

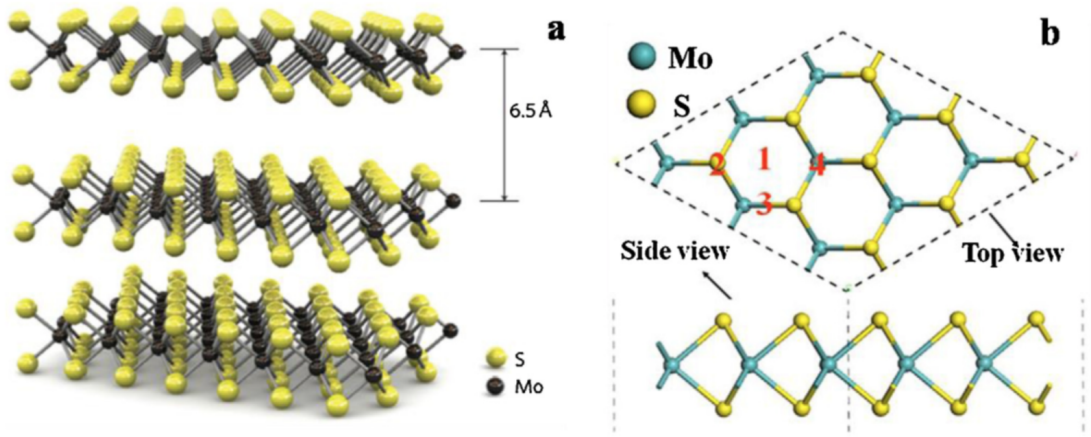

Figure 2.1: (a) A schematic showing the crystal structure of bulk MoS_2, with the individual constituent monolayers clearly visible (b) a top view and side view of a monolayer, showing the hexagonal crystal structure. Reproduced from [35].

structure of these materials can be tuned experimentally by applying strain, either by dynamically straining it[4], or by exfoliating it onto a strain-inducing structure, such as a nanopillar array. These changes modify the band structure of these materials, and can be used to tune their optical properties, such as the exciton emission energy.

2.2.2 Optical Properties

The group VI materials have a variety of interesting optical properties. These include the plethora of quasiparticle states, such as neutral excitons, charged excitons (trions), and biexcitons[56]. The neutral excitons have been the main source of interest for these materials, and even just this type of exciton has a diverse range of properties. These excitons can form between different bands, forming the so-called A and B excitons, and depending on the spins of the bands in question can be either optically dark or bright[57]. One factor which makes these neutral excitons particularly different from other materials is their large binding energies, typically on the order of 100 meV, which is much higher than excitons in many conventional semiconductors such as popular III-V materials like GaAs[60], allowing for the excitons

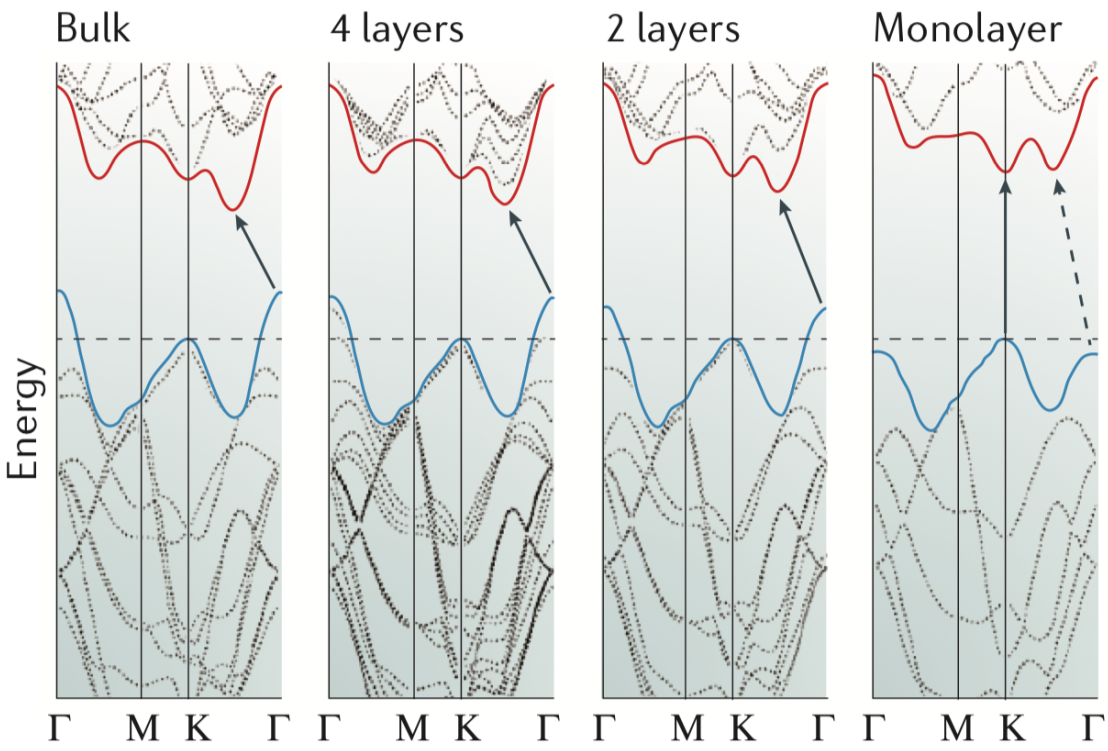

Figure 2.2: Band structures of MoS_2 calculated with DFT for Bulk, 4-layer, 2-layer, and monolayer samples. When the thickness is thinned down to monolayer, we can see that there is a transition from indirect to direct bandgap. Reproduced from [57].

to persist up to room temperature.

One of the more useful optical properties of these excitons are their optical selections rules. The excitons formed in the the K(K') valley couple to σ_+ (σ_-) circularly polarized light, which gives us an extremely easy way of generating carriers/excitons which are associated with only a single valley[93]. Many effects have been demonstrated that utilize this particular degree of freedom, such as the valley-hall effect[54] and controllable valley coherence[78]. There are also interesting effects that can be realized when coupling such materials to photonic structures, such as WS_2 monolayers coupled to silver nanowires, which couple the helicity of the emitted light to the direction of propagation along the nanowire[33].

These materials are also useful for nonlinear optics, as they possess high $\chi^{(2)}$

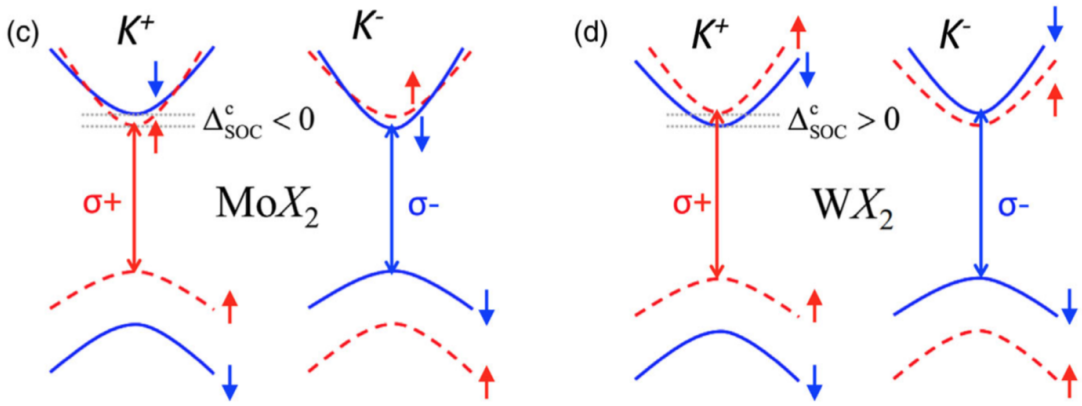

Figure 2.3: A schematic of the band structure near the K/K' prime points, showing the difference in the conduction band ordering between the $M0X_2$ materials, where the smallest gap is optically bright, and the WX_2 materials, where the smallest gap is optically dark. Reproduced from [79].

Table 1 | Electronic properties of 2D TMDs.

	MoS_2	$MoSe_2$	WS_2	WSe_2
Band masses (in m_0)[5]	~0.5	~0.6	~0.4	~0.4
Optical gap E_g (eV)	~2 (refs 7,8,22)	~1.7 (ref. 51)	~2.1 (ref. 25)	~1.75 (refs 23,24,26,45)
Exciton binding energy (eV)	~0.55 (ref. 20) or 0.9 (ref. 21) (Th.) ~0.2 or 0.4 (Exp.)[50]	~0.5 (Th.)[20] ~0.6 (Exp.)[49]	~0.5 (Th.)[20] ~0.4 (ref. 23) or 0.7 (ref. 25) (Exp.)	~0.45 (Th.)[20] ~0.4 (Exp.)[24]
Conduction band spin–orbit splitting (meV)[36]	~–3	~–20	~30	~35
Valence band spin–orbit splitting (meV)[5,36]	~150	~180	~430	~470

Th. and Exp. stand for theoretical predictions and experimental results, respectively. m_0 is the electron mass. The properties are for the lowest-energy conduction and valence bands.

Figure 2.4: A table detailing the electronic and excitonic properties of the four main group VI TMDCs. Reproduced from [56].

values[48]. Due to the crystal structure of the materials, the $\chi^{(2)}$ value is only non-vanishing for odd-numbers of layers, so SHG spectroscopy is sometimes used as a method for identifying layer thickness in few-layer samples. There have been several demonstrations of enhanced SHG from these materials coupled to photonic cavities and waveguides as well[14].

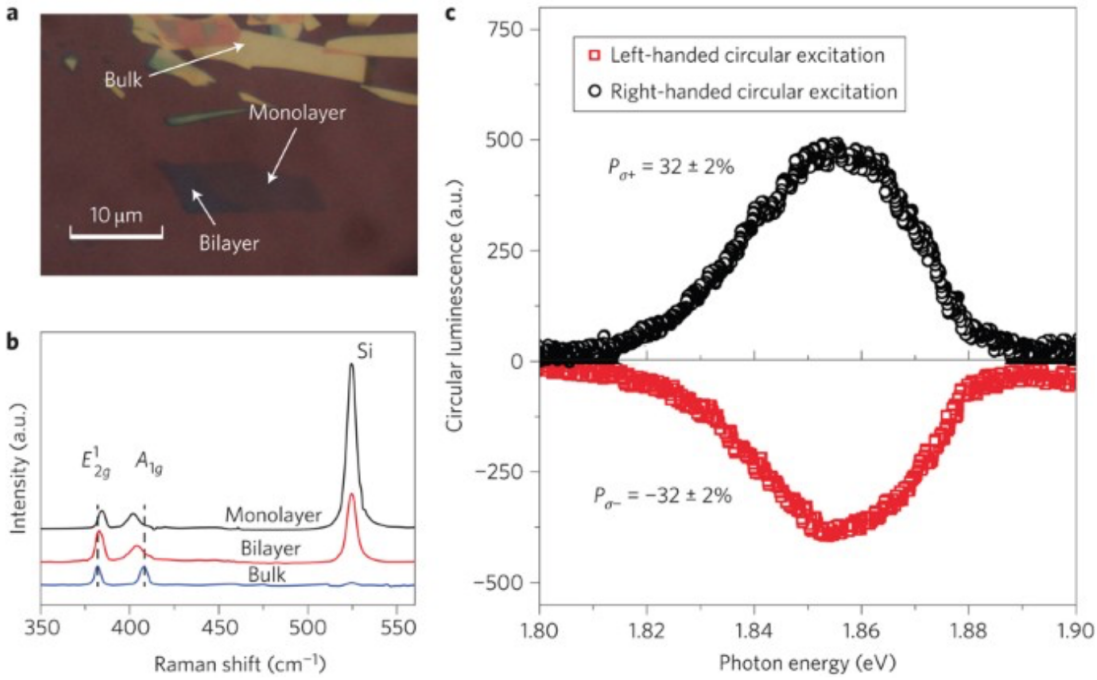

Figure 2.5: (a) An optical image of an exfoliated sample of monolayer MoS_2 (b) Raman spectra of the sample, showing the different modes for the three thicknesses (c) Polarization-resolved photoluminesence, showing that the circular polarization of the pump is partially preserved in the emission. Reproduced from [93].

2.2.3 Heterostructures

As noted above, one of the unique strengths of TMDCs and other 2D materials is their ability to be stacked in arbitrary configurations in order to create customized heterostructures. These can be designed to have a multitude of different electronic and optical properties.

The simplest form of heterostructure which is commonly used is hexagonal boron nitride (hBN) encapsulation, in which a monolayer or other heterostructure is surrounded above and below by at least one layer of hBN. This has been shown to dramatically reduce the linewidths of excitons, which is attributed to the hBN protecting the TMDC from substrate surface roughness, charge transfers, and local electric field fluctuations [11].

One of the more well-studied types of heterostructures involves combining two different group VI TMDCs, which allows for the creation of interlayer excitons. These excitons are long-lived due to their spatial separation, and have been predicted to show diverse phenomena such as topological[89] and moiré effects[90], like modified optical selection rules. They have also been used to demonstrate applications such as interlayer exciton lasers[64].

The moiré heterostructures feature several interesting physical features, such as registry-dependent optical selection rules (which can differ from the underlying monolayer optical selection rule)[90]. The moiré potentials in certain combinations of materials have been predicted to be particularly large, on the order of 100 meV, and have been predicted to be able to form arrays of emitters (similar to quantum-dot arrays) due to the confinement in the moiré potential.

2.2.4 Integration with Photonics

One of the strengths of these materials is their ability to be integrated with a diverse range of photonic devices. Since considerations such as lattice-matching are not relevant with these van der Waals materials[30], they can easily be exfoliated onto a wide array of photonic structures. One example of this is the integration of monolayers onto integrated photonic circuit elements, such as ring resonators[87]. Since the exfoliation process is very simple, and because the monolayer itself is thin enough that it doesn't have a huge effect on the fundamental underlying operation of the photonic device (e.g. the device still functions without the monolayer incorporated), the integrated photonics can be fabricated and its optical properties can be characterized prior to the monolayer transfer, and then the results before and after transfer can be compared. Other devices combining integrated optics with TMDCs have also been realized, such as tunable phase shifters[18].

Monolayer TMDCs have also been incorporated onto defect (L3) photonic crystal cavities made out of GaP in order to demonstrate lasing [91]. Again, similar to the integrated optical waveguides, the entire photonic structure can be fabricated and characterized prior to incorporating the monolayer. An important experimental feature which is evident in this paper is that the transfer process of the monolayer can significantly alter the quality of the device. Generally speaking, a drop in quality factor will result post-transfer. Depending on the system and transfer method, this could be due to many effects, such as excess residue or random fragments of transferred material, all of which will add disorder to the photonic environment. This drop was observed in both [91] and [87]. High quality factor devices which rely on having a periodic dielectric environment can be particularly effected by these spatial inhomogeneities. Integration has also been demonstrated in structures such as whispering gallery mode resonators[92], which also were used to demonstrate lasing.

These materials have also been integrated with a diverse range of photonic structures in order to achieve strong-coupling which we will discuss in the next chapter.

2.3 Group VII TMDCs

Group VII TMDCs have properties which are very different from group VI materials. The pair of materials ReS_2 and $ReSe_2$, which are both similar in terms of their optical properties, will be the group VII materials that we focus on and discuss here.

2.3.1 Overview

One of the major differences between the group VI and group VII materials is in their structural properties. Unlike the group VI materials' highly symmetric hexagonal lattice, the group VII materials have triclinic lattices. The greatly reduced symmetry results in a much more complicated band structure, and many of the

simple and useful properties of the group VI materials are absent.

There are similarities however, in that the group VII materials are still able to be mechanically exfoliated down to monolayer thicknesses, integrated onto a diverse range of photonic structures, and combined into heterostructures with other two-dimensional materials, including being combined with group VI materials.

2.3.2 Optical Properties

The optical properties of $ReS(e)_2$ are very different from the group VI materials. Due in part to the reduced crystal symmetry, there are two underlying excitons in these materials which are linearly polarized and nondegenerate[36]. There are two exciton peaks in the near-infrared, located between 1.55-1.6eV for ReS_2 and 1.36-1.4 eV for $ReSe_2$ [36]. The polarizations angles of the two excitons in each material are generally quite different, in bulk samples being almost orthogonal. For example, in [39] the angles between the two ReS_2 excitons is about 80°. An important feature is that the presence of linearly polarized excitons (although with different energies and with smaller difference in polarization angles) is maintained as the sample is exfoliated from bulk to few-layer and even monolayer thickness. This has been demonstrated in both $ReSe_2$[2] and ReS_2[39]. These unique optical properties have allowed for the exploration of a variety of phenomena, such as the selectively tunable optical stark effect [69]. Additional features include the clear presence of an excitonic Rydberg series, with multiple excited states (up to the fourth excited state in[39]) clearly visible.

An additional difference between the two groups of materials is the stacking-order dependence of SHG: while group VI materials tend to show a large SHG signal in odd-number layers, but not even number layers due to inversion symmetry, this trend is reversed in ReS_2, with only even-numbered layers showing an appreciable

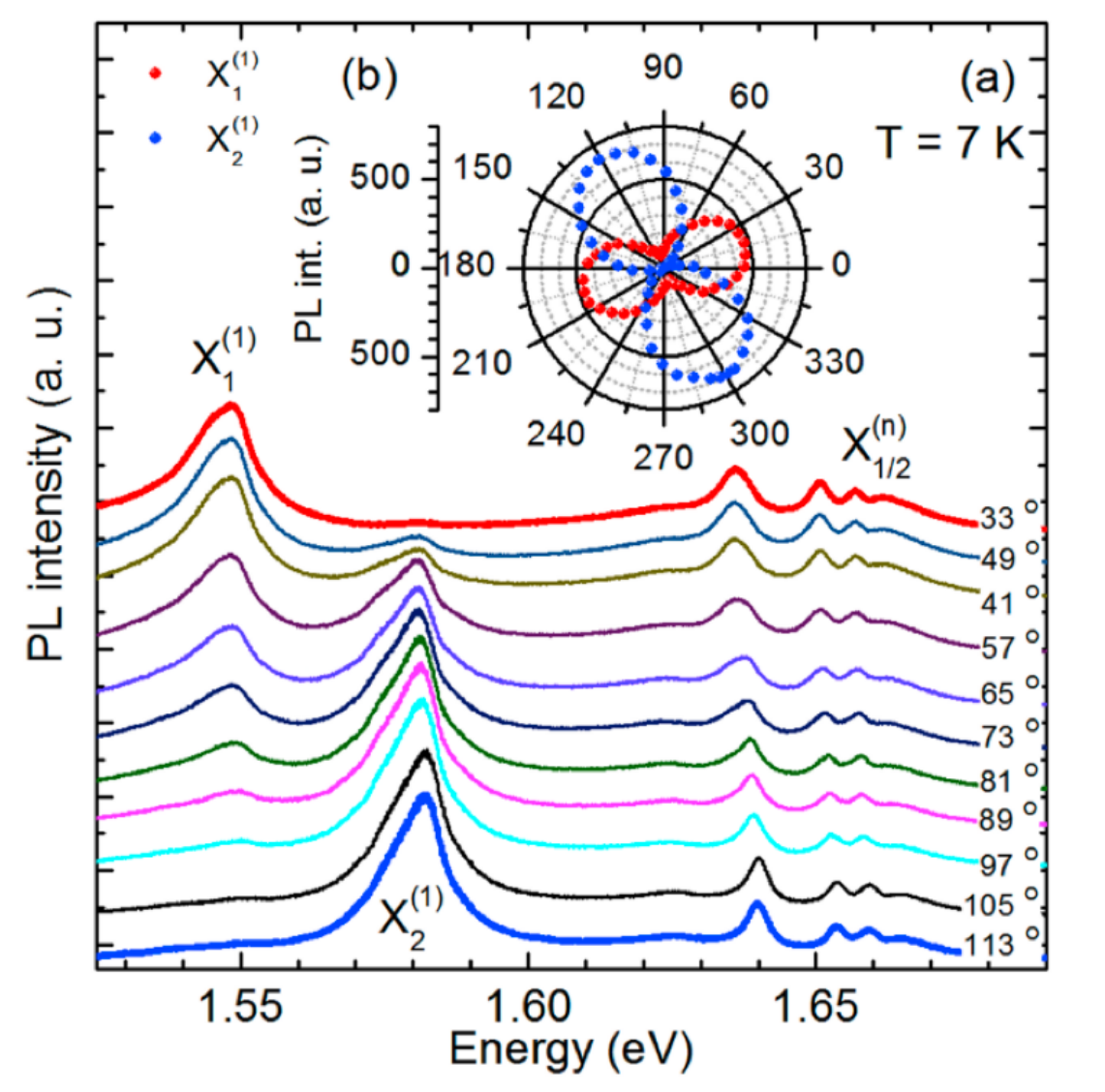

Figure 2.6: A polarization-resolved measurement of the photoluminesence from ReS_2, showing the two lowest-lying excitons which have polarizations that are oriented at roughly 80°, relative to each other. Also visible are the excitonic Rydberg series at higher energies. Reproduced from [39].

SHG generation[70].

Heterostructures have also been demonstrated between group VI and group VII materials, such as the demonstration of "twinned growth" between WS_2 and ReS_2, in which the two materials grown such that the crystals have complete overlap[97]. There has also been a demonstration of type-I and type-II band alignment het-

erostructures, composed of ReS_2/MoS_2[9] and ReS_2/WSe_2[75], respectively.

One interesting feature that had been observed in $ReSe_2$ is the presence of multiple closely-spaced exciton peaks (beyond the two expected ones)[2], whose energy changes based on sample thickness. These results show the clear presence of 4 non-degenerate exciton peaks in thick samples of $ReSe_2$, but in thinner samples the same clear, unambiguous identification of such peaks is not present. It has also been specifically noted in the literature[39] that measurements of thin ReS_2 samples do not show the same exciton splitting that was observed in thicker samples of $ReSe_2$. In this thesis, we will show that a very similar splitting of the peaks in these materials can arise due to intra-flake cavity effects rather than an inherent splitting of the excitons.

CHAPTER III

Light-Matter Coupling in Semiconductors

3.1 Semiconductor Excitons

The fundamental type of excitations in semiconductors that will be most interesting for the purposes of this dissertation is the exciton. Excitons are quasiparticles which are a bound state between an electron and hole, analogous to a solid-state hydrogen atom[60][61][62]. A common choice for excitonic materials are inorganic III-V semiconductors, such as GaAs. One of the important properties which governs the behavior and usability of a material is the exciton binding energy. In GaAs quantum wells, the binding energy is on the order of about 10 meV, which means that the excitons are not sustainable at room temperature due to the larger thermal energy at room temperature. There are materials that can operate at higher temperatures, such as GaN[15], ZnO[47], and organics[44], in order to overcome this deficiency, but can have additional drawbacks, such as large inhomogeneous broadening in these systems. As discussed in the previous section, one of the attractive qualities of TMDCs is the high binding energy of their excitons[56], which overcomes the limitations of materials like GaAs.

The properties of excitons can be tailored and engineered in many ways, including by coupling the material to an optical cavity. The modification of the excitons

properties depends sensitively on the design of the optical cavity. In this dissertation, we will primarily be concerned with the case where the coupling is strong enough that we enter the so-called strong coupling regime.

3.2 Microcavity Polaritons: The Strong Coupling Regime

3.2.1 Background

Systems	Atomic gases	Excitons	Polaritons
Effective mass m^*/m_e	10^3	10^{-1}	10^{-5}
Bohr radius a_B	10^{-1} Å	10^2 Å	10^2 Å
Particle spacing: $n^{-1/d}$	10^3 Å	10^2 Å	1 μm
Critical temperature T_c	1 nK–1 μK	1 mK–1 K	1–>300 K
Thermalization time/Lifetime	1 ms/1 s$\sim 10^{-3}$	10 ps/1 ns$\sim 10^{-2}$	(1–10 ps)/(1–10 ps)=0.1–10

Figure 3.1: A table detailing the different properties of Atomic gasses, Excitons, and Polaritons. Reproduced from [19].

The coupling of the excitons to the photons is characterized by the underlying decay rates of the exciton (γ_X) and cavity photon (γ_C) individually, and the characteristic coupling strength g_0 which depends on the properties of the material, exciton, and cavity. Generally speaking, the coupling will depend sensitively on the mode volume. In general, lower mode volumes (more tightly confined photons) will give rise to a stronger light-matter coupling.

The most common choice of optical cavity for polaritons is the Fabry-Pérot cavity. An example of this is shown in Fig. 3.2. The basic building blocks of these cavities are the Distributed Bragg Reflector (DBR), a stack of $\lambda/4$ layers with alternating high and low indices of refraction which forms a dielectric, high-reflectivity mirror. Generally speaking, a large index contrast is desirable in order to achieve the highest reflection. Other mirrors, such as metal mirrors, can be used, but typically are

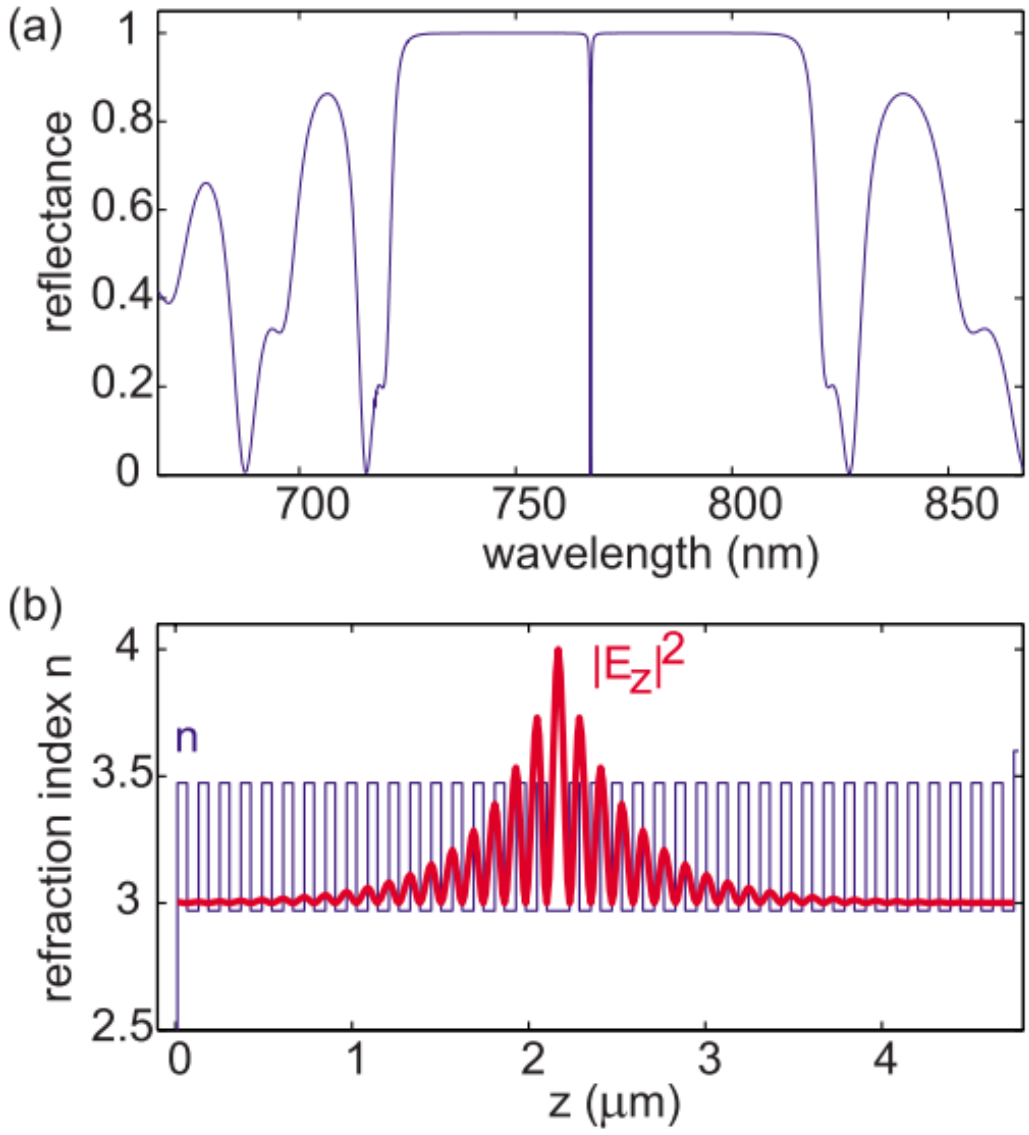

Figure 3.2: (a) The spectrum of a typical DBR/DBR Fabry-Pérot cavity, showing the high-Q resonance in the center of the stopband (b) The index and Electric field distribution correspond to the mode in (a), showing the high field intensity at the center of the cavity. Reproduced from [19].

avoided due to their intrinsically higher losses.

In order to form the cavity, two DBRs are sandwiched together, such that there is a $\lambda/2$ layer in the middle which forms the cavity. At the resonance wavelength λ, we will then get a resonant dip in the mirror reflectivity, as shown in the upper

panel of Fig. 3.2. The field distribution is plotted in the lower panel of Fig. 3.2, showing that we have a highly concentrated field in the $\lambda/2$ layer, which is where the exciton layer will be placed. When the coupling between the cavity and exciton is sufficiently strong, our exciton and photon modes will become hybridized states, the upper and lower polariton. The details of the effects of different DBR/DBR cavity designs on the performance of these cavities for strong coupling is discussed in [84].

Polaritons have many properties and applications which make them a popular subject of research. One of the most notable properties of polaritons is the fact that they are a hybridized state of an exciton and photon, and thus can inherit the useful properties of both underlying particles[19]. The nonlinearity of the polaritons is due to the excitonic component, and the very light effective mass (at certain momenta) is due to the photonic component. The light effective mass is particularly useful, since this gives the polaritons a very large thermal de Broglie wavelength, which drastically increases the temperature required for Bose-Einstein condensation. Unlike atomic BECs, which can require very low temperatures, some as low as a few hundred nK or less, these quasiparticles can condense at temperatures on the order of a few Kelvin, and in some systems, up to room temperature, as shown in Fig. 3.1. This means that standard laboratory helium cryogenics are sufficient to explore BEC physics, as opposed to the much more sophisticated cooling needed for atoms.

The BECs in polariton systems also have practical applications, such as using the coherent emission from the condensate state to effectively form a laser, which has been shown to have a lasing threshold which is lower than the threshold required for conventional lasing[42][20]. Polariton lasers have been demonstrated in electrically pumped devices which can operate at up to room temperature[10], two steps which are necessary for a practical light source.

Additional applications of polaritons include polariton logic gates[7], optically controllable quantum fluids[73], and polariton lattices capable of supporting topological states[45].

3.2.2 Properties of Polaritons

Here we will review some of the theoretical foundations of polaritons from[19]. The Hamiltonian for a system of excitons coupled to confined photons can be written as

$$H_{pol} = H_X + H_C + H_I = \sum E_C(k)\hat{a}_k^\dagger \hat{a}_k + \sum E_X(k)\hat{b}_k^\dagger \hat{b}_k + \sum g_0(\hat{a}_k^\dagger \hat{b}_k + \hat{a}_k \hat{b}_k^\dagger)$$

Where $\hat{a}$ and $\hat{b}$ are the annihilation operators for the cavity photon and exciton,

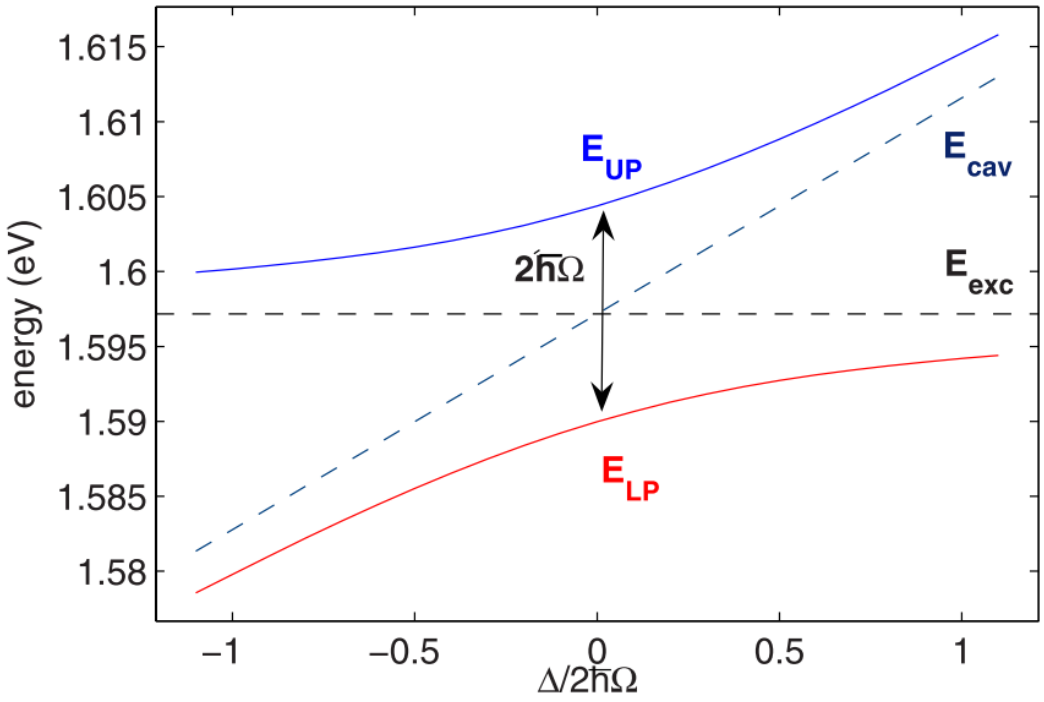

Figure 3.3: A typical anti-crossing in a polariton system, showing the Rabi splitting $2\hbar\Omega$ at the zero-detuning point, where the upper and lower polariton are closest. Reproduced from [19].

respectively. This Hamiltonian can then be diagonalized by defining the following

new operators $\hat{P}_k$ and $\hat{Q}_k$:

$$\hat{P}_k = X_k \hat{b}_k + C_k \hat{a}_k$$

$$\hat{Q}_k = -C_k \hat{b}_k + X_k \hat{a}_k$$

which transforms the Hamiltonian into

$$H_{pol} = \sum E_{LP}(k) \hat{P}_k^\dagger \hat{P}_k + \sum E_{UP}(k) \hat{Q}_k^\dagger \hat{Q}_k$$

with

$$E_{UP,LP}(k) = \frac{1}{2}\left[E_X + E_C + i(\gamma_X + \gamma_C) \pm \sqrt{4g_0^2 + [E_X - E_C + i(\gamma_C - \gamma_X)]^2}\right]$$

where $\hat{P}_k$ and $\hat{Q}_k$ are the annihilation operators of the new, coupled quasiparticles of the system, the upper and lower polaritons. The coefficients we defined are called Hopfield coefficients, which satisfy:

$$|X_k|^2 = \frac{1}{2}\left[1 + \frac{\Delta E(k)}{\sqrt{\Delta E(k)^2 + 4g_0^2}}\right]$$

$$|C_k|^2 = \frac{1}{2}\left[1 - \frac{\Delta E(k)}{\sqrt{\Delta E(k)^2 + 4g_0^2}}\right]$$

where we define the detuning as

$$\Delta E(k) = E_X(k) - E_C(k).$$

These Hopfield coefficients essentially dictate how exciton-like or photon-like the state is. They satisfy

$$|X_k|^2 + |C_k|^2 = 1$$

and each of the quantities $|X_k|^2$ and $|C_k|^2$ essentially correspond to how exciton-like or photon-like the state is. Thus, when one of these two approaches unity, it means the system at that k is very similar to the uncoupled exciton or photon, and when both are close to 1/2 this means the system is half-excitonic and half-photonic.

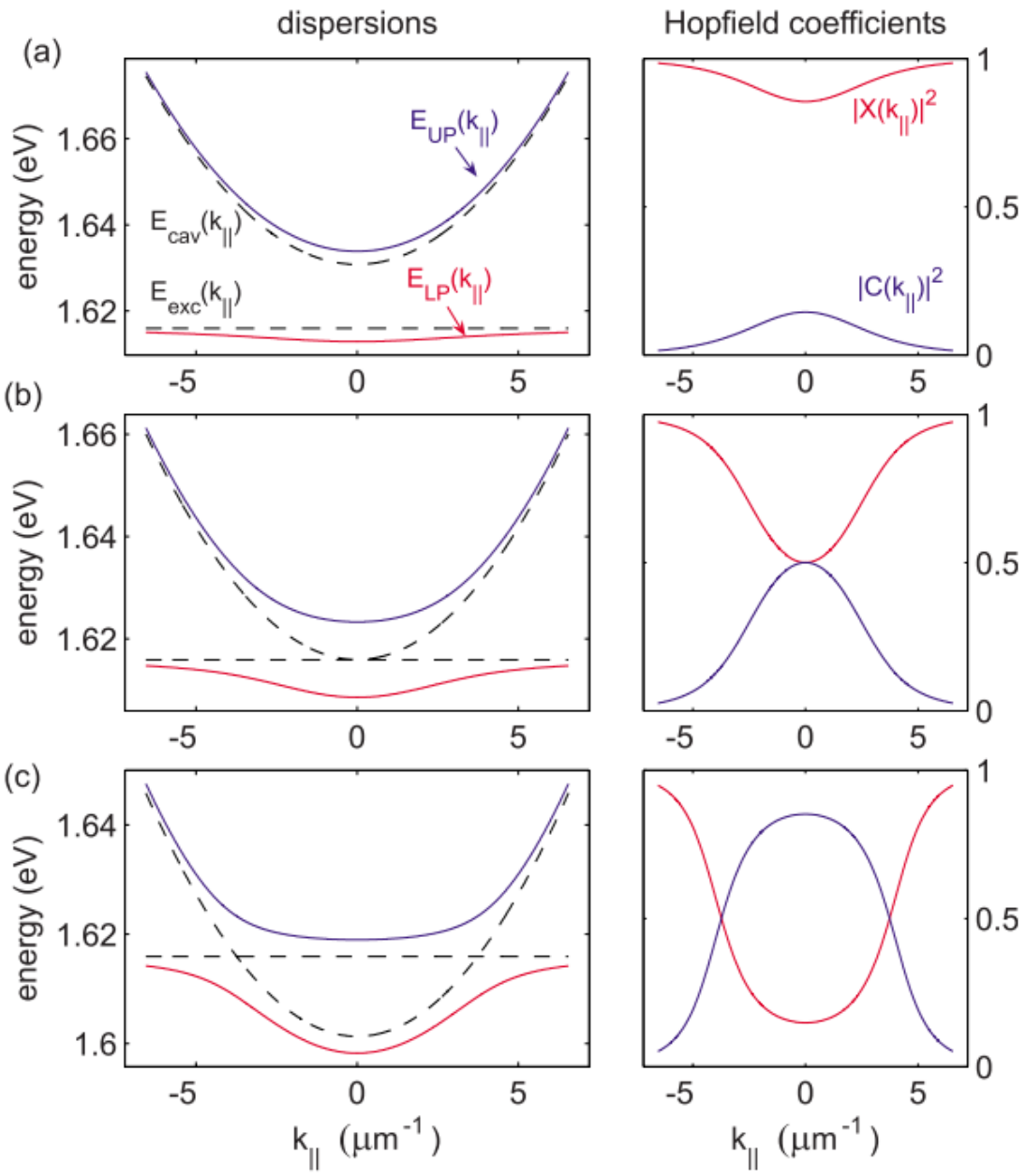

Figure 3.4: Plots of the coupled and uncoupled dispersions and associated Hopfield coefficients for polariton dispersions for (a) Blue detuning, (b) zero detuning, and (c) red detuning of the photon mode at $k = 0$. Reproduced from [19].

A non-vanishing splitting $2\hbar\Omega$ requires that

$$2g_0 > |\gamma_X - \gamma_C|$$

at zero detuning. This condition is insufficient for strong coupling, however. Instead

we require more stringent condition that

$$2\hbar\Omega > \gamma_X + \gamma_C$$

in order for the system to be in the strong coupling regime.

3.3 Polaritons in Two-Dimensional Materials

Since the discovery of two-dimensional semiconducting TMDCs, there has been a tremendous interest in exploring the possibility of strong coupling with these materials. Because the excitons have such large binding energies and are therefore stable at room temperature, this brings the exciting possibility that many of the phenomena in conventional polariton systems may now be accessible without the need for cryogenic cooling, which would make them much more practical.

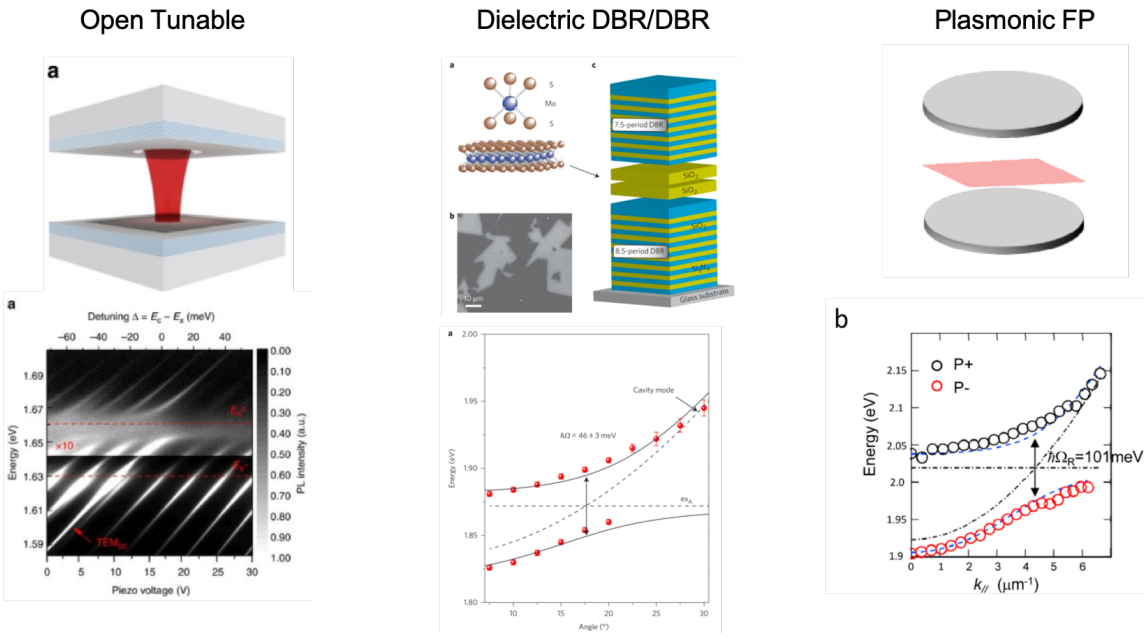

Figure 3.5: Three typical cavity structures used for strong coupling in TMDCs. (left) An open tunable cavity from [21] (middle) A closed all-dielectric DBR/DBR cavity from [50] (right) a closed metallic Fabry-Perot cavity from [83].

The unique structural properties of TMDCs present both challenges and benefits in terms of how easy they are to integrate with optical cavities. Many initial attempts

to create polaritons in these materials used Fabry-Pérot type cavities, in one of two configurations. The first involved closed cavities, akin to the type used in III-V materials. These have been demonstrated with both all-dielectric mirrors[50] as well as with metallic mirrors[83]. These have better performance, but the growth processes runs the risk of damaging the material after transfer. The second type are open cavities, in which the monolayer is exfoliated or grown onto the surface of one mirror, and a second mirror is suspended with a piezo-controller above the first mirror, with an airgap separating the top mirror from the flake[21]. These cavities have larger-than-ideal mode volumes, and are impractical for on-chip integration. Additionally, there are other types of systems which can support strong coupling in TMDCs, which utilize optical modes that can have very different properties from Fabry-Perot cavities. One example of this is using plasmonic nanoantennas[72], which confine the electric field to a very small region.

Another type of polariton which is relevant to this dissertation is the self-hybridized polariton. In these systems, the optical cavity is formed by the material itself, without the need for a complete external cavity constructed around the exciton layer, as shown in 3.6. In other words, the material acts as both the exciton layer and the cavity. This has been demonstrated in group VI materials using thick flakes of TMDC[63].

Recently, condensation of polaritons in a WS_2 monolayer has been demonstrated at room temperature[98]. This demonstrates a very important advance in the state of 2D-material polaritons, as the demonstration of condensation is a prerequisite to exploring most of the interesting physics that is associated with polaritons.

Two of the main results of this thesis are the demonstration of self-hybridized polaritons in group VII materials, as well as theoretical and experimental results

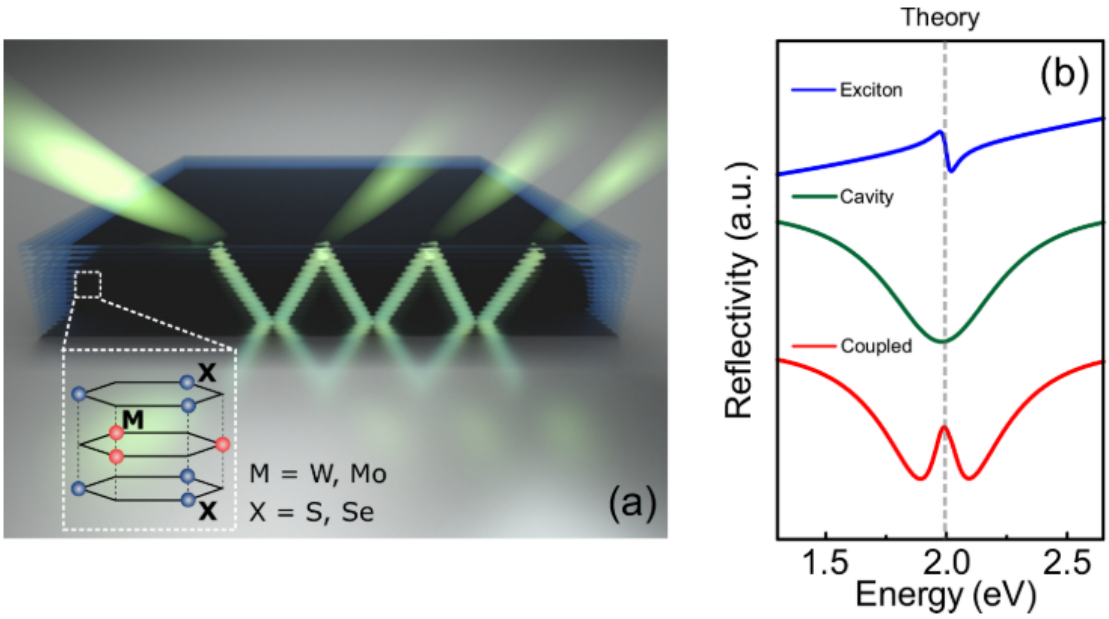

Figure 3.6: (a) A schematic showing the principle of self-hybridization in group VI TMDCs (b) Calculations of uncoupled and coupled modes of the self-hybridized system. Reproduced from [63].

presenting a new method of creating polaritons with group VI TMDCs by utilizing photonic crystals instead of Fabry-Pérot type cavities.

CHAPTER IV

Designing Photonic Crystals for Strong Coupling in TMDC Monolayers

4.1 Introduction

In this section, we will demonstrate strong coupling in photonic crystals coupled to TMDCs. Much of this work has been published in Optics Express [32] and is reproduced here.

There have been many previous examples of polaritons in two-dimensional materials systems, most frequently utilizing Fabry-Pérot type optical cavities. One of the biggest advantages of TMDC monolayers is their versatility of integration, since they can be exfoliated onto a wide variety of optical structures. Many of the Fabry-Pérot structures are either open-cavity structures, which have a larger-than-ideal mode volume and are impractical for integration into practical on-chip devices, or closed cavities, which are more complicated to fabricate (involving more steps) and risk damaging the monolayer via stresses and strain induced during the fabrication process.

Here we demonstrate dielectric slab photonic crystals as a flexible and compact platform for polaritons, where excitons are strongly coupled to photons confined in the leaky modes of the slab. We show that our structure is well-suited for van der Waals materials, features unusual adjustable dispersions, and allows for multi-

wavelength operation on a single chip. The TMDC monolayers are directly exfoliated onto photonic crystals, which is particularly simple from the standpoint of integration and we are able to sustain strong-coupling at temperatures up to room temperature. We will review some background on photonic crystals, the design procedure for these devices, and example calculations of photonic crystals integrated with WS_2 monolayers. Additionally, we will briefly review an alternative photonic optimization method. Finally, we will present experimental results which demonstrate excellent agreement between the theoretical predictions and fabricated devices, demonstrating the viability of this method as a room temperature polariton platform.

4.2 Photonic Crystals for Controlling Strong Coupling in van der Waals materials

When excitons in semiconductors are strongly coupled to photons, new quasi-particles called exciton-polaritons are formed[37, 88]. In vertical Fabry-Pérot (FP) microcavities, polaritons have a meta-stable ground state at the zero in-plane wavenumber with a very light effective mass and robust coherence. Such microcavity polaritons allow room-temperature Bose-Einstein condensation and other many-body phenomena at high temperatures, potentially enabling polaritronic devices such as low threshold lasers and ultrafast optical switches[19, 13, 26]. However, high quality vertical FP cavities are made of distributed Bragg reflectors, which require a large numbers of wavelength-scale epitaxial-layers that are closely lattice-matched to the quantum wells containing the excitonic medium. Consequently, such polariton cavities are difficult to make and are limited to a handful of material choices. High quality polariton cavities have been made with GaAs and CdTe systems, but they require low temperature operation. In high temperature materials, polaritons have been realized with GaN[15], ZnO[47], and organics[44], although typically with

relative low cavity quality and large inhomogeneous broadening of excitons, which makes it challenging to observe many-body coherent phenomena. Furthermore, the multi-layer construction of FP-cavities makes them bulky and inflexible, and it is difficult to integrate multiple components on a single chip.

Recently, monolayer transition metal dichalcogenides crystals (TMDCs) have emerged as a promising candidate for both high-temperature polariton physics and increased flexibility in device integration. They are direct-bandgap semiconductors[71, 55] with exceptionally large exciton binding energies and oscillator strengths[56], therefore supporting excitons and polaritons at room temperature [50, 95, 49, 21, 83, 8].

Uniquely, these 2D crystals and heterostructures can be placed on substrates without requiring lattice-matching and are robust against surface effects of the substrate [91]. These properties suggest new possibilities to control matter-light interactions in these materials with diverse photonic structures. It has been demonstrated that photonic crystal defect cavities coupled to 2D materials can be used to enhance both absorption[29] and emission[28], as well as second harmonic generation[27, 23]. Recently TMDC-polaritons have been created in slab photonic crystals (PhCs) [95]. In this chapter, we provide the design principles of such PhC-polariton systems and show that they enable dispersion engineering, and multi-color integration on a single chip, therefore providing a flexible and compact platform for 2D material polaritons.

4.2.1 Guided mode resonances

We will restrict the discussion to the simplest example of one-dimensional (1D) periodic PhCs, so as to clarify the basic properties and design principles of the slab-PhC polariton system. Extension to more complicated 1D patterns and 2D PhCs is straightforward conceptually as well as fabrication-wise, but opens up a wide design space for mode-engineering. For the 1D PhC, we will consider a semi-infinite

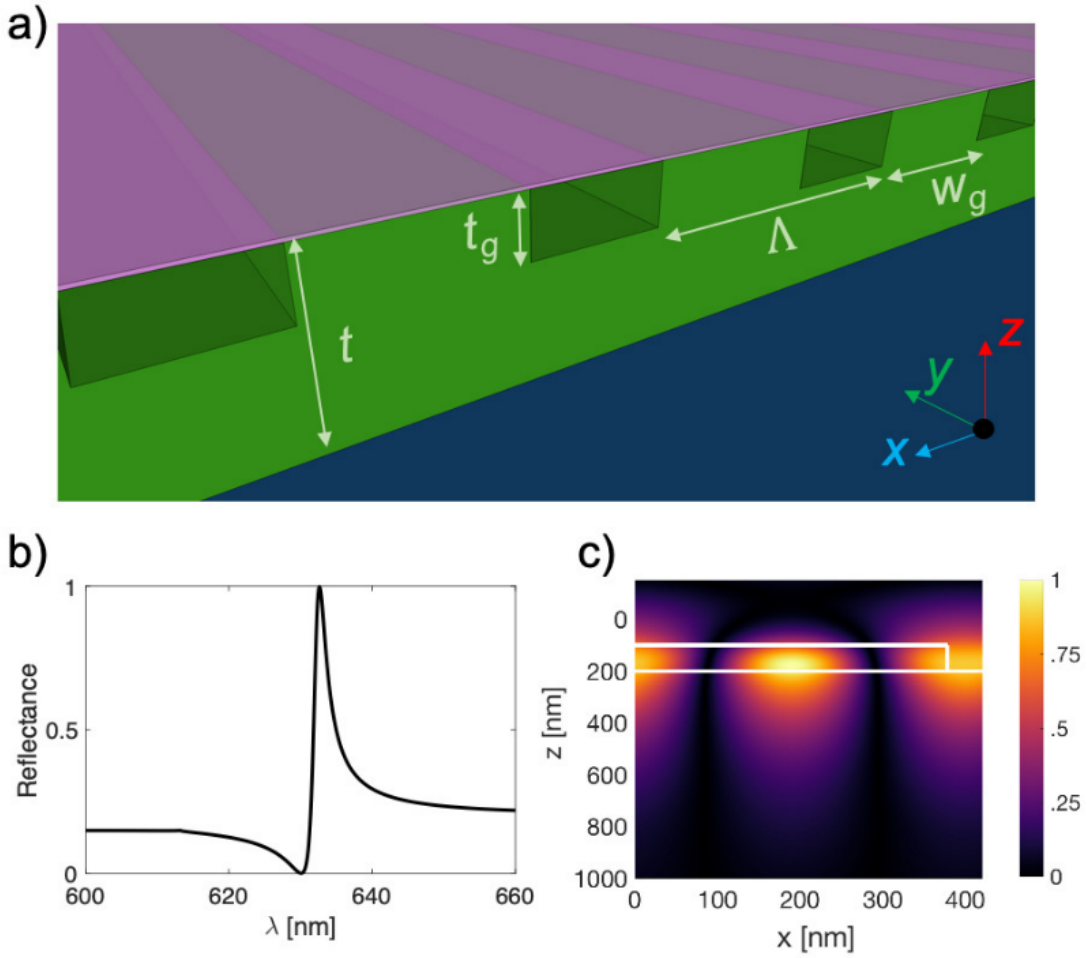

Figure 4.1: (a) A schematic of the proposed PhC structure. (b) A reflectance spectrum of the guided mode resonance showing the characteristic asymmetric Fano lineshape ($\Lambda = 420$ nm, $t = 100$ nm, $\mathcal{F}_\Lambda = .9$, $\mathcal{F}_t = 0$) (c) The distribution of the amplitude of the electric field for the guided mode resonance in (b).

SiO_2 substrate ($n = 1.46$) with a Si_3N_4 (n=2.02) PhC grown on top. As shown in Fig. 4.1(a), the PhC is characterized by a period Λ, thickness t, modulation fill factor $\mathcal{F}_\Lambda = w_g/\Lambda$, and thickness fill factor $\mathcal{F}_t = (1 - t_g/t)$. All calculations are done using the RCWA method.

We utilize guided mode resonances in the PhC, which occur when light is incident on a weakly modulated PhC that essentially acts as a periodic waveguide [16]. The incident light can be coupled into the waveguide mode and propagates along while

energy is coupled out of the waveguide due to the periodic modulation [66], resulting in the formation of sharp, polarization-dependent resonances. Assuming the index modulation can be treated as a weak perturbation, these resonances are formed when the external radiation and the waveguide mode satisfy the following phase matching condition [67]:

$$|\mathbf{k}_{\parallel}(\omega)| = \left| \left(k_x(\omega) \pm m\frac{2\pi}{\Lambda} \right) \hat{\mathbf{x}} + k_y(\omega)\hat{\mathbf{y}} \right| = |\boldsymbol{\beta}_j(\omega)| \tag{4.1}$$

where ω is the angular frequency, $\mathbf{k}_{\parallel}$ is the in-plane wavevector, $k_{x,y}$ are the wavenumbers of the external radiation in the $\hat{\mathbf{x}}/\hat{\mathbf{y}}$ directions, m is an integer, and $\boldsymbol{\beta}_j$ is the effective propagation constant of the j^{th} slab waveguide mode. The resonance wavelength can be adjusted by modifying Λ, which changes the frequency that satisfies Eqn. 4.1, or by adjusting the grating parameters such as t, $\mathcal{F}_\Lambda$, or $\mathcal{F}_t$, which alters the waveguide dispersion $\boldsymbol{\beta}(\omega)$.

This type of mode is qualitatively quite different from the more popular photonic crystal defect mode, such as the one used in [91], where the photonic crystal is constructed such that it has a photonic bandgap in-plane, and a defect is introduced which pulls a localized state into the bandgap. This type of defect cavity is particularly popular in nanophotonics, and can be integrated with monolayers in much the same way as the guided-mode resonance photonic crystals. One important difference is that the defect modes do not possess an easily accessible method of detuning the photon mode, so mapping out an anti-crossing of the two modes can be difficult. In contrast, our modes have a dispersion which can easily be measured via k-space resolved spectroscopy.

The mechanism behind the operation of the guided-mode resonance is clearly illustrated in 4.2. Consider a slab of dielectric material, which supports a guided mode with a dispersion, as plotted. Since this is a true bound mode, the dispersion

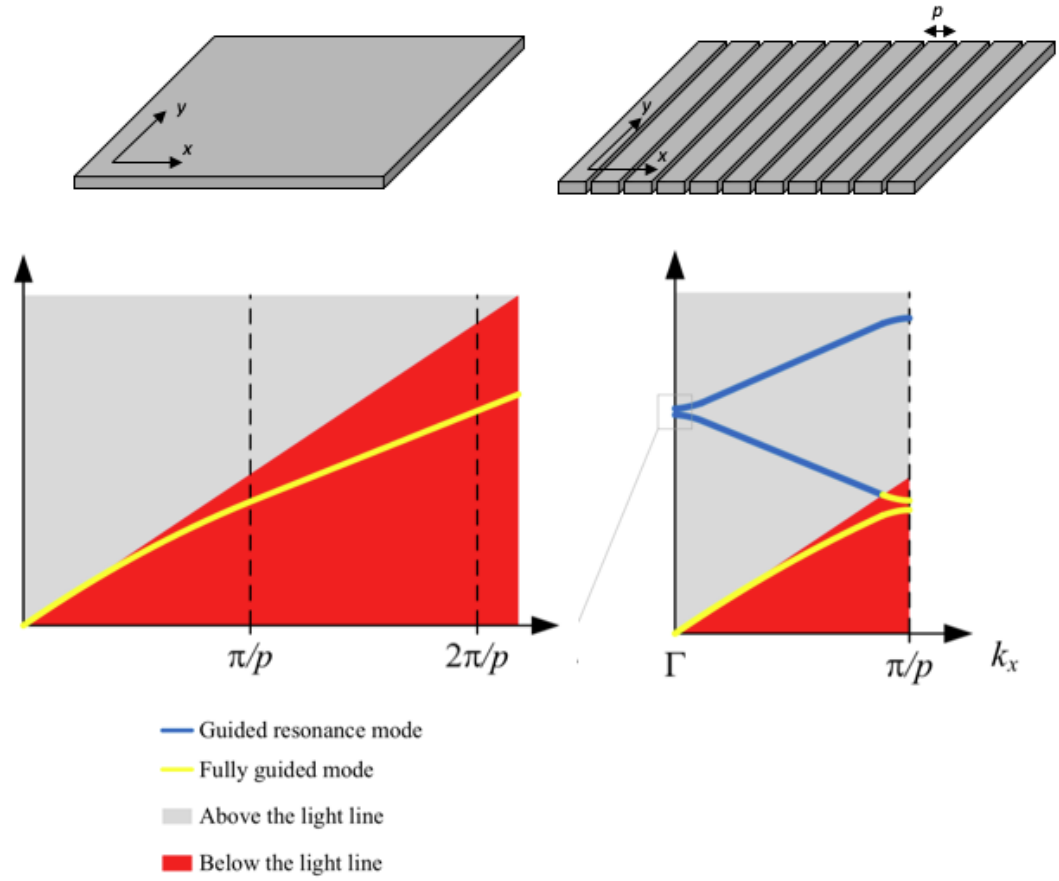

Figure 4.2: A schematic showing the operation of a guided-mode resonance in a photonic crystal. (left) The dispersion of an unpatterned dielectric slab, showing modes that exist soley below the light-line (right) The dispersion of the slab after patterning, showing the formation of a Brillouin zone, the opening of band-gaps, and the folding of modes inside the light line. Adapted from [34].

is entirely below the light line and thus is not accessible from vertically incident light. If we pattern this slab, we will form a Brillouin zone and fold the bands into the irreducible Brillouin zone. Several important modifications result from this: first, a bandgap will open up at the edges of the Brillouin zones. Second, there are folded bands which now exist inside the light cone, which now do couple to externally incident light. As a result of this, the nature of the mode is strongly modified; rather than being a true guided (bound) state, it is now a leaky resonance with a finite lifetime. It is clear what the dispersion looks like along the k_x direction in Fig. 4.2,

and an example of the full 2D dispersion surface near one of these resonance is shown in 4.3.

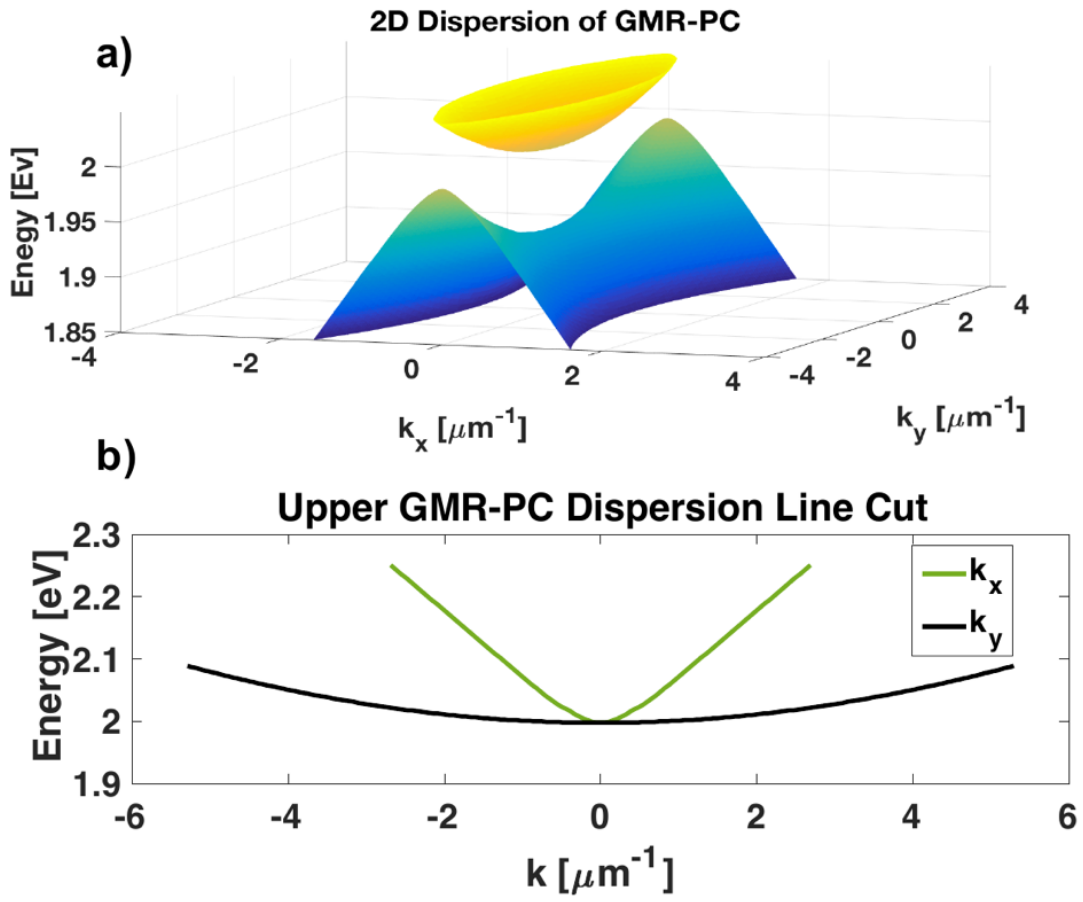

Figure 4.3: (a)The two-dimensional dispersion surface of a typical guided-mode resonance, showing both the folded-waveguide k_x dispersion and the upwards-facing k_y dispersion (b) Line cuts of (a) which show the difference between the the two momentum directions.

The fundamental mode manifests as a narrow-band peak in the reflectance spectrum, with the peak reflectance approaching unity, as shown in Fig. 4.1(b). This is due to destructive interference of the transmitted light [66, 53]. The resonance features a characteristic Fano lineshape due to interference between energy reflected through two distinct pathways: energy is reflected directly from the slab as well as indirectly reflected after coupling to the guided resonances of the slab [22, 52].

The linewidth of the resonances can become very narrow, in particular when the magnitude of the index modulation (controlled here by $\mathcal{F}_\Lambda$ and $\mathcal{F}_t$) is very small[82].

This type of PhC structure has been used in a variety of applications, such as general-purpose narrow-band optical filters [53], biosensors [68], and distributed feedback lasers [43]. In this letter, we focus on using the fundamental TE_0 mode for strong-coupling.

4.2.2 Photonic design for strong coupling

In order to gain some intuition about the design of these photonic crystals, it is instructive to consider the behavior of a simple un-patterned slab waveguide. The primary consideration which will need to be kept in mind is the electric field distribution, as this is the property of the cavity which will directly modify the exciton-photon coupling energy. Although the field distributions are not exactly the same as those of the photonic crystal, the behavior is close enough to provide qualitative guidance on what we should expect. In Fig. 4.4 we show the fields calculated for three different waveguide thicknesses. In order to maximize the light-matter coupling, we want to simultaneously keep the mode volume small, while maximizing the field overlap with the monolayer.

We can see that for thin waveguides, the optical mode is close to the cutoff (e.g. the slab is barely thick enough to support a mode), and although the field amplitude outside the slab is a high fraction of the maximum field, the mode volume is huge (which, as we will see later, means the normalized field is small). As we make the waveguide thicker, we can see that the mode is much more localized in the slab, which drastically lowers the mode volume, and the field at the monolayer is still an appreciable fraction of the maximum field value. Finally, for a thick waveguide, the mode volume again increases, and the field at the monolayer is a small fraction of

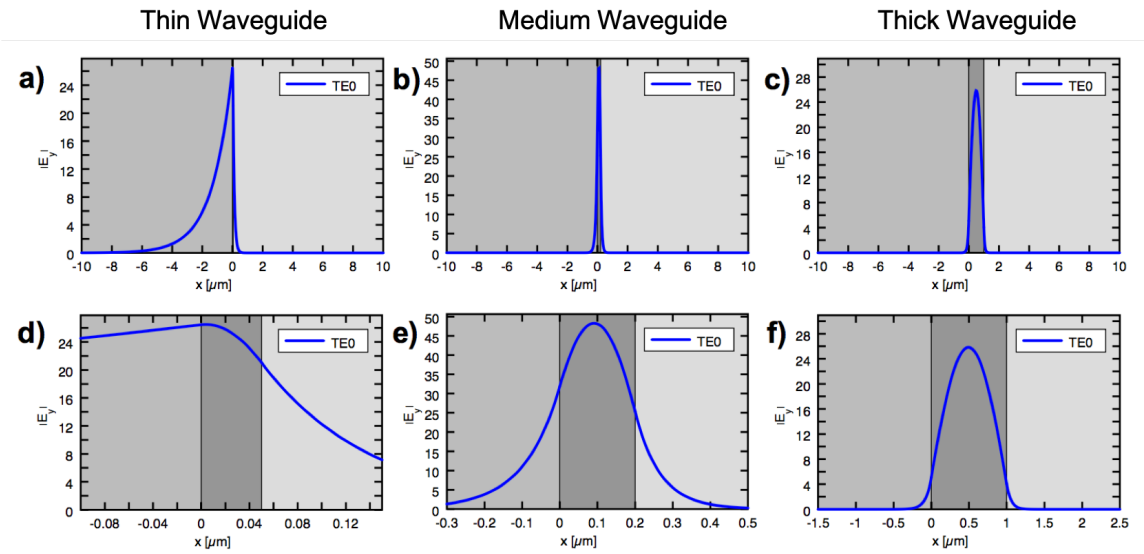

Figure 4.4: Plots showing the calculated electric field distributions of thin (left), medium (middle), and thick (right) slab waveguides comprised of SiO_2 (medium colored), Si_3N_4 (dark colored), and air (light colored). The top row is zoomed out versions of the bottom row.

the maximum field. Thus, we can conclude that very thin and very thick waveguides are both detrimental to the light-matter coupling strength, and thus we can expect there to be a middle value which balances these considerations and yields the optimal coupling strength.

Now, we consider the full photonic crystal. The thin slab results in strong vertical confinement of the waveguide mode and large electric field enhancement (Fig. 4.1(c)), which makes the 1D PhC a good platform for polaritons. The electric field of the resonant mode is confined to the high-index slab and decays exponentially into the surrounding regions. The 2D materials can be incorporated simply by exfoliation onto the top of the PhC, as shown in Fig. 4.1(a). Note that propagating waveguide-polaritons can also be formed in unmodulated waveguides[77], which do not have a meta-stable ground state and do not couple out of the system except at the ends of the waveguide. Here we focus on polaritons with a meta-stable ground state within

the light cone, by using PhCs.

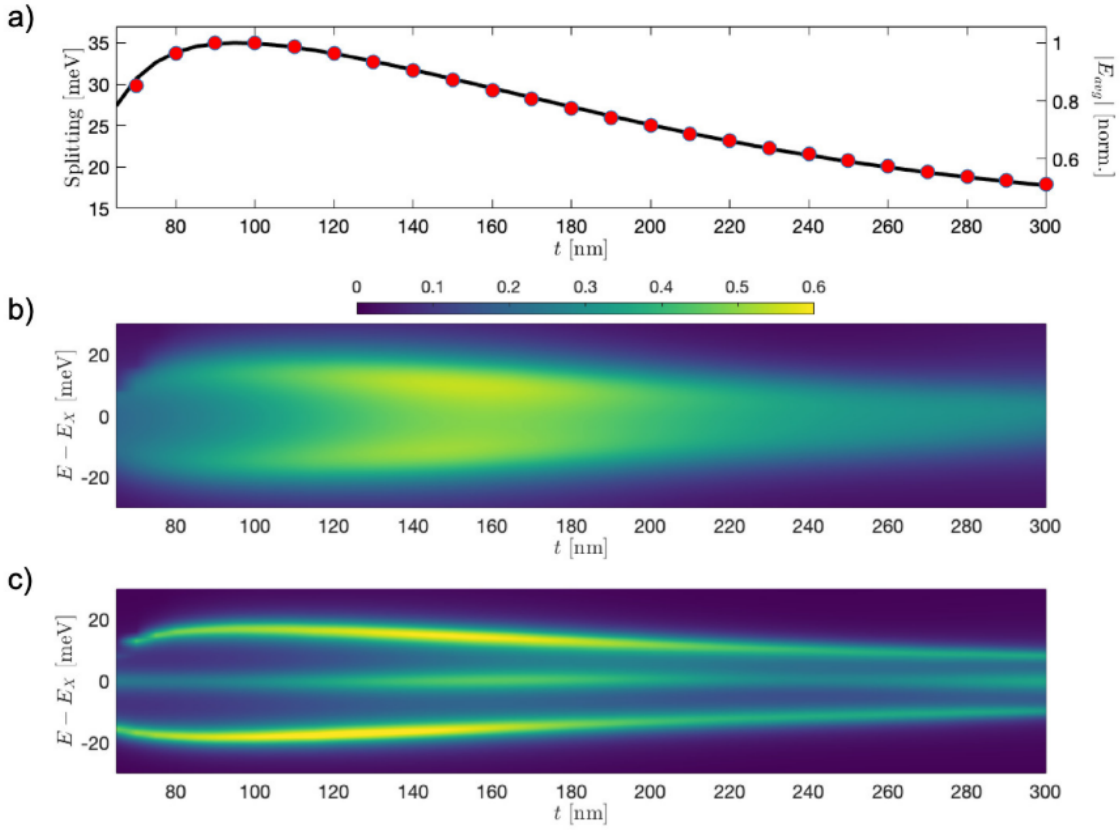

Figure 4.5: (a) Variation of the average normalized field amplitude at the monolayer (black) with t_g, compared with the polariton splitting vs. t_g obtained from (c) (red dots); (b-c) The absorption spectrum versus the PhC thickness at high (b) and low (c) temperatures. The period is tuned to maintain zero-detuning with the exciton. All calculations are at normal incidence.

The evanescent coupling between the PhC mode and the 2D material excitons can be tuned by adjusting the thickness of the slab. This can be understood as being analogous to the evanescent field overlap in the asymmetric slab waveguide. When the PhC layer is much thicker than the operating wavelength, the field is mostly confined within the PhC with low evanescent leakage as well as low normalized peak amplitude. Reducing the thickness, the evanescent leakage increases while the normalized peak amplitude also increases due to tighter confinement, leading to higher field amplitude at the surface of the photonic crystal. This can be quantified

by appropriately normalizing the electric fields according to [84]

$$\int |\mathbf{E}(\mathbf{r})|^2 \epsilon(\mathbf{r})\, dV = \frac{1}{2}\hbar\omega. \tag{4.2}$$

The electric field is confined in the vertical direction and unbound in the in-plane directions, and the integral is evaluated over a finite volume. As the photonic crystal thickness is decreased to much smaller than the wavelength, there will be a high amount of field leakage, and the peak amplitude of the field will decrease as well since the confinement is no longer sufficient to localize the field. Thus, it follows there is an optimal thickness for the field-amplitude enhancement. This is seen in Fig. 4.5(a), where we plot the E field, normalized according to Eqn. 4.2 and averaged in the plane of the monolayer.

With a large field enhancement and the large oscillator strength of TMDCs, strong coupling is readily achieved once we incorporate TMDCs on the PhC. We consider the example of a monolayer WS_2, coupled to a PhC with $\mathcal{F}_t = 0$ and $\mathcal{F}_\Lambda = .9$, with the period Λ adjusted such that we obtain a guided mode resonance at zero in-plane wave-number that matches the exciton resonance. We model the exciton resonance of a single .8 nm thick monolayer of WS_2 as a Lorentz oscillator:

$$\varepsilon(E) = \epsilon_B + \frac{f}{E_X^2 - E^2 - i\Gamma E} \tag{4.3}$$

with background static permittivity $\varepsilon_B = 20$, exciton resonance E_X, oscillator strength f=1.59 eV^2, and linewidth Γ=30 meV, consistent with experimentally measured results[83]. The resonances of this WS_2-PhC coupled system are shown in Fig. 4.5(b). Normal mode splitting is evident. The splitting varies with the thickness of the grating, proportional to the field strength enhancement, as shown in Fig. 4.5(a). A maximum splitting of about 30 meV is obtained at maximum field enhancement, comparable to monolithic DBR structures near room temperature[49], and 13 meV

smaller than the splitting in Bloch-Surface Wave structures[8], as expected by the improved field confinement in the latter[5]. The corresponding optimal thickness is at $t = 100$ nm, in agreement with Eqn. 4.2. Although we are primarily interested in room temperature polaritons in this letter, for comparison we show the same plot at low temperatures in Fig. 4.5(c) by reducing Γ to 5 meV, which shows a similar result with a slightly higher splitting of about 35 meV. The coupling can be increased by moving the TMDCs to the interior of the PhC, where the field amplitude is higher, and by using more than one monolayer. By embedding three WS_2 monolayers in the center of the Si_3N_4 layer of the PhC, each separated by 2 nm sheets of hBN, the polariton mode splitting is increased to over 70 meV. While we have used Si_3N_4 here due to its prevalence as a common optical material, higher index materials can also be used to increase the coupling[5].

Due to the coexistence of the direct and indirect transmission/reflection pathways discussed above, the structure exhibits both weak coupling of excitons to the free-space continuum of optical modes, clearly visible in Fig. 4.5(b), and the split upper and lower polaritons modes formed due to strong coupling between the exciton and the confined resonant mode.

4.2.3 Alternative Methods for Optimization

In this chapter, we have looked at designing these photonic crystals based on the physical principles of the device. There are, however, alternative ways of approaching device design. One way would be to brute force the problem by fixing the general architecture of the device, and then simulating all possible values of the different parameters. This is computationally expensive for most simulations, and generally isn't feasible except for particularly simple problems. As an alternative method of optimizing our devices, we can instead use automated algorithmic methods which

intelligently search through the simulation space and attempt to minimize some defined loss function in order to arrive at a design which fulfills our requirements. We'll briefly review one such method here, the so-called particle-swarm optimization. Although we did not end up using this for any of our final designs, it is a popular method which is useful for many types of problems where physical intuition is more difficult to come by.

The general flow of this type of optimization involves initializing a "swarm" of "agents", each of which is defined by a coordinate in the defined parameter space. The simulation is run for the parameters associated with each agent, and the results of the simulation are converted into a defined loss-function which determines the "fitness" of each agent. At each round, the agents keep track of their personal best value, and the global best value amongst the entire swarm, and at each round the position of each agent is updated following a kinematic formula with new velocities based on their old velocity, the distance of each agent from their personal best, and the distance from the global best. The weighting between these can be modified as a hyperparameter of the optimization process, or can be dynamically changed during the optimization, e.g. in order to favor "local" exploration early on and "global" consensus at later points in the optimization.

Example results are shown in Fig. 4.6, where we are optimizing a photonic crystal to act as a broadband mirror (simply as a test problem, unrelated to the goal of strong coupling in TMDCs). We compare the results to a value in the literature from [58], and see that our algorithm is able to converge on a solution which is very comparable.

Although this methodology is very useful for some problems, for the problems we are interested in this chapter, we will not need to resort to heuristic algorithms in order to complete our designs.

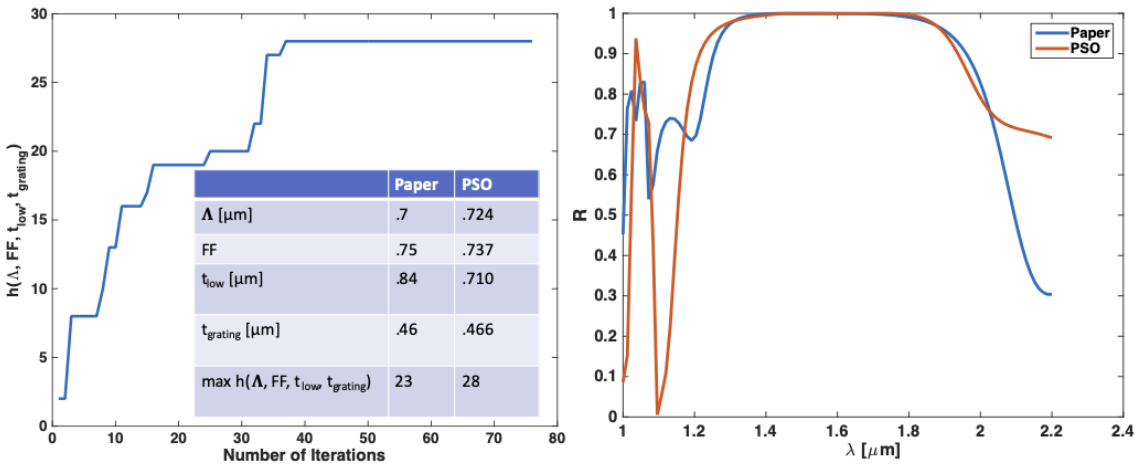

Figure 4.6: (left) A plot of the convergence of a PSO optimization algorithm solving for a high-reflectance mirror (inset) A table of the final parameters, compared to the results from [58] (right) A plot comparing the solution from [58] and the solution found using PSO.

4.2.4 Dispersion properties

Unlike a DBR cavity, which has a fixed isotropic dispersion, a PhC allows for more complex dispersions [85]. As shown in Fig. 4.7, the dispersion of the polariton modes consists of highly anisotropic bands. Along one direction it is very steep, and along the other it is shallow. The anisotropy of the bands can be understood from the phase matching condition in Eqn. 4.1. For dispersions along just the $\hat{\mathbf{x}}$ and $\hat{\mathbf{y}}$ directions, we have the following expressions:

$$|\mathbf{k}_{\parallel}(\omega)| = \left| k_x(\omega) \pm m\frac{2\pi}{\Lambda} \right| = |\boldsymbol{\beta}(\omega)|, \tag{4.4}$$

$$|\mathbf{k}_{\parallel}(\omega)| = \sqrt{\left(m\frac{2\pi}{\Lambda}\right)^2 + k_y^2(\omega)} = |\boldsymbol{\beta}(\omega)|. \tag{4.5}$$

The first equation simply results in a folded waveguide dispersion, and the second results in an approximately parabolic dispersion with a much lower group velocity. The dispersion anisotropy means that depending on the plane in k-space being considered, the polaritons have drastically different group velocities.

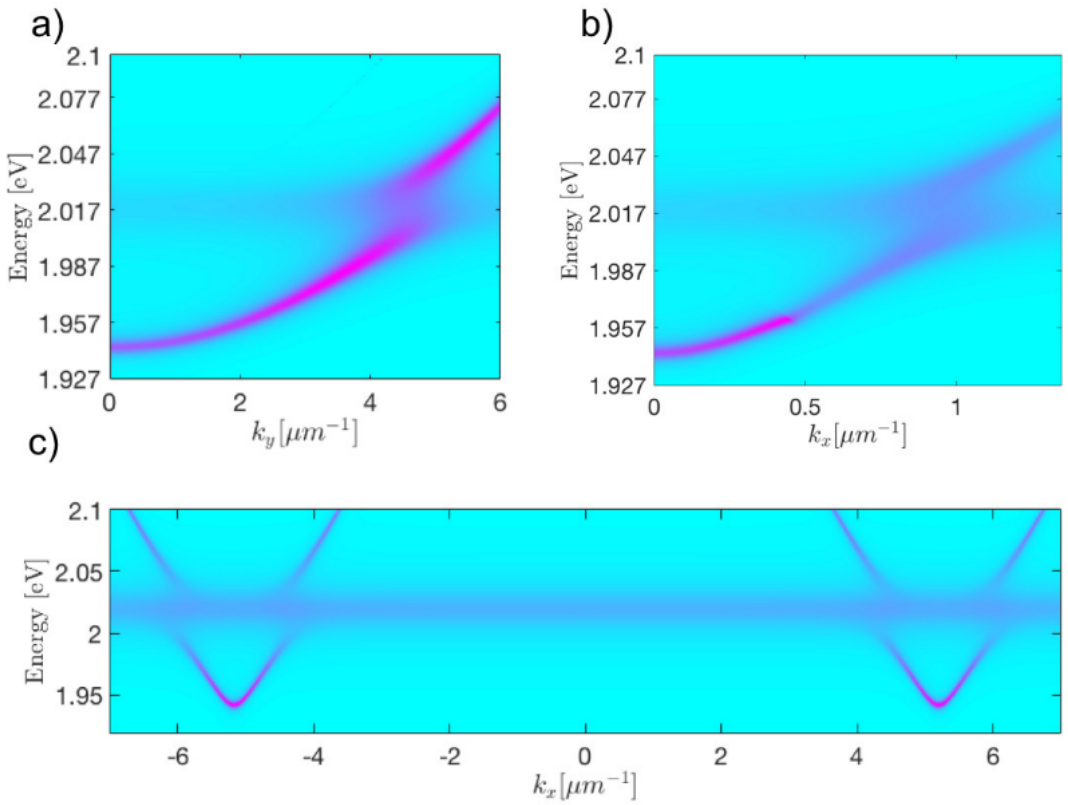

Figure 4.7: (a-b) Polariton dispersions along the two principle k directions; note the different scales on the k-axis. (c) A double-well dispersion, showing two separate local minima located at the first Brillouin zone edges $k_{min} = \pm\pi/\Lambda$, well away from $k = 0$.

The device may also be designed to have unusual dispersions. For example, the polariton ground state can be shifted to $k \neq 0$. As shown in the example in Fig. 4.7(c), the ground states are located at the edge of the PhC Brillouin zone at $k_x = \pi/\Lambda$. For this structure, we use a center-coupled grating with $\Lambda = 606$ nm, $t = 100$ nm, $\mathcal{F}_t$=0, and $\mathcal{F}_\Lambda$=.96. By choosing Λ appropriately, the edge of the Brillouin zone can be tuned to a desired k_x.

The 1D PhC can be generalized to two dimensions. The dispersion may be further tuned by breaking the symmetry in the $\hat{\mathbf{y}}$ direction to create a 2D PhC, or by introducing variations within a single period [51] to allow additional degrees of freedom in designing the dispersion relation for the system, such as massless Dirac

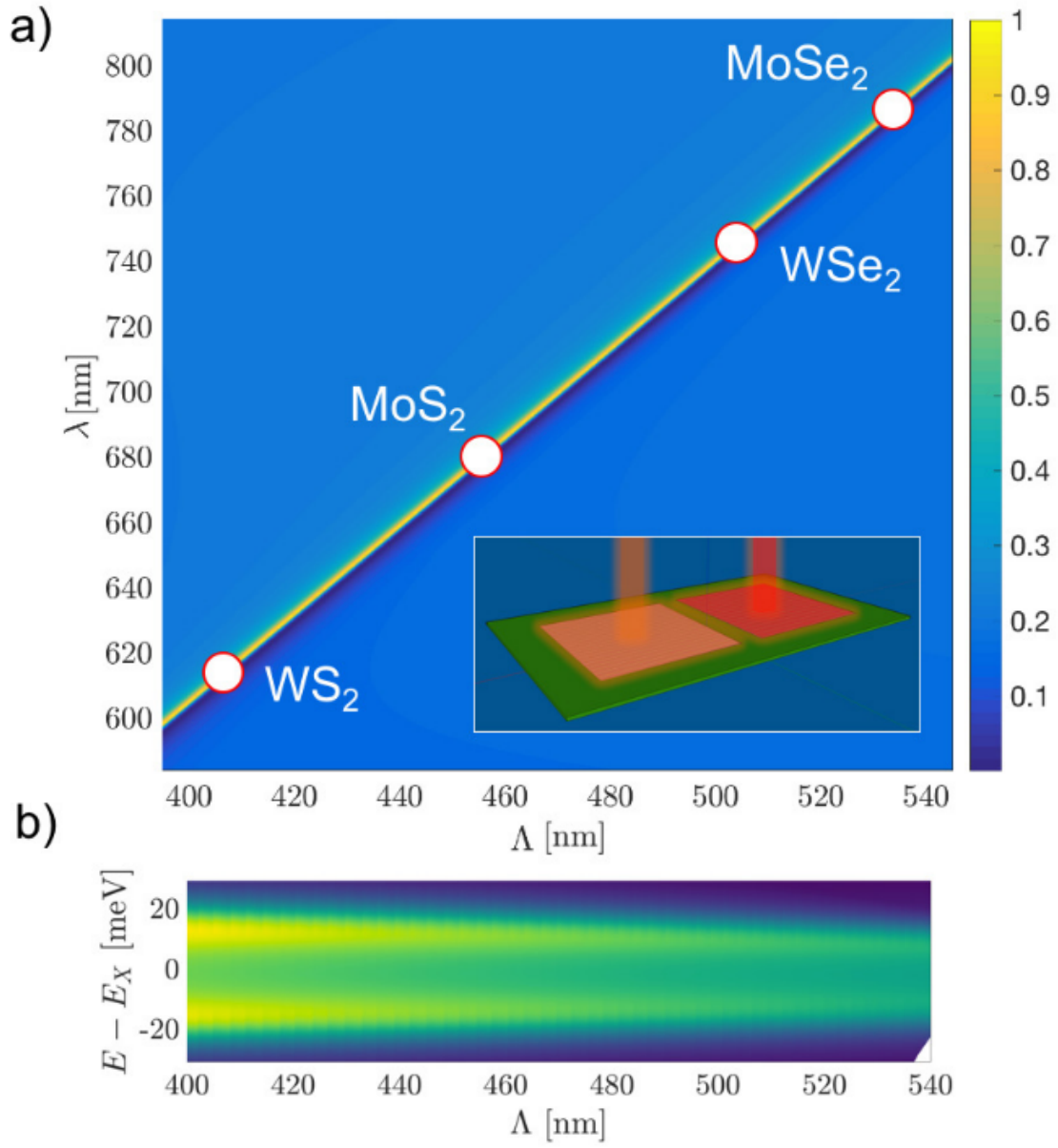

Figure 4.8: a) Tuning of a PhC resonance with the period Λ while all other grating parameters are fixed. The circles mark the resonance wavelength of the exciton resonances of the four commonly used monolayer TMDCs. Inset: A schematic showing the proposed multi-wavelength chip with multiple TMDC heterostructures emitting at different wavelengths. b) The corresponding absorption spectrum of the TMDC-PhC system as Λ is tuned. Normal mode splitting is evident and maintained throughout the tuning range.

disperions[99].

4.2.5 Multi-color, hybrid polariton systems on a single chip

Another unique benefit of the PhC platform is that different PhC cavities can be created side-by-side on the same slab of a uniform total thickness t, which allows for simple fabrication of multiple devices operating at different wavelengths on the same chip[41]. With 2D materials, the different PhC cavities can also couple to different materials. As an example, in Fig. 4.8 we tune the PhC resonance in the strong-coupling regime over 200 nm by varying only the period. The PhC has a fixed $t = 100$ nm, $\mathcal{F}_\Lambda = .9$, and $\mathcal{F}_t = 0$. For a period of $\Lambda = 420$ nm, this structure is equivalent to the structure in Sec. 4 for strong coupling with monolayer WS_2. As we vary Λ from 400 nm to 540 nm, the resonance shifts from 600 nm to 800 nm, covering the exciton resonances of four common monolayer TMDCs. At the same time, a high finesse is maintained. Adjusting the exciton resonance to track the PhC resonance and assuming the same oscillator strength and linewidth of WS_2, we compute the coupled modes in this structure. As shown in Fig. 4.8(b), normal mode splitting is maintained throughout the tuning range of over 200 nm. This shows that one can straightforwardly integrate photonic and polaritronic devices of WS_2, WSe_2, MoS_2, $MoSe_2$ and their heterostructures at various temperatures, simply by choosing an appropriate Λ at various locations on a single chip.

4.3 Experimental Demonstration

Using the previous sections as a guide, several photonic crystals with integrated monolayers were fabricated by our group, with results presented in [95] (the fabrication and characterization done by Long, the first author of this paper). The photonic crystals were designed for two TMDCs, WS_2 and WSe_2. Since WS_2 has a higher oscillator strength, it is expected to have a higher Rabi splitting and thus was the

choice for demonstrating room-temperature strong coupling. The results are shown in Fig. 4.10. WSe_2 has a smaller oscillator strength, and results are only presented at cryogenic temperatures, as shown in Fig. 4.9.

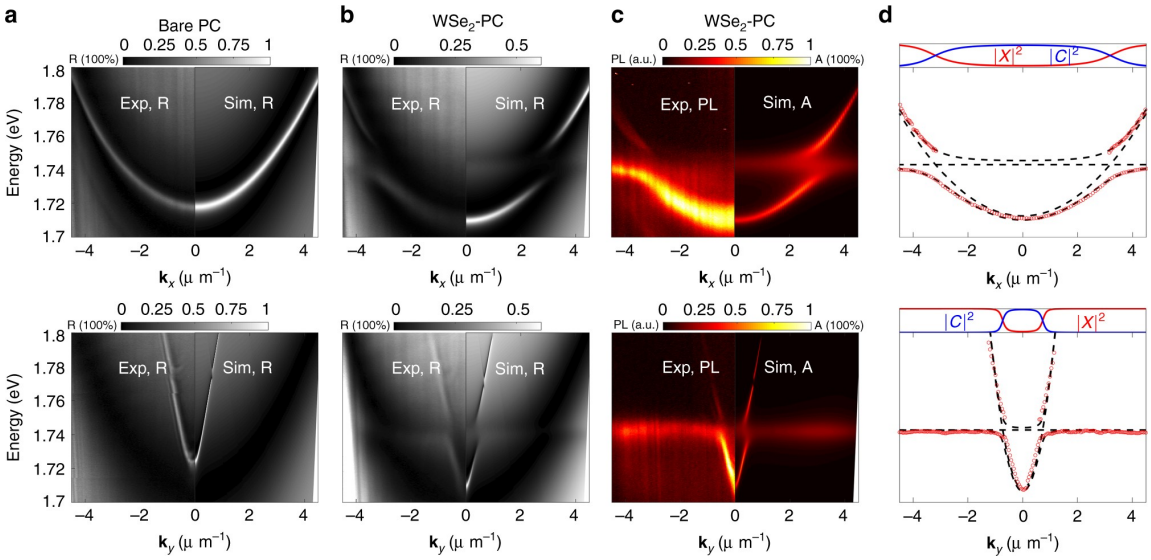

Figure 4.9: (a-c) Plots showing comparisons of the calculated and experimentally measured dispersions of a WSe_2 polariton device at 10K (d) Fitting and extracted Hopfield coefficients of the measured spectra. Reproduced from [95].

In both cases, we have excellent agreement between the experimental results and the theoretical predictions. These results unambiguously demonstrate that the guided-mode resonances in appropriately designed photonic crystals are a viable platform for polariton physics in TMDC monolayers.

4.4 Conclusions

In conclusion, we have demonstrated slab PhCs as a simple and flexible structure for creating polaritons with monolayer TMDCs. The PhC resonators allow comparable exciton-photon coupling as in DBR cavities, while allowing on-chip integration, compact design, and a much greater degree of flexibility in engineering the properties of the polaritons, including generating complex dispersions and wavelength tuning.

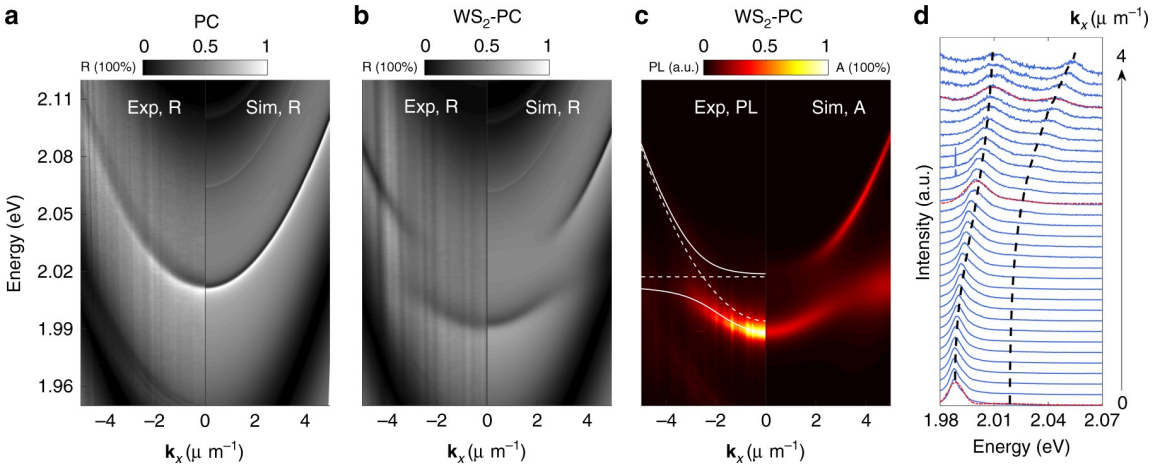

Figure 4.10: (a-c) Plots showing comparisons of the calculated and experimentally measured dispersions of a WS_2 polariton device at room temperature (d) A waterfall plot of the measured photoluminesence. Reproduced from [95].

These features will facilitate the realization of novel phenomena and development of practical photonic devices with 2D material polaritons.

CHAPTER V

Dual-Band Cavities for Strong Coupling

5.1 Introduction

When designing photonic cavities for integration with excitonic materials, we typically only consider the coupling of a single optical mode to a single excitonic state. Due to the ubiquitous presence of multiple excitonic states in TMDCs, it is worth considering the design of cavities designed to coupled to multiple resonances simultaneously. Here we present results of a cavity which had two modes, a guided-mode resonance and Fabry-Pérot mode, which both have a tightly confined field near the same location and are independently tunable over a broad range, and may facilitate coupling to a diverse range of excitonic modes in 2D materials and other systems.

5.2 Design of Dual-Band Photonic Cavities for Coupling to TMDCs

Optical cavities play a critical role in the engineering of light-matter interactions. The most common system consists of a single emitter coupled to a cavity with a single optical mode. This arrangement allows for the exploration of a wide variety of physical phenomena, such as Purcell enhancement[28] and polaritons[19, 37, 88], and many more. Although the most common situation is to consider is a single emitter and a single optical mode, in practice most material systems which are explored often

have many different resonances, which can be separated by a wide range of different energy gaps. The popular transition-metal dichalcogenides (TMDCs) provide an example of a system with a particularly rich landscape of resonances which can be coupled to an optical cavity. For example, in the semiconducting group VI TMDCs (MoS_2, $MoSe_2$, WSe_2, and WS_2), even a single monolayer has a rich excitonic landscape, with several neutral excitonic resonances corresponding to different interband transitions, which are separated by 100s of meV (corresponding to the large valence band splitting). Additionally, there are prominent peaks corresponding to charged trions, which are typically separated by 10s of meV from their corresponding neutral excitons.

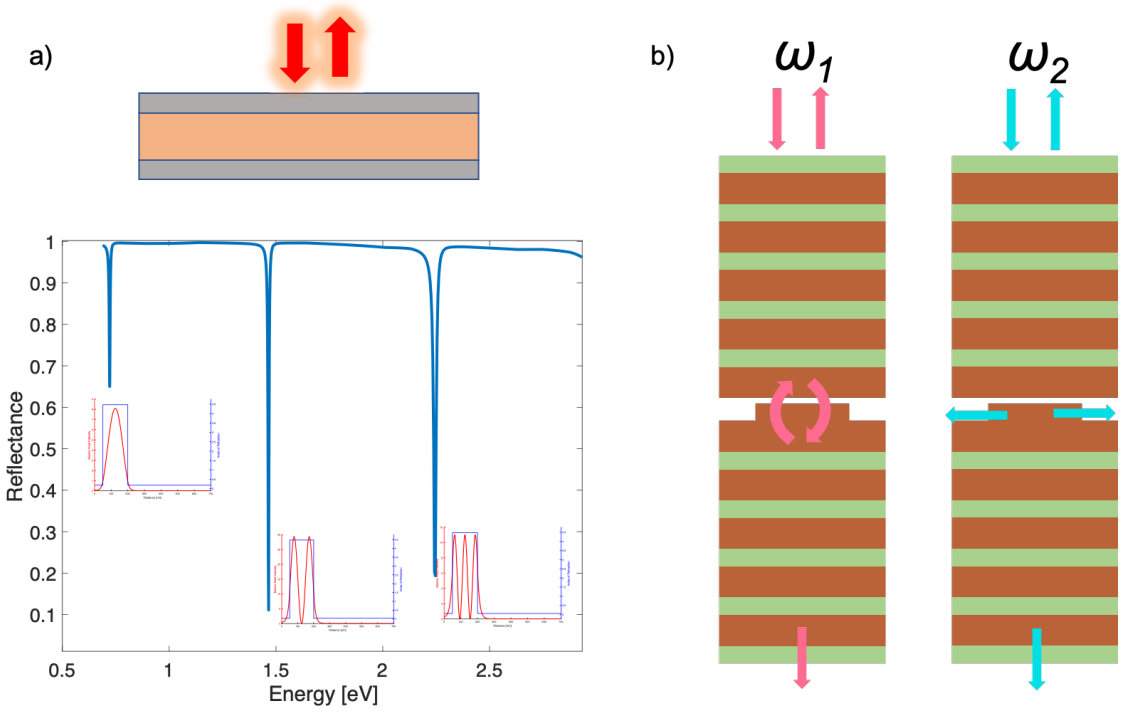

Figure 5.1: (a) Spectrum of a typical Fabry-Perot cavity, showing multiple modes and their associated field intensity distributions (b) A schematic of the proposed dual-band cavity, which is designed such that it supports both guided-mode resonances and Fabry-Perot modes with electric field distributions which both overlap with the same material layer, and can be tuned independently of each other.

The excitonic landscape can be further tailored by combining multiple materials.

Moving beyond a single monolayer, one can produce a large variety of composite heterostructures by stacking multiple TMDCs, leading to a wider array of interesting excitonic features. For example, both intralayer and interlayer excitons can be redistributed across a set of moiré peaks due to the moiré potential formed by a heterobilayer, and the separation between these peaks is highly tunable by adjusting the angle between the two layers[90][89]. Additionally, a bilayer of two different group VI materials will naturally have two intralayer excitons which are separated by 100s of meV.

There a wide variety of cavities which are commonly used for light-matter coupling: Fabry-Pérot cavities[50], guided-mode resonances[95] and defect modes[91] in photonic crystals are all common choices. These cavities are generally designed such that a single optical mode is coupled to the material. One example of a situation where two optical modes are desirable is in the case of doubly-resonant second harmonic generation, where an optical mode is resonant at both ω and 2ω[74, 80]. Whereas the design of a single-mode cavity is relatively straightforward, the design of this double-mode cavity is more involved and naturally presents challenges.

In this chapter, we demonstrate the design of hybrid cavities which form resonances by two completely distinct photonic processes: a Fabry-Pérot type mode and a guided-mode resonance formed by propagating states inside the DBR cavity. The spectral properties of the modes as well as their electric field distributions are independently tunable, allowing for a high level of control in engineering the light-matter interactions of systems with many excitonic resonances.

5.2.1 Results and Discussion

As an illustrative example of a typical optical cavity, consider the structure shown in Fig. 5.1a, a Fabry-Pérot cavity formed by two silver mirrors. This structure sup-

ports a spectrum of modes, which are formed when the round-trip phase ϕ is equal to a multiple of 2π. Each mode order also has an associated electric field distribution, with the m^{th} mode having m electric-field anti-nodes. These modes are not independently tunable: once we have fixed a desired m^{th} order mode at a frequency ω_m, the rest of the modes $\omega_{k\neq m}$ and their associated electric field distributions are fixed, and cannot be tuned to an arbitrary frequency.

In order to overcome the design limitations of conventional cavities, we propose a cavity which supports modes that originate from two entirely separate physical mechanisms, which would in principle allow the modes to be tuned separately from each other. The design of our proposed structure is shown in Fig. 5.1b. It consists of a DBR/DBR type Fabry-Pérot cavity, where the cavity region in the center is etched with a weak periodic modulation. For this design, we use two materials, a high index material with $n_h = 2.55$, corresponding to TiO_2, and a low index material with $n_l = 1.46$, corresponding to SiO_2. The structure is on an SiO_2 substrate, with seven DBR pairs of thicknesses $(t_h,t_l) = (126,205)$nm, arranged so the top layer is a low index layer. The particular thicknesses we use here don't exactly correspond to exactly the same value $\lambda/4n$ for both materials, but nevertheless these parameters result in a high-reflectivity dielectric mirror. Then, we have 75nm of SiO_2, a 70nm thick SiO_2 grating layer with a fill-factor of 50% and adjustable period Λ, 10nm of air (which can be replaced by another material), and finally another 7 DBR layers (with the layer closest to the etched portion being a low-index layer). Designing the cavity in this manner allows for two distinct mechanisms to simultaneously be supported: the completely out-of-plane Fabry-Pérot mode, and the guided-mode resonance which is caused by the periodic modulation. The GMR mode is reminiscent of a Surface-Bloch Wave[6], but here it is supported in the cavity formed by the

interface of the two cavity mirrors rather than just at the surface of a single mirror. An example of a surface-Bloch wave GMR (with just one DBR mirror) is shown in Fig. 5.2, displaying a the characteristic Fano lineshape and resonant field.

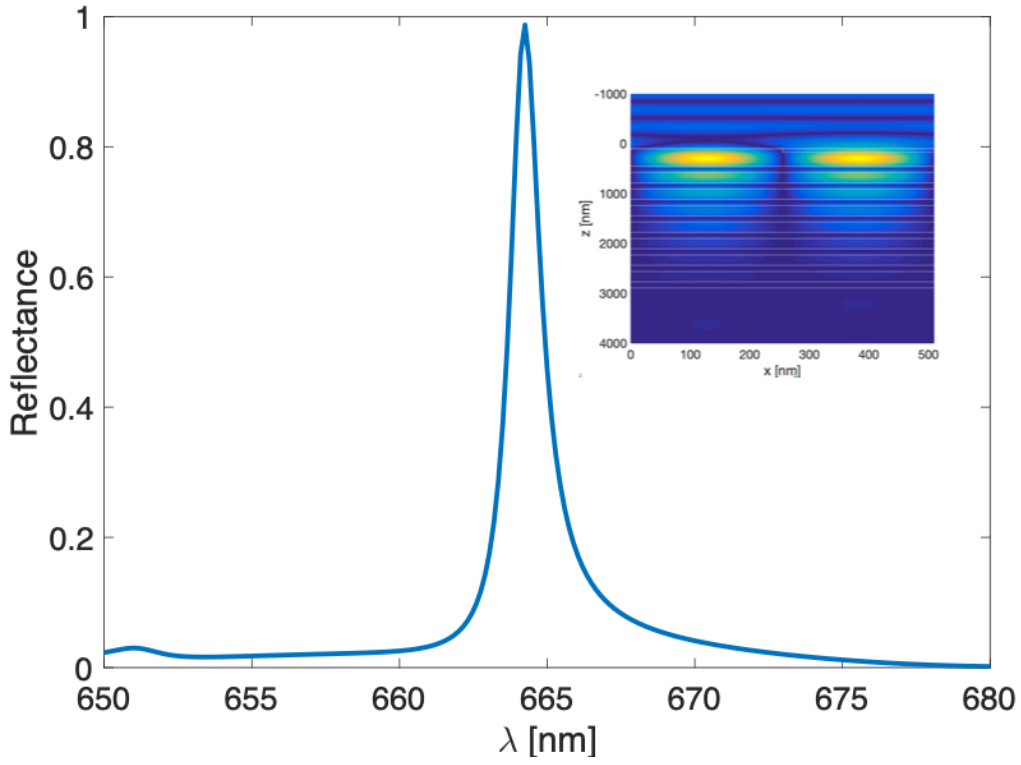

Figure 5.2: An example of the spectrum of a guided-mode resonance photonic crystal etched into a DBR mirror (inset) the associated electric field distribution.

To explore the possibilities of this structure, we'll examine the case of simultaneous enhancement at both ω_1 and ω_2, for either simultaneous Purcell enhancement or simultaneous strong coupling. This is shown in Fig. 5.3 , where we see the clear signatures of both the FP mode in the DBR stopband, as well as the Fano resonance corresponding to the GMR. In Fig 5.3a-b, we can see that the electric field distributions are both tightly confined around the location of the material, and both modes have field distributions that are tightly confined around the active material and are near the field maximum.

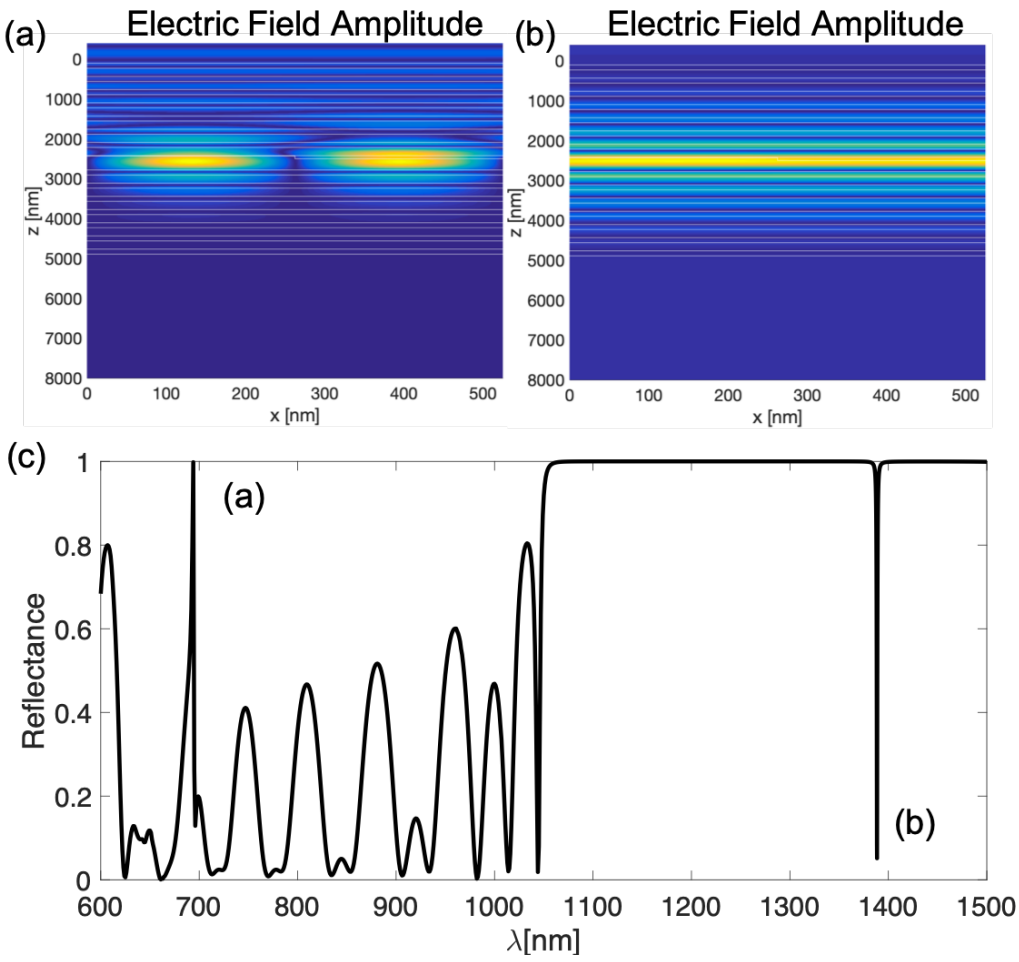

Figure 5.3: (c)Spectrum showing the presence of both a guided-mode resonance (a) and Fabry-Pérot mode (b). The associated field distributions are plotted, showing that both are concentrated in the layer where the excitonic material is located.

Finally, we'll show that these modes are very easy to tune across a very wide spectral range, covering a range of experimentally relevant energy gaps between various emitters. In Fig. 5.4, we show a map of the reflectance spectrum as a function of the modulation period Λ. We show that by adjusting Λ over a wide range, we can continuously tune the GMR mode over a very wide energy range, while leaving the Fabry-Pérot mode essentially unchanged. This is due to the different origins of the modes: the periodic modulation is simply a weak perturbation on the FP mode, whereas it is a critical part of the formation of the GMR mode. Over this

range, both modes remain well-confined, and have a high quality factor. To have this degree of tunability of multiple modes simultaneously is not easy to accomplish with a traditional cavity, such as the one in Fig. 5.1a, but it is very easy to achieve with our structure.

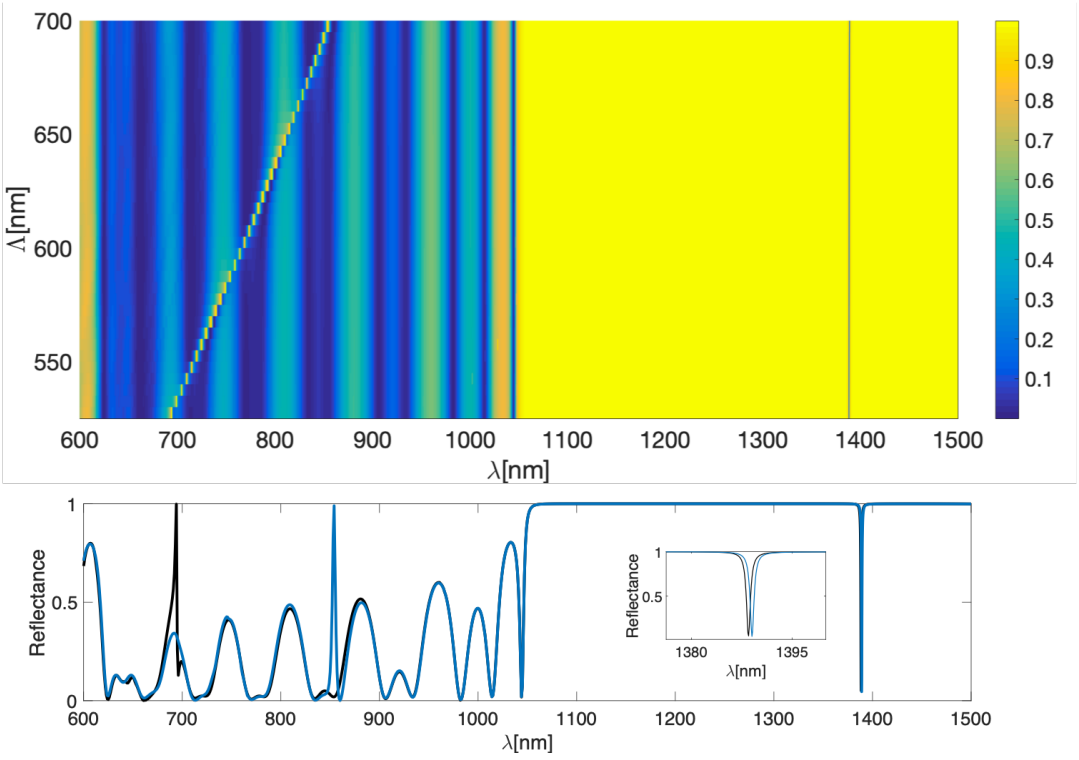

Figure 5.4: (top) A sweep of the grating period Λ, showing the tunability of the GMR type resonance, while the FP type resonance is largely unchanged (bottom) A line cut of the two extreme values in this sweep (inset) a zoom-in on the FP modes, showing the slight displacement of the mode.

Finally, we adjust the patterning to bring the states even closer by further increasing Λ. In Fig. 5.5, we can see that by adjust the patterning we have tuned the mode inside the photonic bandgap, and that now the modes are separated by only about 40 meV. At this detuning, we still see high-Q resonances, which have a strongly confined field distributions centered around the active material layer. A notable feature is that once the modes have been brought this close together, there is a clear modification of the electric field distribution for the DBR-type mode, but

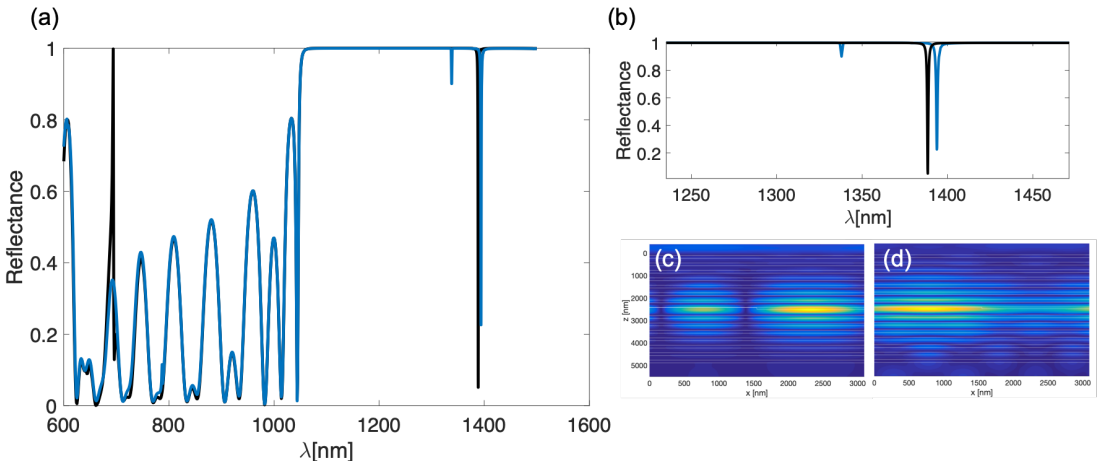

Figure 5.5: (a) A comparison of the cavity with $\Lambda = 525$nm and $\Lambda = 3095$nm, showing the range of tunability of this mode. The mode spacing in the latter case is just 40 meV, compared to the former case, where it is on the order of a full eV (b) Zoom in of the FP modes (c-d) Electric field distributions of the two blue dips in (b), showing that the resonant field his still strongly confined near the center of the cavity, although the DBR field is modified from the unpatterned field.

nevertheless the field distribution is favorable for coupling to the active material.

5.3 Conclusions

In conclusion, we have demonstrated the design of a hybrid, dual-band cavity which has a much higher degree of tunability in terms of both the spectral properties, as well as the associated electric field distribution. This allows for a degree of tunability which is not possible in a traditional optical cavity, and opens a pathway to further engineering the radiative properties of multiple emitters in optoelectronic systems.

CHAPTER VI

TMDC Heterostructures

6.1 Introduction

As discussed in Chapter 2, one of the interesting properties of TMDCs is their ability to be combined into arbitrary heterostructures with novel electronic and optical properties. In this chapter, we will present experimental results of the helicity-resolved photoluminescence which clearly demonstrates the interesting optical selection rules which are present in these heterostructures, along with a high degree of valley polarization (these measurements were conducted as part of [94]). Then we will present some calculations of the electronic and optical properties of TMDC moiré heterostructures.

6.2 Experimental Results on $MoSe_2/WSe_2$ Heterobilayers

6.2.1 Overview

Here we will present experimental results of low-temperature photoluminescence measurements on $WSe_2/MoSe_2$ heterobilayers. The measurements which are presented here are done on the same samples as in [94], which were fabricated by a collaborator with our group who is co-authored on this paper. An image of the heterostructure being measured is shown in Fig. 6.1, with the various different layers outlined. We are interested in the portions of the sample where the bilayer is fully

encapsulated by the boron nitride. The encapsulation of the heterobilayer in hexagonal boron nitride helps reduce the broadening of the exciton peaks significantly, and allows us to easily resolve features that would otherwise have a strong overlap. The two individual monolayers are aligned such that they are oriented at roughly 60° relative to each other, which ensures that there is a small momentum mismatch between the electron and holes.

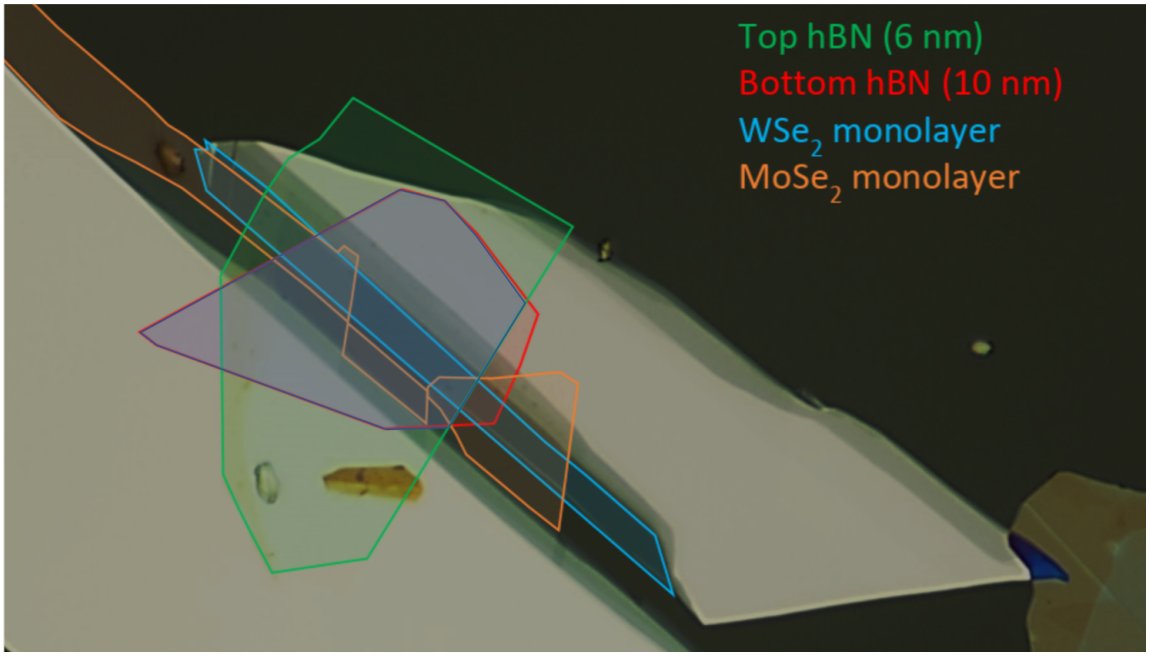

Figure 6.1: A optical microscope image showing the heterostructure measured in this section. The various regions of the sample are labeled

6.2.2 Results

The main optical property we are interested in here is the circular-polarization resolved photoluminescence. The samples are cooled down to 4K, and pumped using a tunable CW Ti-Sapphire laser, tuned to the wavelength which maximizes the emission helicity, which in this case is the WSe_2 A exciton energy. In simpler systems like single monolayers, the optical selection rules dictate that the emission should be co-circularly polarized, but as we can see in the results in Fig. 6.3, the interlayer

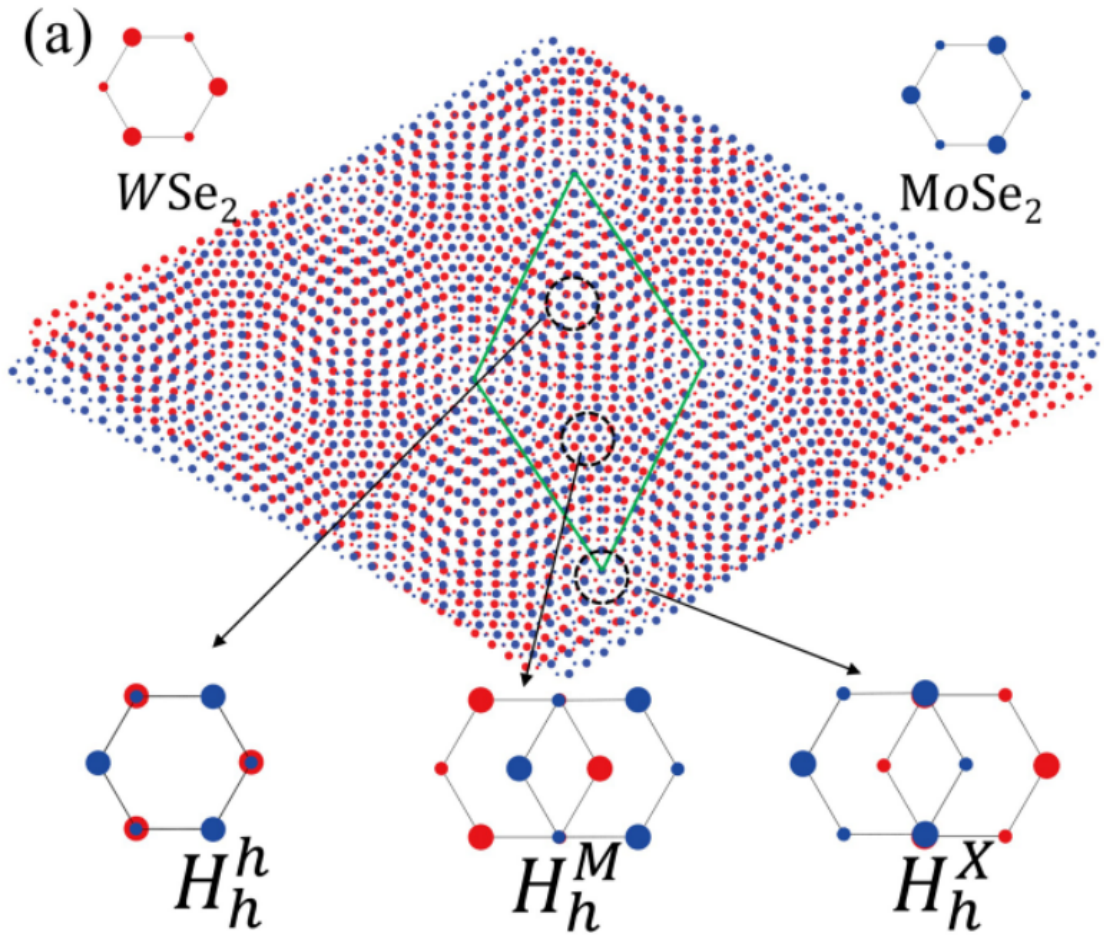

Figure 6.2: A schematic of the moiré structure formed in the $MoSe_2/WSe_2$ heterobilayer, with the three high-symmetry registries labeled Reproduced from [94].

excitons are very different. There are two peaks, one of which is largely co-circularly polarized and the other which is largely counter-circularly polarized, and both of which display high degrees of polarization over 80%. The expected results in heterostructures is much more complicated in general than in the single monolayer, and there are many different possibilities for what the optical response can look like. In this case, the multiple exciton peaks with flipped helicities can be explained as originating from singlet and triplet excitons, which are theoretically predicted to display this particular behavior at the H_h^h registry in the moiré lattice[94], which is shown

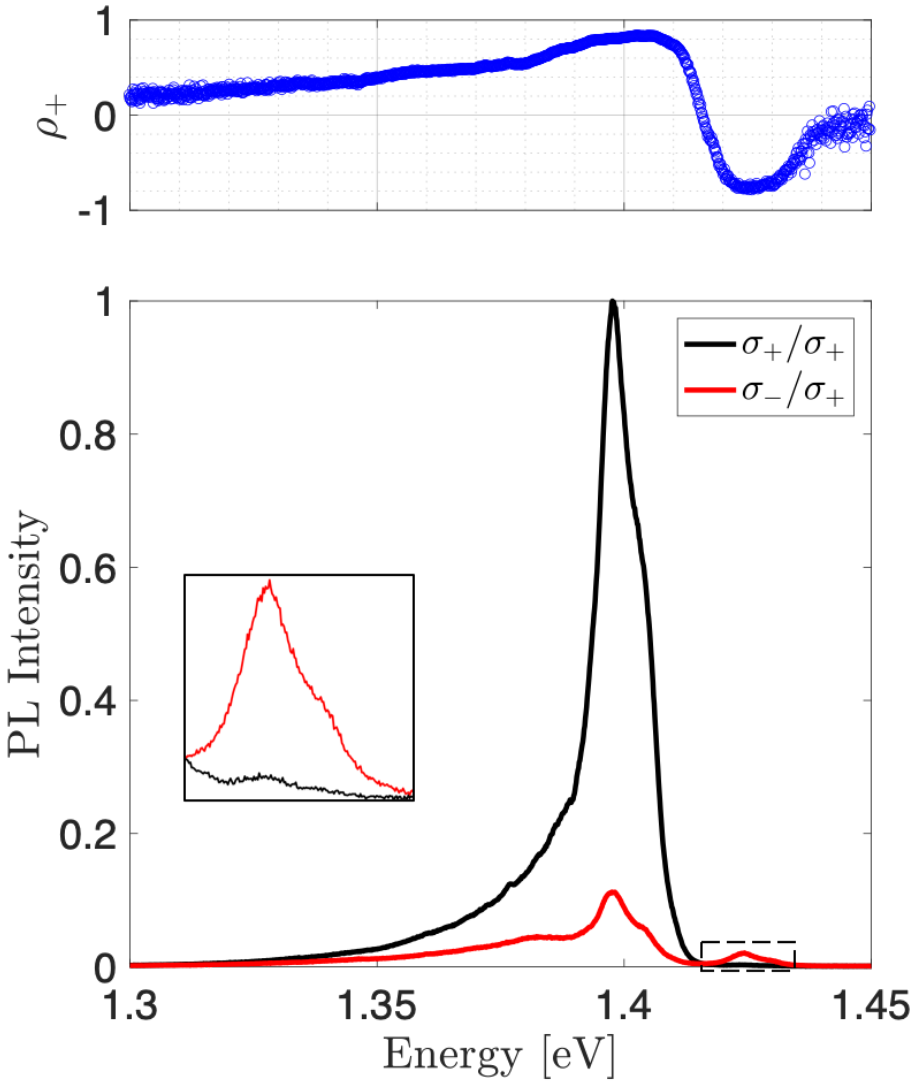

Figure 6.3: The measured polarization-resolved photoluminescence from the heterobilayer sample. (top) The extracted degree of polarization, showing near-unity positive and negative polarization (bottom) The spectrum for both co- and cross-polarized collection of the emission.

in Fig. 6.2. The other two high-symmetry points do not have selection rules that agree with our observations; at these sites the singlet and triplet excitons couple in either the opposite way as we observed, or they couple to out-of-plane light. The observed high degree of valley polarization present in this sample (along with additional time-resolved measurements done in [94]) suggest that there is a rapid electron

transfer between layers, which is significantly faster than the WSe_2 intralayer exciton depolarization time.

6.3 Theoretical Predictions of Heterobilayer Physics

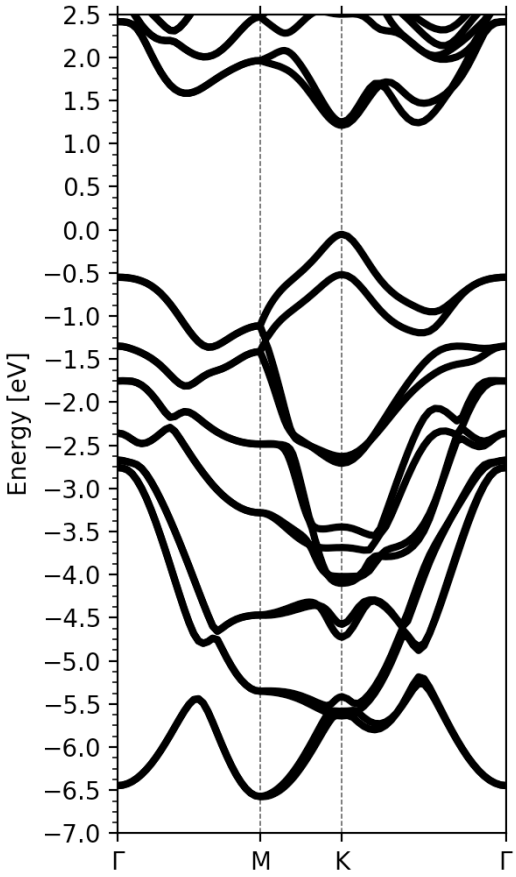

Figure 6.4: The band structure of monolayer WSe_2 (calculated with Quantum Espresso), showing band structure along the irreducible Brillouin zone.

In order to predict the theoretical properties of TMDCs and their heterostructures, an invaluable tool is the Density Functional Theory (DFT) calculation, which can be used to calculate the electronic band structure of materials, among other properties. The calculations presented here are done with the open-source DFT package Quantum Espresso, a popular choice for doing DFT calculations. As a basic

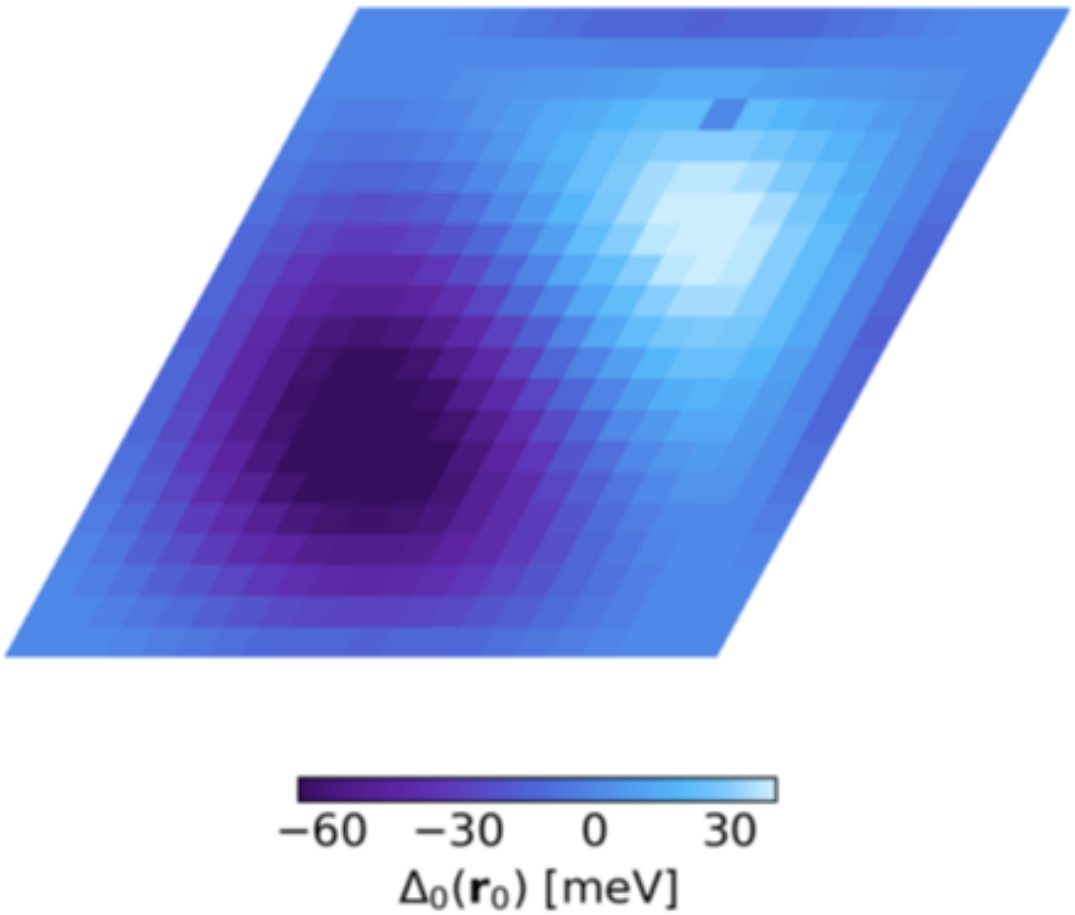

Figure 6.5: The calculated spatially dependent bandgap for an AA stacked $WSe_2/MoSe_2$ heterostructure. The calculation was done using Quantum Espresso. There was a single calculation which failed due to a crashed program, which is the one discontinuous point on the mapping.

example, we can calculate the band structure of monolayer WSe_2, which is shown in Fig. 6.4, in excellent agreement with expected results from the literature (for instance, in [46]). We can clearly see all of the important features in the electronic band structure, such as the direct bandgap at the K point and the large splitting on the order of .5eV in the valence band. Although this calculation is just done for a single monolayer of WSe_2, we can extend the calculations to explore the effect of modifications of the material structure, such as applied stresses and strains or the introduction of other materials in the vicinity of the monolayer.

Moving beyond the simple monolayer, we can begin to explore the theoretical predictions made when heterobilayers are constructed, where we combined two different group VI TMDCs together. Many of these predictions rely on the existence of moiré lattices forming when the two monolayers are integrated with each other, and which generally form due to a combination of lattice mismatch and finite twist angle. These moiré heterostructures have a spatially varying bandgap[90], which can be calculated via DFT calculations in order to understand the strength of the moiré potential. We calculate the moiré potential strength in Fig. 6.5 of an AA stacked heterobilayer of $MoSe_2/WSe_2$, following the prescription in [90][89]. What we are calculating here is the bandgap magnitude as a function of the offset of one monolayer relative to the other monolayer, which determines the underlying moiré potential[90]. It is in excellent agreement with the results in [90], showing a moiré potential depth on the order of about 100 meV.

Additionally, we can go beyond calculations of the electronic properties and calculate the direct optical properties of the heterostructures as well. Here, we follow the theoretical work developed in [89] to calculate the exciton band structure and absorption of intralayer excitons as a function of twist angle in an AA stacked MoS_2/WS_2 heterobilayer. The Hamiltonian is

$$H = H_0 + \Delta(r)\tau_0$$

with

$$H_0 = \left(\hbar\Omega_0 + \frac{\hbar^2\mathbf{Q}^2}{2M}\right)\tau_0 + J|\mathbf{Q}|\tau_0 + J|\mathbf{Q}|[\cos(2\phi_\mathbf{Q})\tau_x + \sin(2\phi_\mathbf{Q})\tau_y]$$

and

$$\Delta(\mathbf{r}) \approx \sum_{j=1}^{6} V_j \exp(i\mathbf{b}_j \cdot \mathbf{r}).$$

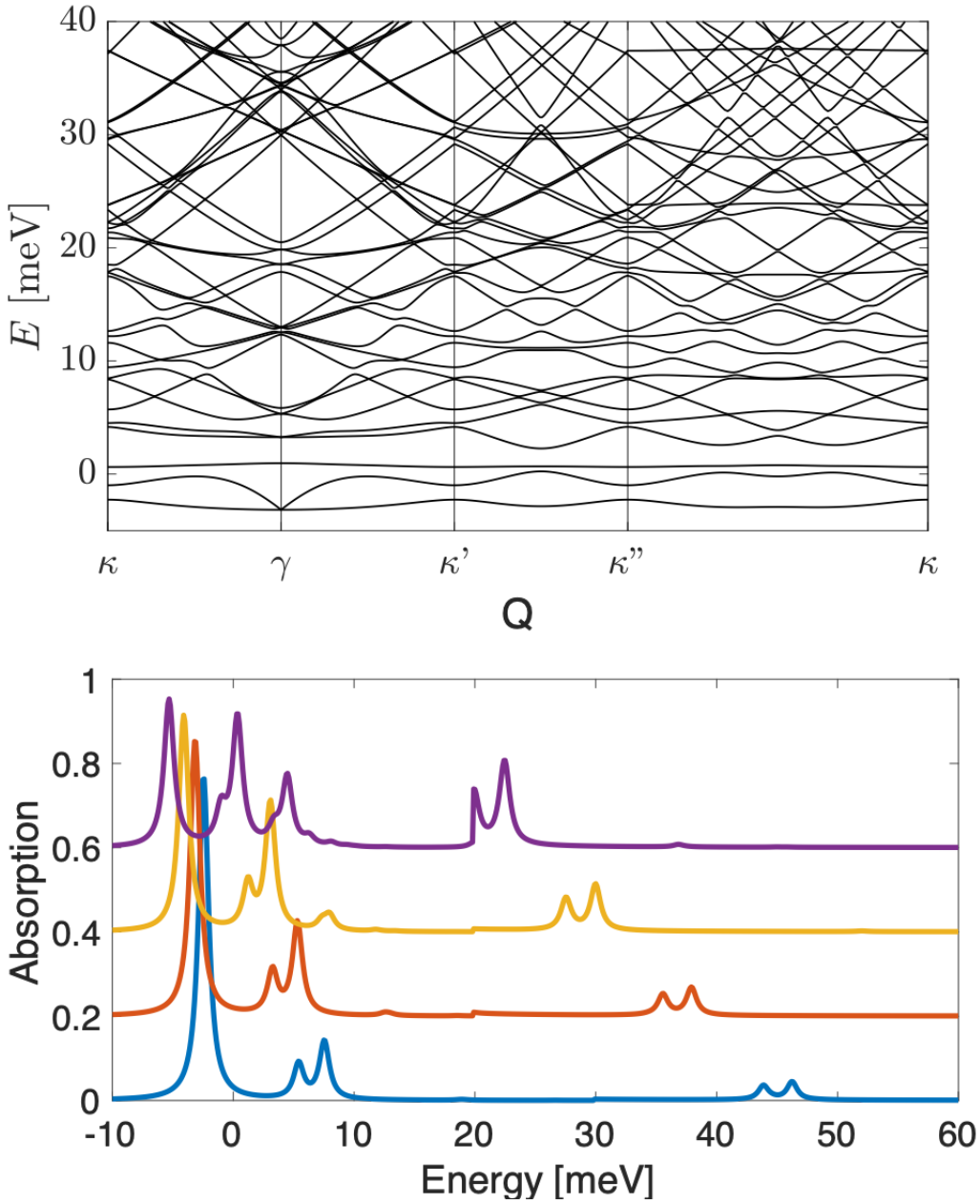

Figure 6.6: (top) Calculated moiré band structure at a twist angle of 1° (bottom)twist-angle dependent absorption spectrum for an AA stacked MoS_2/WS_2 heterobilayer.

Here, $\hbar\Omega_0$ is the energy at $\mathbf{Q} = 0$, τ_0 is the identity matrix (corresponding to the intravalley electron-hole exchange interaction), $\tau_{x,y}$ are Pauli matrices (corresponding to the intervalley exchange interaction), $\phi_{\mathbf{Q}}$ is the angle of the vector $\mathbf{Q}$, and J quantifies the strength of the electron-hole exchange interactions. Plugging in the

same material values as in [89], we can diagonalize the Hamiltonian and calculate the intralayer exciton band structure, as shown in Fig. 6.6. In order to perform the calculation, we have written a plane-wave expansion code in MATLAB, which diagonalizes the Hamiltonian and produces the band structures.

In addition to the exciton band structure, we can also calculate the absorption spectrum based on the calculated eigenvectors of the states at the γ point of the exciton band structure, as shown in the bottom panel of 6.6. Here the calculation is done for a range of twist angles, from 0.6° to 1.2°, in steps of 0.2° from top to bottom, and the highest energy peaks in each are multiplied by a factor of 10. This shows that the effect of the moiré lattice is to redistribute the emission to multiple peaks, which can shift in energy based on the twist angle of the heterobilayer. The results presented here use the same values as in [89] and thus are essentially a replication of their results, but can easily be modified in order to predict the behaviors of other combinations of monolayers.

6.4 Conclusions

In this section, we have explored a few different aspects of TMDC heterostructures. First, we presented experimental results which show that group VI heterostructures can support multiple different interlayer exciton states, some of which have interesting flipped optical selection rules which are not present in monolayers. The interlayer excitons also showed a very high degree of valley polarization of about 80%. Following this, we showed calculations of the moiré potential strength as well as the exciton band structure and absorption of moiré exciton states, showing the characteristic redistribution of the exciton oscillator strength across multiple mini-peaks which are tunable via twist-angle.

CHAPTER VII

Self-Hybridized Polaritons in ReS_2

7.1 Introduction

In this section, we will demonstrate self-hybridization of exciton states in ReS_2 flakes. Most of this work has been published in ACS Photonics [31] and is reproduced here.

Strong coupling between excitons and photons in a photonic cavity provides a promising platform for exploring a wide array of physical effects. To date, there are many examples of strong coupling in group VI TMDCs, but no examples of group VII polaritons have been demonstrated. Here, we show evidence of polaritons in ReS_2 flakes, where the photonic confinement arises from internal reflections within the flake itself, without requiring a separate cavity to confine the field. By examining several different samples of varying thicknesses (each thickness with a different intrinsic cavity mode), we vary the detuning and map out a polariton dispersion. The polaritons exhibit multiple peaks in the absorption spectra, a fact which may help elucidate the observed multiple resonances in similar group VII TMDCs. As a unique feature of the anisotropic crystal structure of group VII TMDCs, these polaritons inherit the underlying polarization dependence of the two lowest order bright ReS_2 excitons, displaying a polarization-tunable absorption, with maximum

absorption greater than 95%.

7.2 Self-Hybridized Polaritons in ReS_2

Transition Metal Dichalcogenides (TMDCs) have emerged as a new class of semiconductor materials with many unique properties. The most commonly studied TMDCs are monolayer crystals containing group VI transition metal (MX_2, M=Mo,W, X=S,Se) [55, 71, 56], since excitons in these four monolayer crystals feature high oscillator strengths, high binding energies, and narrow linewidth, making them attractive as optical materials. In particular, strong exciton-photon coupling can be established even at the room temperature in a variety of photonic structures [21, 50, 25, 95], opening the possibility of high-temperature polariton Bose-Einstein condensation, superfluid transport, lasing, matter-wave logic, and many other rich nonlinear phenomena. However, these group VI TMDCs become indirect bandgaps semiconductors when the crystals have more than one molecular layer. The need to exfoliate down to monolayer thicknesses and to integrate a monolayer crystal into additional cavities and other photonic structures, without significantly changing or degrading the crystal's properties, poses a technical challenge in the study and application of these materials.

A number of group VII TMDCs have also been shown to feature exciton transitions with large oscillator strengths in both bulk and monolayer forms [3], and have other interesting properties, making them potentially a more versatile alternative to group VI materials. As opposed to the hexagonal symmetry of group VI TMDCs, group VII TMDCs have a triclinic crystal symmetry[86] with a distorted 1T diamond-chain structure. As a result, the optical response is highly anisotropic, giving rise to

a myriad of unusual phenomena, such as non-degenerate linearly polarized exciton resonances [36, 3, 2, 39], selectively tunable optical Stark effect[69], anisotropic third harmonic generation[17], and anisotropic saturable absorption[59]. Many of these phenomena can be enhanced in the strong-coupling regime [88], but to date there have been no reports on coupling of these materials with cavities.

In thin crystals of group VII materials, the optical anisotropy leads to two prominent, non-degenerate linearly polarized exciton resonances [3, 39], but there is evidence in the literature of additional nearby resonances whose physical origin is not clear. For example, thicker samples of the related material $ReSe_2$ have been reported to exhibit multiple well-resolved additional nearby resonances, which vary from sample to sample in energies and spectral weights [2]. It was suggested that these additional resonances were due to breaking of the 2-fold spin degeneracy at the conduction and valence band extrema by exchange interactions. In ReS_2, however, similar splitting is not clearly evident [3, 39].

In this work, we demonstrate a similar set of closely spaced exciton peaks and show that they originate from strong-coupling between ReS_2 excitons and photons via self-hybridization [81, 63, 77, 96, 65, 76, 12, 24], without the need of an external cavity. The Fabry-Pérot cavity modes are formed within the TMDC crystal itself between its top and bottom interfaces due to the high refractive index of ReS_2. The polariton modes are identified by studying the variation of resonances in ReS_2 crystals of a variety of thicknesses. Notably, the self-hybridized polariton modes maintain the underlying polarization sensitivity of the excitons, and can achieve polarization-tunable absorptions greater than 95%. These results provide insight into fundamental excitonic properties of ReS_2 and open a door to developing optoelectronic devices which can exploit strong light-matter coupling in optically anisotropic materials.

7.3 Results and Discussion

7.3.1 Sample Fabrication

In this project, we will be interested in measuring the properties of ReS_2 flakes of a variety of thicknesses, on different substrates. The fabrication process used to make our devices follows the standard mechanical exfoliation procedure used with the group VI materials. We utilize repeated exfoliation between sheets of Polydimethylsiloxane (PDMS) in order to progressively thin down the ReS_2 until all large flakes have been visibly removed, then perform the final transfer onto the end substrate. The end result is large areas of the substrate covered in randomly arrange pieces of ReS_2, with varying thicknesses. The pieces are deposited in tightly packed clusters which can be separated by large distances, on the orders of mm, on the chip.

The two substrates which we use here are gold and sapphire. The higher reflectivity of the gold substrates makes them an excellent choice for the experiment, as it drastically improves the reflection at the bottom surface and allows us to significantly narrow the linewidth of the intrinsic optical mode. We also use sapphire as it is a standard choice of substrate for exfoliating TMDC materials, and will allow us to demonstrate that cavity effects are easily seen even in the absence of a high reflectivity substrate.

In Fig. 7.1 we show a typical optical microscope image of the samples on a gold substrate, with several candidate samples circled. Due to the high absorbance of the samples, when placed on a reflective substrate they often display bright, bold colors when observed under a microscope. In Fig. 7.2 we show a typical sample which was exfoliated onto the sapphire substrate. Since this method of preparation results in random thicknesses of ReS_2, getting appropriate thicknesses required in order to map out a thickness map is a matter of luck. Once the samples have been exfoliated, the

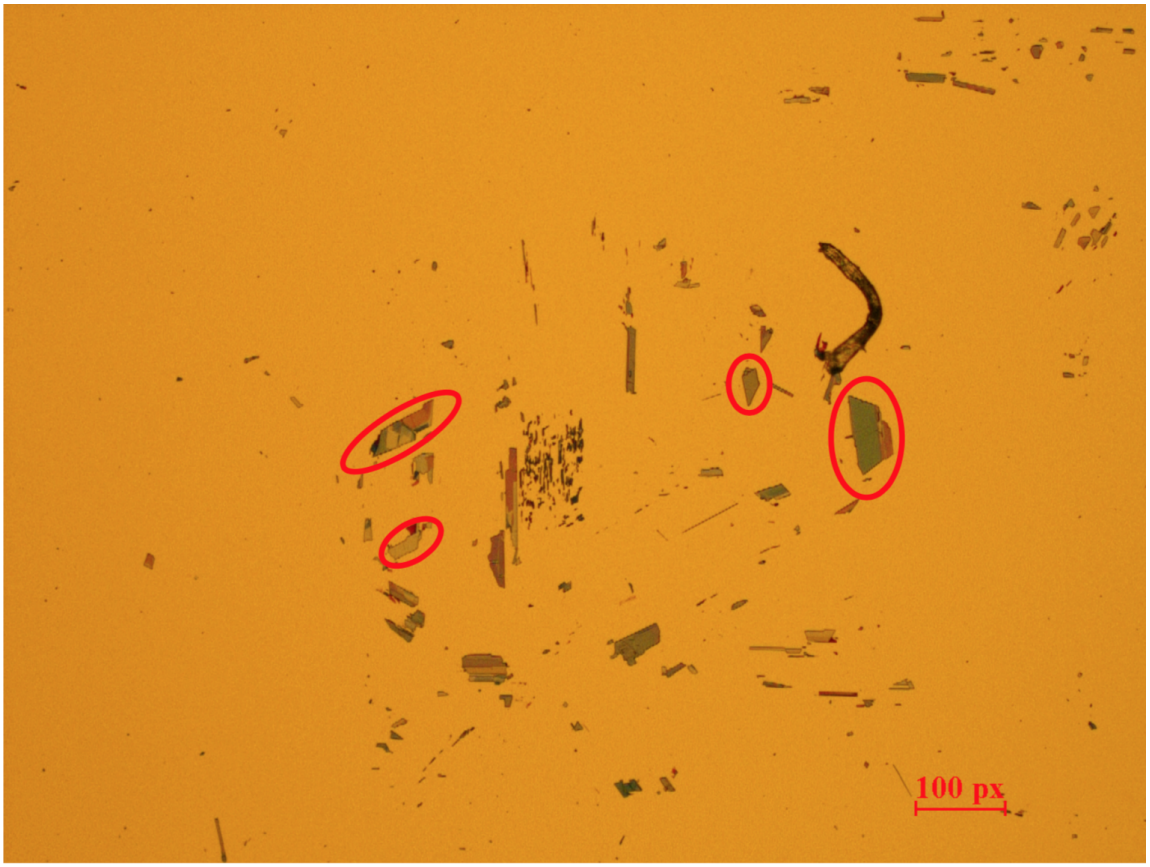

Figure 7.1: An optical microscope image showing a typical exfoliation of ReS_2 on a gold substrate.

thicknesses were then measured via Atomic-Force Microscopy (AFM) measurements (conducted by the second author of [31]). These measurements allowed us to compare the properties of different thicknesses directly, and map out our thickness sweep.

7.3.2 Optical Measurements

In Fig. 7.3a, we show a schematic of our device, where a single flake of ReS_2 is exfoliated onto a gold mirror. An optical microscope image of a typical device is shown in Fig. 7.3b. We characterize the devices via polarization-resolved absorption and photoluminescence (PL) spectroscopy.

Unless otherwise stated, all measurements were carried out at a temperature of 5K. Reflection and absorption measurements were taken with a halogen white-light

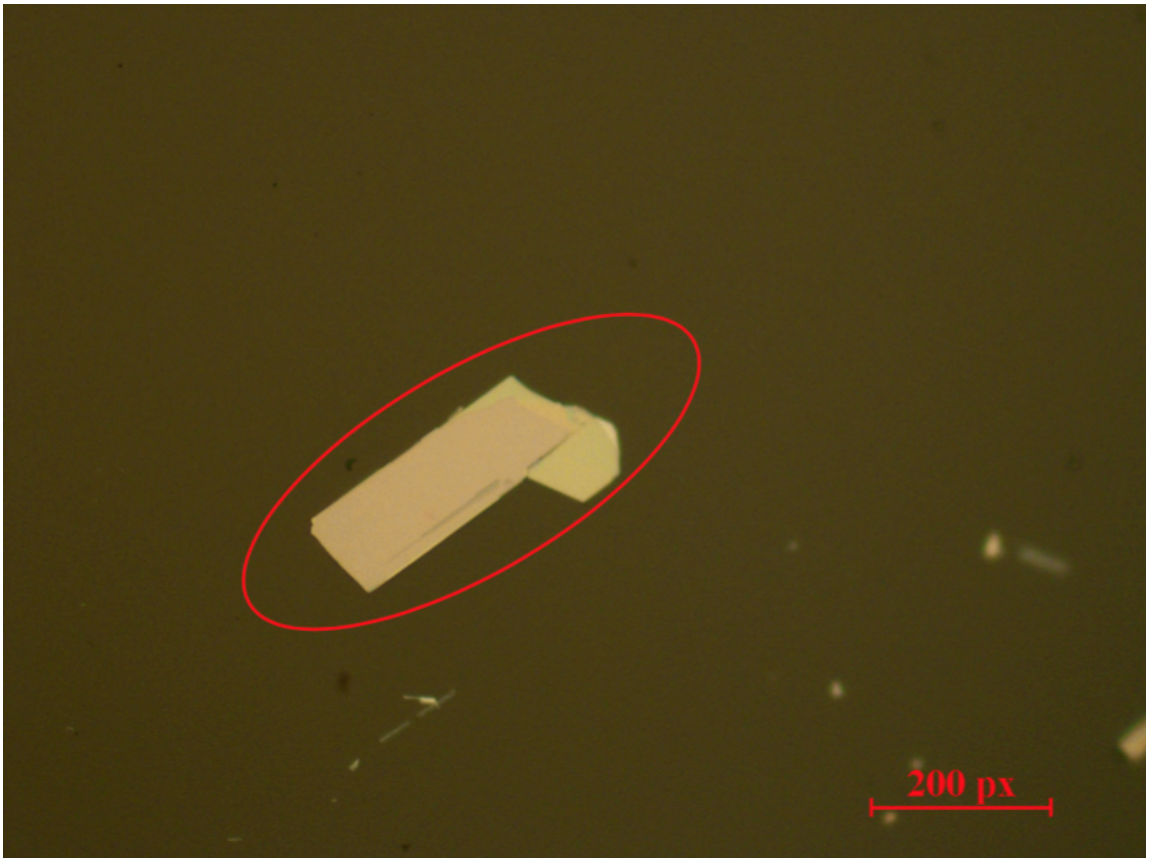

Figure 7.2: An optical microscope image showing a typical exfoliation of ReS_2 on a sapphire substrate.

source focused to a spot size of 10 μm, and PL measurements were performed by pumping the sample with a 532nm solid-state laser focused to a spot size of 2 μm. All measurements were done in a home-built optical microscope with an objective lens with NA=0.45. A half-waveplate and linear polarizer were inserted in the collection path to obtain the polarization-resolved absorption and reflection. The thicknesses of the samples were determined via AFM measurements.

We show in Fig. 7.4 the PL and absorption spectra of the device. As shown in Fig. 7.4a, the PL spectrum at 5 K, measured without polarization selectivity, has two pairs of peaks clearly separated by about 40 meV. Each pair contains two peaks about 10 meV apart. Fig. 7.4b. shows the temperature dependent absorption, also

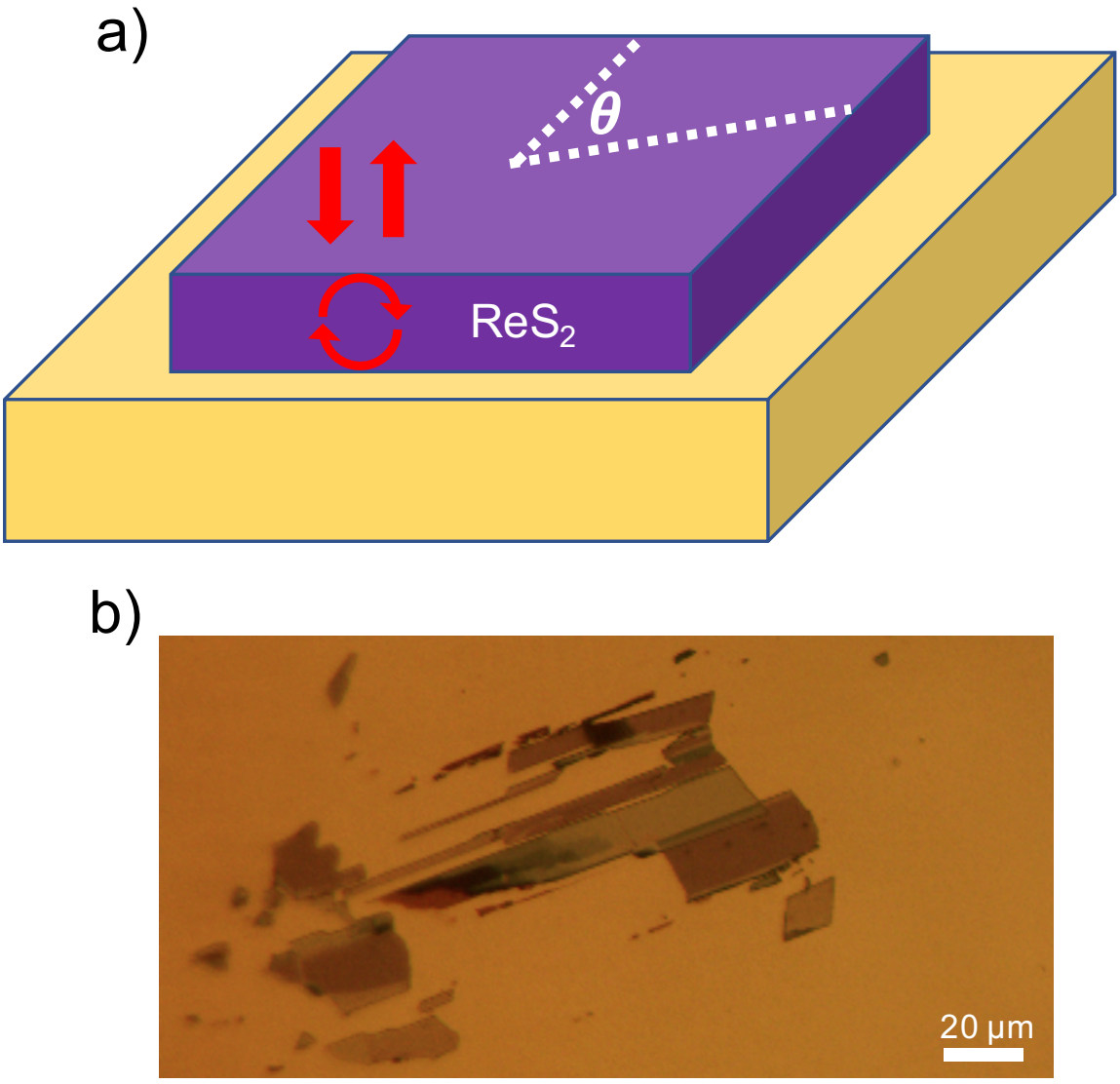

Figure 7.3: (a) Schematic of the device consisting of a ReS_2 crystal on gold. Reflections at the top and bottom surfaces of the crystal leads to confined photon modes, sufficient for achieving strong coupling with the excitons in the crystal. (b) An optical microscope image of a typical ReS_2 flake deposited on a gold substrate.

including all polarizations. The two pairs of resonances in the PL spectrum are clearly seen in the low-temperature absorption spectrum as well. With increasing temperature, the peaks broaden, and each pair merges into one broader peak instead. The presence of two broad absorption resonances in thicker samples at room temperature agrees well with previous reports.

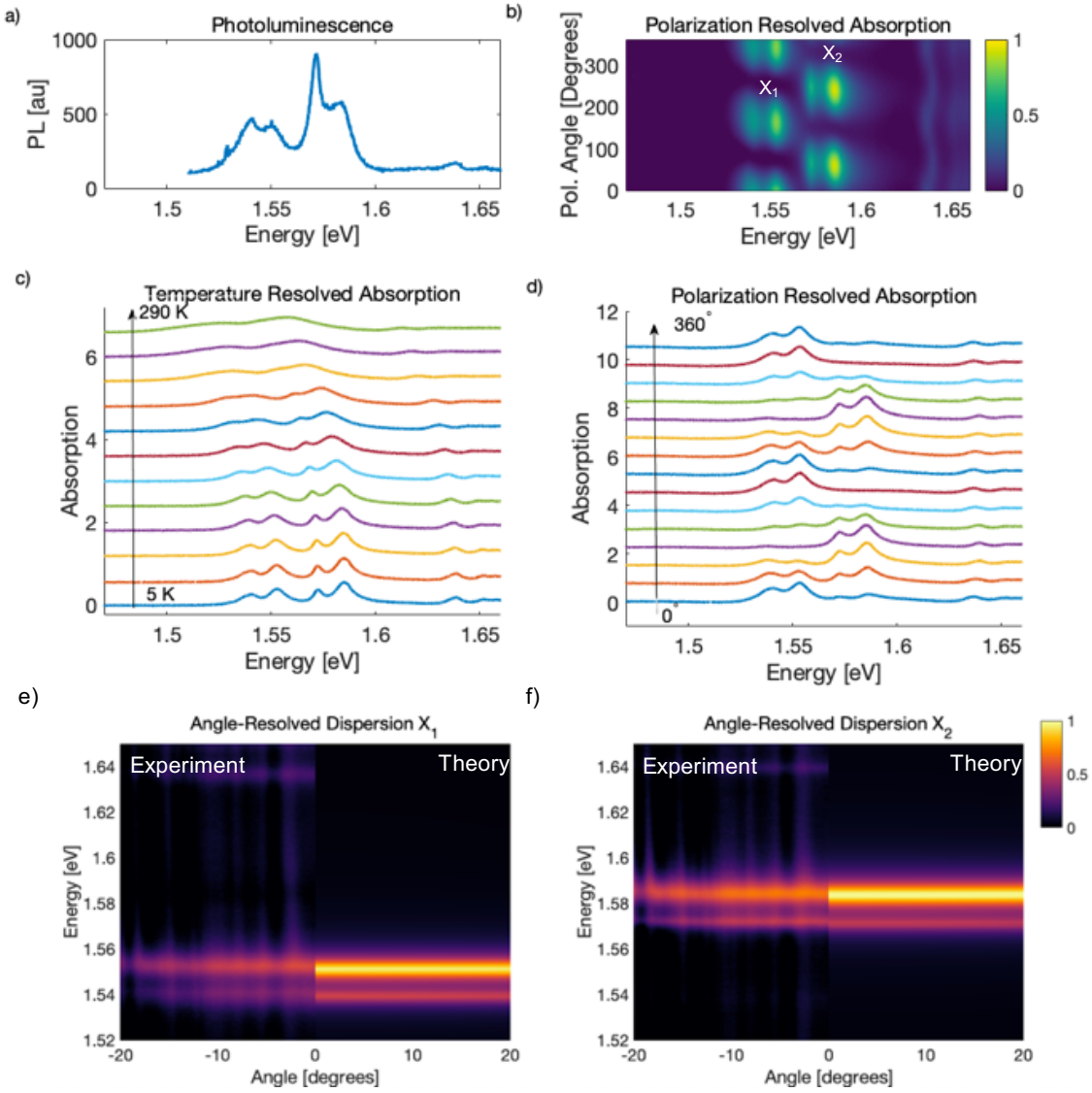

Figure 7.4: (a) Unpolarized PL of the 72nm flake shown in Fig. 7.3, at 5K. (b) Temperature dependent unpolarized absorption from the same flake up to room temperature, showing the splitting vanish at higher temperatures. (c) Polarization-resolved absorption of the same flake. (d) Line cuts of the polarization angle-resolved absorption from (c). (e-f) Measured angle-resolved dispersion from the same flake, for each of the two underlying excitons, compared to the theoretical predictions from a transfer matrix calculation.

To identify the origin of the resonances, we measure absorption of different linear polarizations. As shown in Fig. 7.4c,d, the two pairs of peaks as measured in Fig. 7.4a,b are clearly resolved. Interestingly, while the two peaks in each pair have about the same linear polarization, the polarizations of the two pairs differ by about 74°,

which also agrees well with previous reports of polarization properties of the two exciton resonances [69]. As shown in Fig. 7.4c, we label the lower energy pair of peaks as arising from the splitting of the underlying exciton X_1, and the higher energy pair as arising from X_2.

Mode splitting is a characteristic of strong coupling of excitons with photons. The properties of strongly coupled modes can be analyzed using transfer-matrix simulations, where the bare exciton resonances, X_1 and X_2, can be modeled using Lorentz oscillators, with the dielectric function given by

$$\varepsilon_{1,2} = \varepsilon_{B_{1,2}} + \frac{f_{1,2}}{E_{X_{1,2}}^2 - E^2 - iE\Gamma_{1,2}}.$$

Here, ϵ_B is the background permittivity, E_X is the exciton resonance energy, Γ is the linewidth, and f is the oscillator strength. To clarify if strong-coupling is the origin of the multiple resonances, we measure the dispersion and thickness dependence of the mode and compare them with simulations. The fitted values used for the excitons (X_1, X_2) in our calculations are $\epsilon_B = (17, 14)$; $\Gamma = (5, 5)$ meV, $E_X = (1.5431, 1.5744)$ eV, and $f = (0.325, 0.3)$ eV^2.

We first compare the calculated and measured energy-momentum dispersion of the device, which is widely used to identify polaritons formed in external Fabry-Pérot cavities. We measure the energy-momentum dispersion via angle-resolved spectroscopy, and we use a linear polarizer to maximize the spectral weight of the X_1 (Fig. 7.4e) and X_2 (Fig. 7.4f) peaks, respectively. To compare with the data of the lower-energy mode, associated with X_1, we set $f_2 = 0$ in the simulation. As shown in Fig. 7.4e, the calculated dispersions agree well with the experiment data. Similarly, considering only X_2 renders dispersions matching well with the measured dispersions of the higher-energy peaks. However, the dispersion is very flat, making it impossible to observe anti-crossing of the modes with angle. Rather than mapping

out polariton modes via angle, we instead characterize the thickness dependence of the modes.

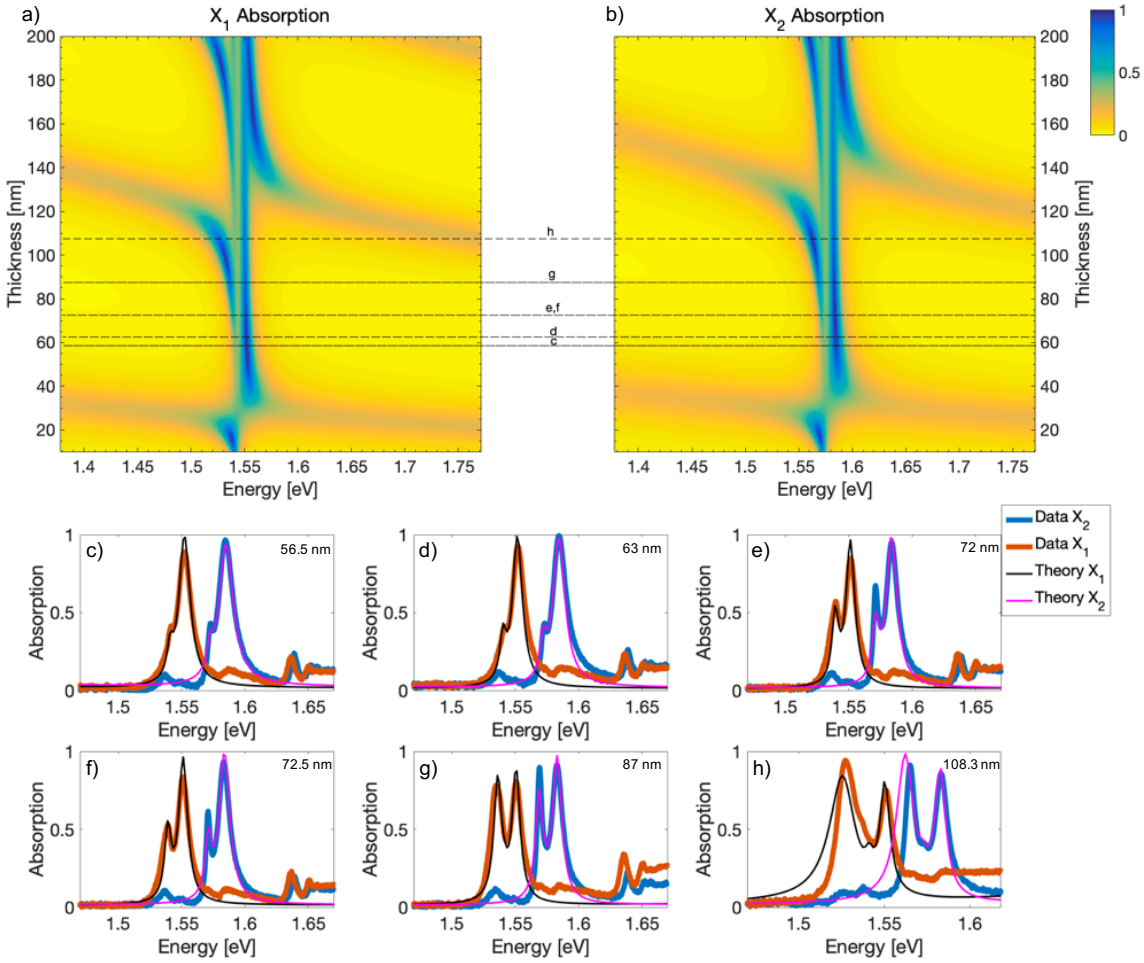

Figure 7.5: Polarization dependent thickness sweep of ReS_2 absorption. (a-b) Thickness tuning of the calculated absorption spectrum as a function of sample thickness, showing an effective dispersion and anti-crossing as the photon modes cross each of the two excitons X_1 and X_2. (c-h) Linecuts of the absorption spectrum for samples of different thicknesses (labeled in (a-b) with dashed lines). Each plot shows two prominent pairs of peaks, with each pair corresponding to the two underlying exciton modes. For each flake, selecting each exciton is done by rotating the polarization collection angle that maximimizes the signal for that pair of peaks. The data are overlaid with line-cuts from from the transfer matrix calculation in (a-b) showing good agreement between the two.

Figure 7.5a and b show the calculated absorption spectrum versus the thickness of the crystals due to exciton resonances X_1 and X_2, respectively. These calculations reveal the anti-crossing of the photon modes with each of the excitons. We have ex-

perimentally measured six samples with different thicknesses, marked as (c-h) in the bottom panel, and compared with the corresponding line-cuts of the calculated spectra in Fig. 7.5a and b. Each spectrum is taken at the polarization which maximizes that particular exciton absorption signal. We find excellent quantitative agreement between our model and the measured absorption for all six different thicknesses, which confirms that the different peaks of the same polarization are polariton modes formed by coupling with different photon modes. It is important to note that the observed splitting here is different from what is typically measured in conventional polariton systems: the split peaks are not the upper and lower polaritons directly, but instead are the highly detuned upper polariton from one photonic Fabry-Pérot mode, and the lower polariton from the next order Fabry-Pérot mode, as is evident in Fig. 7.5a, b (a more detailed explanation of this can be found in the next section). Notably, the absorption magnitude is very large, greater than 95% in some of the samples.

We note that similarly split peaks have been reported in crystals of a related group VII material, $ReSe_2$ [2], of comparable thicknesses used here. Although these resonances were attributed as excitonic, it is possible they could be explained by the polaritronic effect demonstrated here. In a more recent paper where the absence of these four peaks in multiple ReS_2 samples are discussed [39], all the samples used are all thin enough so that multiple polariton resonances are not expected based on our analysis.

Finally, we also characterize a 128 nm thick flake of ReS_2 on sapphire to show that the same effect is still observable without a gold substrate. For this sample, we measure the reflection contrast since it is difficult to extract the absorption from a sample with a transparent substrate. As shown in Fig. 7.6, we see clearly presence

of multiple resonances in the vicinity of the two bare excitons, and the spectra match very well with our model. This shows that even without a gold substrate, a similar strong modification of the spectrum is present (i.e., an apparent splitting of the exciton resonance), due to the cavity effect caused by reflections within the flake.

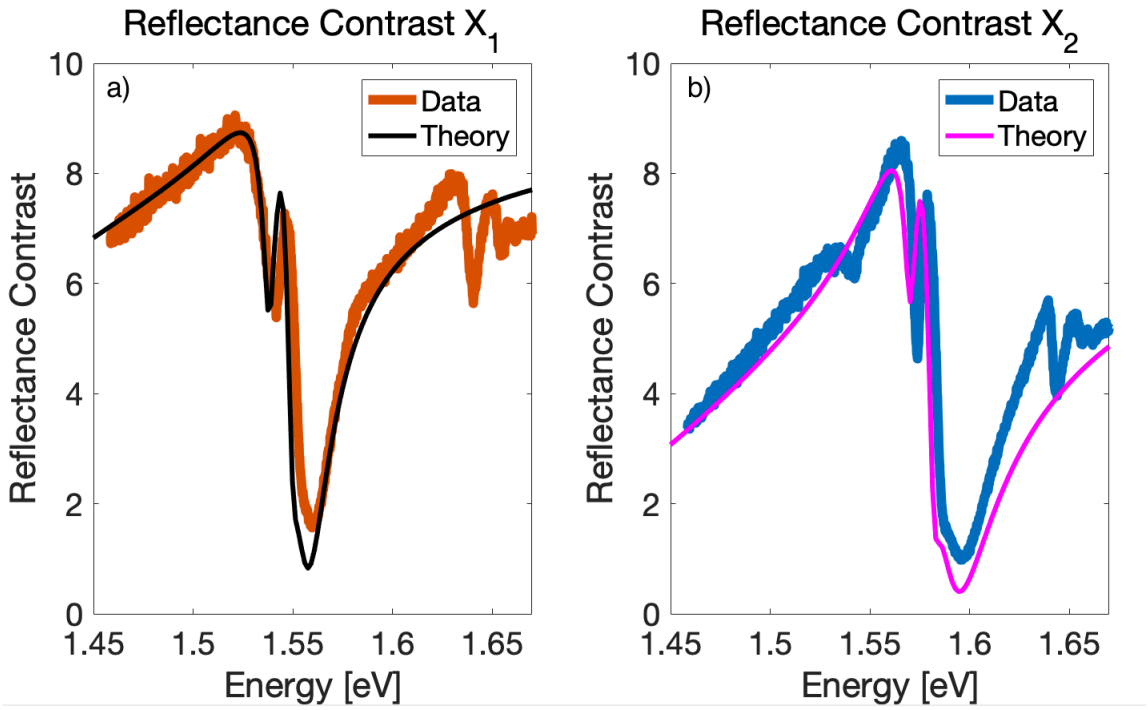

Figure 7.6: Measured and calculated reflectance contrast spectra for a 128nm thick ReS_2 sample on sapphire, showing the reflectance contrast for both exciton 1 (a) and 2 (b). The data in each plot shows the spectrum at a specific polarization angle, which selects for each of the underlying excitons, as in Fig. 7.5.

7.4 Clarification of Cavity Properties

7.4.1 Bare Cavity

In the section, we will show results to elaborate on the properties of the primary structure presented in the main text, a cavity formed between a gold substrate and a flake of ReS_2 (the Au/Interface cavity). For comparison, and as a reference to compare the results to, we also show results for a more traditional FP cavity with two gold mirrors (the Au/Au cavity). Both are shown in Fig. 7.7.

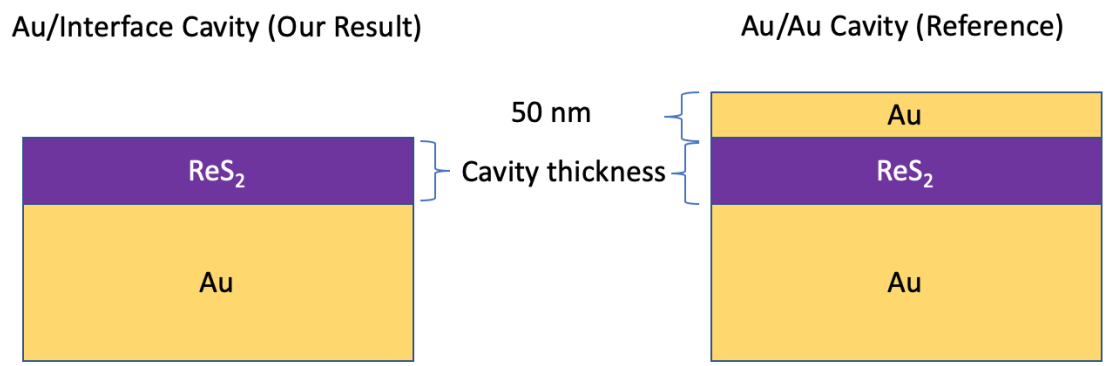

Figure 7.7: A schematic showing the difference between the cavity studied in our experiments (left) and the reference cavity we compare it to (right).

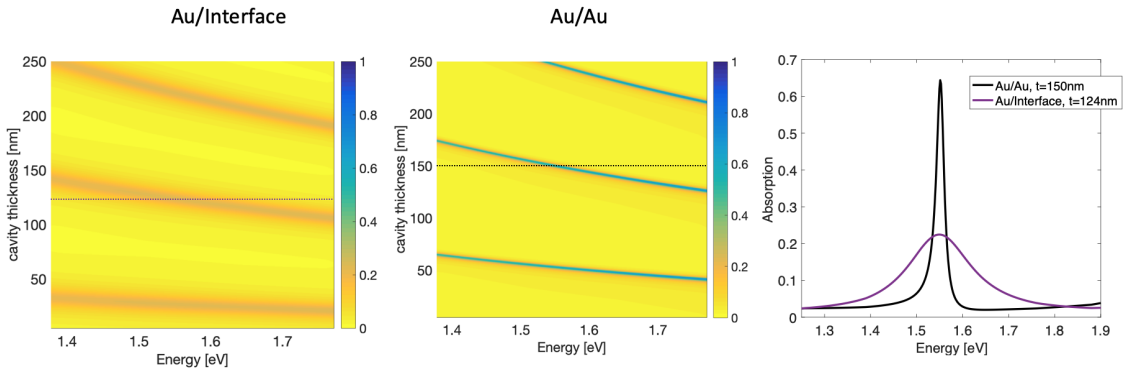

Figure 7.8: (left) The bare cavity modes for our structure (middle) The bare cavity modes for the reference cavity (right) Line cuts for both cavities, showing a mode at 800nm.

To begin with, we calculate the modes of the bare cavities, as a function of both energy and cavity thickness, as shown in Fig 7.8. For these calculations, we will take the material properties of X_1 as given in the main text, and for the bare cavity we set $f_1 = 0$ in order to just see the properties of the background material without the exciton resonance. As we tune the thickness, we see a set of modes for each, and it is clear that the Au/Interface cavity has a significantly reduced quality factor due to the lower reflectivity of the top ReS_2/Air interface. For the following calculations where we look at a single device, we select cavity thicknesses for each cavity that

give a resonance which is approximately at 800nm, in order to easily compare the two. The Au/Interface cavity has a very low Q of about 10. Despite the low quality factor, we will show that such a structure is still in the strong-coupling regime.

7.4.2 Cavity with Excitons

Now we consider the case where $f_1 \neq 0$. When the exciton resonance is turned on, there is a strong modification of the thickness mapping for both cavities, as shown in Fig. 7.9. We have included overlaid lines to indicate the uncoupled cavity photon modes (dashed) and the coupled polariton modes (dotted), and different colored the lines to correspond to different mode orders.

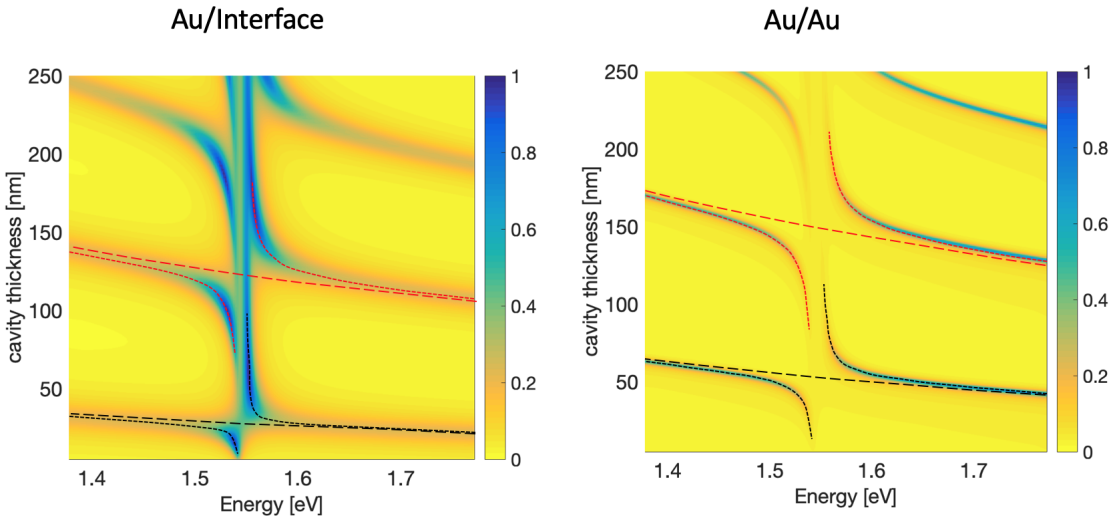

Figure 7.9: Thickness sweep of the loaded cavity from our results, and the reference cavity. In both, different FP mode orders are labeled with different colors, and the uncoupled modes (dashed) and coupled modes (dotted) are also labeled

We can see that there is a clear anti-crossing of the photonic modes as they approach the exciton resonance near 1.54 eV. Importantly, if we look at a single cavity thickness for the Au/Interface cavity (say, near 70nm), the line cut will show multiple resonances: one coming from a higher order mode (the red branch), and one from the lower order mode (the black branch). These two peaks are not the

upper/lower polariton modes for a single photonic resonance, but rather each comes from a different photonic resonance (one from the red branch, and one from the black), due to the effects of strong-coupling with the exciton. In the previous section, this is what we see in our data. At other thickness, say near 125-140 nm, we would be able to see split peaks where both originate from the same photonic mode (a more typical experimental signature for polaritronic systems). In our experiments, we did not have any samples which had an appropriate thickness to see this case.

7.4.3 Strong Coupling

In order to directly determine that a particular cavity is in the strong-coupling regime, we can sweep the exciton energy across the cavity mode to directly map out an anti-crossing for a single cavity thickness.

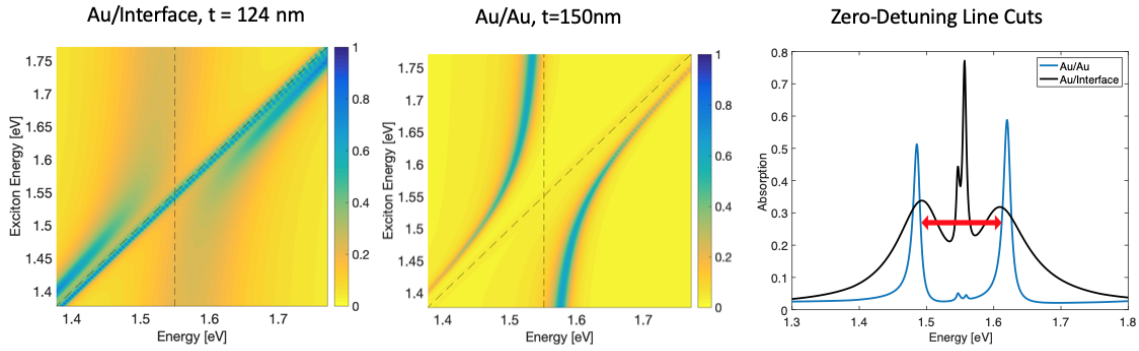

Figure 7.10: Exciton energy sweeps for the cavity in our result (left) and the reference cavity (middle). The linecuts at zero-detuning are shown in the right panel.

Although this is experimentally difficult to do for this system, we can easily calculate the results and show that this system is indeed in the strong coupling regime, as shown in Fig. 7.10. The peak splitting here for the Au/Interface cavity is $2\hbar\Omega \sim$ 115 meV (indicated by the red arrow). The condition for strong coupling is that

$$2\hbar\Omega > \gamma_X + \gamma_C$$

e.g. that the peak separation at zero-detuning must exceed the sum of the two half-linewidths. This condition is easily satisfied here, as our fitted value for γ_X is 2.5meV and γ_C for the bare cavity mode is about 90 meV, establishing that this system is in the strong-coupling regime.

7.5 Conclusions

In conclusion, we have demonstrated the observation of self-hybridized polaritons in multi-layer ReS_2 crystals. The resonances exhibit a clear polarization dependence of the polariton modes, reflecting the underlying polarization dependence of the two constituent excitons. Our samples which were deposited on gold exhibited a very high, polarization tunable absorption of over 95%, and showed tunability of the polariton modes by adjusting the sample thickness. These results may help clarify the origin of multiple peaks observed in these group VII samples, and pave the way for developing next-generation optoelectronic devices utilizing thin TMDC crystals.

CHAPTER VIII

Conclusions and Future Work

8.1 Conclusions

In this dissertation, we have demonstrated several experimental and computational results broadly related to the coupling of light and matter in two-dimensional semiconductors, with a particular focus on optical cavity design and the strong-coupling regime.

First, we demonstrated a new design for achieving strong coupling in these systems by integrating a single monolayer of group VI TMDC with the guided mode resonances of a photonic crystal. The design was optimized using RCWA simulations and was experimentally demonstrated, and has unambiguously shown the signatures of strong coupling. This demonstrates that photonic crystals are a viable polariton platform for these materials at both low temperatures and at room temperature. The fact that these polaritons exist at room temperature is particularly important, as it allows for the potential of exploring interesting polariton physics at room temperature.

Then, we introduced the design of dual-band cavities which are capable of supporting two optical modes that can be tuned independently of each other while maintaining a favorable electric field distribution, in order to achieve coupling be-

tween multiple different states in the same material. This opens the possibility of using the cavity to engineer the properties of multiple excitonic states which are present in a single material.

Following this, we presented some work on TMDC heterobilayers, including theoretical calculations of the expected moiré potentials experienced by interlayer excitons, as well as calculations of the exciton band structure and absorption spectra of intralayer moiré excitons. We also presented experimental work on measuring the helicity of heterobilayers which display a flipped optical selection rule compared to the bare monolayer, and which display high levels of valley polarization.

Finally, we demonstrated that the group VII material ReS_2 is capable of supporting self-hybridized polaritons, in which the interface of the flake acts as a mirror to create an intra-flake cavity effect. These results demonstrate that interesting photonic effects can be seen even when measuring just the flake itself, manifesting as a splitting of each of the bare excitons into a pair of resonances which inherit the underlying polarization of the excitonic state.

8.2 Future Work

Moving forward, there are many exciting possibilities for extending and expanding upon the work which has been presented in this dissertation. Firstly, it would be very interesting to experimentally achieve the goal of polariton lasing and Bose-Einstein condensation using our photonic crystal devices. It was only recently demonstrated[98] that condensation is possible at room temperature in a typical Fabry-Pérot type cavity, and experimental verification of this in our photonic crystal system would be make this a very useful platform to explore more complicated BEC physics, due to it's simplicity and on-chip tunability.

The dual-band cavities which have been described in this dissertation have never been fabricated, and it will be interesting to fabricate them and utilize them for coupling to multiple resonances in a single heterostructure. For example, we could place a heterobilayer into the cavity and couple to both underlying intralayer excitons at once.

With regards to the TMDC heterostructures, there is still a significant amount of interesting, unexplored physics to be done on both the existing heterostructures which have been looked at already, as well as the innumerable possible combinations of TMDCs and other 2D materials which are yet to be made. With regards to the heterostructure that we reported on here, the spatial distribution of the confined emission still has not been measured, due to the fact that the length scales of the moiré period are small (deep subwavelength), and thus not possible to resolve with conventional optics. It would be interesting to optically characterize the spatial distribution to be able to further investigate the properties of the moiré potential landscape.

Finally, there are many opportunities to further explore the physics of group VII TMDC materials. These are generally much less studied than their group VI counterparts, especially in regards to polaritronic physics, but are nevertheless an interesting material for these applications. Currently, as far as we are aware, there are no other demonstrations of strong-coupling in group VII materials other than our work, so it would be very interesting to see them integrated into proper external photonic cavities as well.

BIBLIOGRAPHY

BIBLIOGRAPHY

[1] Matthew J. Allen, Vincent C. Tung, and Richard B. Kaner. Honeycomb carbon: A review of graphene. *Chemical Reviews*, 110(1):132–145, 2010.

[2] Ashish Arora, Jonathan Noky, Matthias Drüppel, Bhakti Jariwala, Thorsten Deilmann, Robert Schneider, Robert Schmidt, Osvaldo Del Pozo-Zamudio, Torsten Stiehm, Arnab Bhattacharya, Peter Krüger, Steffen Michaelis de Vasconcellos, Michael Rohlfing, and Rudolf Bratschitsch. Highly Anisotropic in-Plane Excitons in Atomically Thin and Bulklike 1T-ReSe2. *Nano Letters*, 17(5):3202–3207, 2017.

[3] Ozgur Burak Aslan, Daniel A. Chenet, Arend M. Van Der Zande, James C. Hone, and Tony F. Heinz. Linearly Polarized Excitons in Single- and Few-Layer ReS2Crystals. *ACS Photonics*, 3(1):96–101, 2016.

[4] Ozgur Burak Aslan, Minda Deng, and Tony F. Heinz. Strain tuning of excitons in monolayer WSe2. *Physical Review B*, 98(11):115308, 2018.

[5] Daniele Aurelio and Marco Liscidini. Electromagnetic field enhancement in Bloch surface waves. *Physical Review B*, 96(4):1–7, 2017.

[6] Hajar Kaviani Baghbadorani, Daniele Aurelio, Jamal Barvestani, and Marco Liscidini. Guided modes in photonic crystal slabs supporting Bloch surface waves. *Journal of the Optical Society of America B*, 35(4):805, 2018.

[7] D. Ballarini, M. De Giorgi, E. Cancellieri, R. Houdré, E. Giacobino, R. Cingolani, A. Bramati, G. Gigli, and D. Sanvitto. All-optical polariton transistor. *Nature Communications*, 4, 2013.

[8] Fábio Barachati, Antonio Fieramosca, Soroush Hafezian, Jie Gu, Biswanath Chakraborty, Dario Ballarini, Ludvik Martinu, Vinod Menon, Daniele Sanvitto, and Stéphane Kéna-Cohen. Interacting polariton fluids in a monolayer of tungsten disulfide. *Nature Nanotechnology*, 13(10):906–909, 2018.

[9] Matthew Z. Bellus, Ming Li, Samuel D. Lane, Frank Ceballos, Qiannan Cui, Xiao Cheng Zeng, and Hui Zhao. Type-I van der Waals heterostructure formed by MoS2 and ReS2 monolayers. *Nanoscale Horizons*, 2(1):31–36, 2017.

[10] Pallab Bhattacharya, Thomas Frost, Saniya Deshpande, Md Zunaid Baten, Arnab Hazari, and Ayan Das. Room temperature electrically injected polariton laser. *Physical Review Letters*, 112(23):29–31, 2014.

[11] F. Cadiz, E. Courtade, C. Robert, G. Wang, Y. Shen, H. Cai, T. Taniguchi, K. Watanabe, H. Carrere, D. Lagarde, M. Manca, T. Amand, P. Renucci, S. Tongay, X. Marie, and B. Urbaszek. Excitonic Linewidth Approaching the Homogeneous Limit in MoS2-Based van der Waals Heterostructures. *Physical Review X*, 7(2):021026, 2017.

[12] Adriana Canales, Denis G. Baranov, Tomasz J. Antosiewicz, and Timur Shegai. Abundance of cavity-free polaritonic states in resonant materials and nanostructures. *arXiv*, 2020.

[13] Iacopo Carusotto and Cristiano Ciuti. Quantum fluids of light. *Reviews of Modern Physics*, 85(1):299–366, 2013.

[14] Haitao Chen, Vincent Corboliou, Alexander S. Solntsev, Duk Yong Choi, Maria A. Vincenti, Domenico de Ceglia, Costantino de Angelis, Yuerui Lu, and Dragomir N. Neshev. Enhanced second-harmonic generation from two-dimensional MoSe2 on a silicon waveguide. *Light: Science and Applications*, 6(10):e17060, 2017.

[15] S. Christopoulos, G. Baldassarri H??ger Von Hogersthal, A. J D Grundy, P. G. Lagoudakis, A. V. Kavokin, J. J. Baumberg, G. Christmann, R. Butte, E Feltin, J. F. Carlin, and N Grandjean. Room-temperature polariton lasing in semiconductor microcavities. *Physical Review Letters*, 98(12):1–4, 2007.

[16] Stéphane Collin. Nanostructure arrays in free-space: optical properties and applications. *Reports on Progress in Physics*, 77(12):126402, 2014.

[17] Qiannan Cui, Rodrigo A. Muniz, J. E. Sipe, and Hui Zhao. Strong and anisotropic third-harmonic generation in monolayer and multilayer ReS2. *Physical Review B*, 95(16):2–7, 2017.

[18] Ipshita Datta, Sang Hoon Chae, Gaurang R. Bhatt, Mohammad Amin Tadayon, Baichang Li, Yiling Yu, Chibeom Park, Jiwoong Park, Linyou Cao, D. N. Basov, James Hone, and Michal Lipson. Low-loss composite photonic platform based on 2D semiconductor monolayers. *Nature Photonics*, 14(4):256–262, 2020.

[19] Hui Deng, Hartmut Haug, and Yoshihisa Yamamoto. Exciton-polariton Bose-Einstein condensation. *Reviews of Modern Physics*, 82(2):1489–1537, 2010.

[20] Hui Deng, Gregor Weihs, David Snoke, J. Bloch, and Yoshihisa Yamamoto. Polariton lasing vs. photon lasing in a semiconductor microcavity. *Proceedings of the National Academy of Sciences*, 100(26):15318–15323, dec 2003.

[21] S Dufferwiel, S Schwarz, F Withers, A A P Trichet, F Li, M Sich, O Del Pozo-Zamudio, C Clark, A Nalitov, D D Solnyshkov, G Malpuech, K S Novoselov, J M Smith, M S Skolnick, D N Krizhanovskii, and A I Tartakovskii. Exciton-polaritons in van der Waals heterostructures embedded in tunable microcavities. *Nature Communications*, 6(May):8579, 2015.

[22] Shanhui Fan and J. Joannopoulos. Analysis of guided resonances in photonic crystal slabs. *Physical Review B*, 65(23):1–8, 2002.

[23] Liang Fang, Qingchen Yuan, Hanlin Fang, Xuetao Gan, Juntao Li, Tao Wang, Qinghua Zhao, Wanqi Jie, and Jianlin Zhao. Multiple Optical Frequency Conversions in Few-Layer GaSe Assisted by a Photonic Crystal Cavity. *Advanced Optical Materials*, 6(22):1–7, 2018.

[24] Z. Fei, M. E. Scott, D. J. Gosztola, J. J. Foley, J. Yan, D. G. Mandrus, H. Wen, P. Zhou, D. W. Zhang, Y. Sun, J. R. Guest, S. K. Gray, W. Bao, G. P. Wiederrecht, and X. Xu. Nano-optical imaging of WS2 waveguide modes revealing light-exciton interactions. *Physical Review B*, 94(8):081402, 2016.

[25] Lucas C. Flatten, Zhengyu He, David M. Coles, Aurelien A. P. Trichet, Alex W. Powell, Robert A. Taylor, Jamie H. Warner, and Jason M. Smith. Room-temperature exciton-polaritons with two-dimensional WS2. *Scientific Reports*, (September):1–7, 2016.

[26] Michael D. Fraser, Sven Höfling, and Yoshihisa Yamamoto. Physics and applications of exciton-polariton lasers. *Nature Materials*, 15(10):1049–1052, 2016.

[27] Xue Tao Gan, Chen Yang Zhao, Si Qi Hu, Tao Wang, Yu Song, Jie Li, Qing Hua Zhao, Wan Qi Jie, and Jian Lin Zhao. Microwatts continuous-wave pumped second harmonic generation in few- and mono-layer GaSe. *Light: Science and Applications*, 7(1):1–6, 2018.

[28] Xuetao Gan, Yuanda Gao, Kin Fai Mak, Xinwen Yao, Ren Jye Shiue, Arend Van Der Zande, Matthew E. Trusheim, Fariba Hatami, Tony F. Heinz, James Hone, and Dirk Englund. Controlling the spontaneous emission rate of monolayer MoS2in a photonic crystal nanocavity. *Applied Physics Letters*, 103(18):1–5, 2013.

[29] Xuetao Gan, Kin Fai Mak, Yuanda Gao, Yumeng You, Fariba Hatami, James Hone, Tony F Heinz, and Dirk Englund. Strong enhancement of light-matter interaction in graphene coupled to a photonic crystal nanocavity. *Nano Letters*, 12(11):5626–5631, 2012.

[30] A. K. Geim and I. V. Grigorieva. Van der Waals heterostructures. *Nature*, 499(7459):419–425, 2013.

[31] Rahul Gogna, Long Zhang, and Hui Deng. Self-Hybridized Polarized Polaritons in ReS2 Crystals. *ACS Photonics*, 7(12):3328–3332, 2020.

[32] Rahul Gogna, Long Zhang, Zhaorong Wang, and Hui Deng. Photonic crystals for controlling strong coupling in van der Waals materials. *Optics Express*, 27(16):22700, 2019.

[33] Su-Hyun Gong, Filippo Alpeggiani, Beniamino Sciacca, Erik C. Garnett, and L. Kuipers. Nanoscale chiral valley-photon interface through optical spin-orbit coupling. *Science*, 359(6374):443–447, jan 2018.

[34] Jon Olav Grepstad, Martin M Greve, Bodil Holst, Ib-Rune Johansen, Olav Solgaard, and Aasmund Sudbø. Finite-size limitations on Quality factor of guided resonance modes in 2D photonic crystals. *Optics express*, 21(20):23640–54, 2013.

[35] Zuoli He and Wenxiu Que. Molybdenum disulfide nanomaterials: Structures, properties, synthesis and recent progress on hydrogen evolution reaction. *Applied Materials Today*, 3:23–56, 2016.

[36] C. H. Ho and C. E. Huang. Optical property of the near band-edge transitions in rhenium disulfide and diselenide. *Journal of Alloys and Compounds*, 383(1-2):74–79, 2004.

[37] J. J. Hopfield. Theory of the contribution of excitons to the complex dielectric constant of crystals. *Physical Review*, 112(5):1555–1567, 1958.

[38] Wei Ting Hsu, Li Syuan Lu, Dean Wang, Jing Kai Huang, Ming Yang Li, Tay Rong Chang, Yi Chia Chou, Zhen Yu Juang, Horng Tay Jeng, Lain Jong Li, and Wen Hao Chang. Evidence of indirect gap in monolayer WSe2. *Nature Communications*, 8(1):1–7, 2017.

[39] J. Jadczak, J. Kutrowska-Girzycka, T. Smoleński, P. Kossacki, Y. S. Huang, and L. Bryja. Exciton binding energy and hydrogenic Rydberg series in layered ReS 2. *Scientific Reports*, 9(1):1–9, 2019.

[40] I. V. Grigorieva K. S. Novoselov, A. K. Geim, S. V. Morozov, D. Jiang, Y. Zhang, S. V. Dubonos and A. A. Firsov. Electric Field Effect in Atomically Thin Carbon Films. 306(5696):666–669, 2016.

[41] Vadim Karagodsky, Bala Pesala, Christopher Chase, Werner Hofmann, Fumio Koyama, and Connie J Chang-hasnain. Monolithically integrated multi-wavelength VCSEL arrays using high-contrast gratings. *Optics Express*, 18(2):694–699, 2010.

[42] J. Kasprzak, M. Richard, S. Kundermann, A. Baas, P. Jeambrun, J. M. J. Keeling, F. M. Marchetti, M. H. Szymańska, R. André, J. L. Staehli, V. Savona, P. B. Littlewood, B. Deveaud, and Le Si Dang. BoseEinstein condensation of exciton polaritons. *Nature*, 443(7110):409–414, 2006.

[43] Rudolf F. Kazarinov and Charles H. Henry. Second-Order Distributed Feedback Lasers with Mode Selection Provided by First-Order Radiation Losses. *IEEE Journal of Quantum Electronics*, 21(2):144–150, 1985.

[44] S Kéna-Cohen, M Davanço, and S R Forrest. Strong exciton-photon coupling in an organic single crystal microcavity. *Physical Review Letters*, 101(11):116401, sep 2008.

[45] S. Klembt, T. H. Harder, O. A. Egorov, K. Winkler, R. Ge, M. A. Bandres, M. Emmerling, L. Worschech, T. C.H. Liew, M. Segev, C. Schneider, and S. Höfling. Exciton-polariton topological insulator. *Nature*, 562(7728):552–556, 2018.

[46] Duy Le, Alexei Barinov, Edwin Preciado, Miguel Isarraraz, Iori Tanabe, Takashi Komesu, Conrad Troha, Ludwig Bartels, Talat S. Rahman, and Peter A. Dowben. Spin-orbit coupling in the band structure of monolayer WSe2. *Journal of Physics Condensed Matter*, 27(18):1–6, 2015.

[47] Feng Li, L Orosz, O Kamoun, S Bouchoule, C Brimont, P Disseix, T Guillet, X Lafosse, M Leroux, J. Leymarie, M. Mexis, M. Mihailovic, G. Patriarche, F. Réveret, D Solnyshkov, J. Zuniga-Perez, and G Malpuech. From excitonic to photonic polariton condensate in a ZnO-based microcavity. *Physical Review Letters*, 110(19):1–5, 2013.

[48] Yilei Li, Yi Rao, Kin Fai Mak, Yumeng You, Shuyuan Wang, Cory R. Dean, and Tony F. Heinz. Probing symmetry properties of few-layer MoS2 and h-BN by optical second-harmonic generation. *Nano Letters*, 13(7):3329–3333, 2013.

[49] Xiaoze Liu, Wei Bao, Quanwei Li, Chad Ropp, Yuan Wang, and Xiang Zhang. Control of coherently coupled exciton-polaritons in monolayer tungsten disulphide. *Physical Review Letters*, 027403(July):027403, 2017.

[50] Xiaoze Liu, Tal Galfsky, Zheng Sun, Fengnian Xia, and Erh-chen Lin. Strong light-matter coupling in two-dimensional atomic crystals. *Nature Photonics*, 9(1):30–34, 2015.

[51] Z. S. Liu and R. Magnusson. Concept of multiorder multimode resonant optical filters. *IEEE Photonics Technology Letters*, 14(8):1091–1093, 2002.

[52] Boris Luk'yanchuk, Nikolay I Zheludev, Stefan a Maier, Naomi J Halas, Peter Nordlander, Harald Giessen, and Chong Tow Chong. The Fano resonance in plasmonic nanostructures and metamaterials. *Nature Materials*, 9(9):707–15, 2010.

[53] Robert Magnusson, Y Ding, K. J. Lee, D. Shin, P. S. Priambodo, P. P. Young, and T. A. Maldonado. Photonic devices enabled by waveguide-mode resonance effects in periodically modulated films. *Proceedings of SPIE, Nano- and Micro-Optics for Information Systems,*, 5225:20–34, 2003.

[54] K. F. Mak, K. L. McGill, J. Park, and P. L. McEuen. The valley hall effect in MoS2 transistors. *Science*, 344(6191):1489–1492, 2014.

[55] Kin Fai Mak, Changgu Lee, James Hone, Jie Shan, and Tony F. Heinz. Atomically thin MoS2: A new direct-gap semiconductor. *Physical Review Letters*, 105(13):2–5, 2010.

[56] Kin Fai Mak and Jie Shan. Photonics and optoelectronics of 2D semiconductor transition metal dichalcogenides. *Nature Photonics*, 10(4):216–226, 2016.

[57] Sajedeh Manzeli, Dmitry Ovchinnikov, Diego Pasquier, Oleg V. Yazyev, and Andras Kis. 2D transition metal dichalcogenides. *Nature Reviews Materials*, 2, 2017.

[58] C. F R Mateus, M. C Y Huang, Yunfei Deng, Andrew R. Neureuther, and Connie J. Chang-Hasnain. Ultrabroadband Mirror Using Low-Index Cladded Subwavelength Grating. *IEEE Photonics Technology Letters*, 16(2):518–520, 2004.

[59] Xianghai Meng, Yongjian Zhou, Ke Chen, Richard H. Roberts, Wenzhi Wu, Jung Fu Lin, Ray T. Chen, Xiaochuan Xu, and Yaguo Wang. Anisotropic Saturable and Excited-State Absorption in Bulk ReS2. *Advanced Optical Materials*, 6(14):1–8, 2018.

[60] David A. B. Miller. Optical physics of quantum wells.

[61] R.C. Miller and D.A. Kleinman. Excitons in GaAs Quantum Wells. *Journal of Luminescence*, 30:520–540, 1985.

[62] Thomas Mueller and Ermin Malic. Exciton physics and device application of two-dimensional transition metal dichalcogenide semiconductors. *npj 2D Materials and Applications*, 2(1):1–12, 2018.

[63] Battulga Munkhbat, Denis G Baranov, Michael Stührenberg, Martin Wersäll, Ankit Bisht, and Timur Shegai. Self-Hybridized Exciton-Polaritons in Multilayers of Transition Metal Dichalcogenides for Efficient Light Absorption. *ACS Photonics*, 6(1):139–147, 2019.

[64] Eunice Y Paik, Long Zhang, G William Burg, Rahul Gogna, Emanuel Tutuc, and Hui Deng. Interlayer exciton laser of extended spatial coherence in atomically thin heterostructures. *Nature*, 576(December), 2019.

[65] C. E. Platts, M. A. Kaliteevski, S. Brand, R. A. Abram, I. V. Iorsh, and A. V. Kavokin. Whispering-gallery exciton polaritons in submicron spheres. *Physical Review B - Condensed Matter and Materials Physics*, 79(24):1–6, 2009.

[66] David Rosenblatt, Avner Sharon, and Asher A. Friesem. Resonant grating waveguide structures. *IEEE Journal of Quantum Electronics*, 33(11):2038–2059, 1997.

[67] Emilie Sakat, Grégory Vincent, Petru Ghenuche, Nathalie Bardou, Christophe Dupuis, Stéphane Collin, Fabrice Pardo, Riad Haïdar, and Jean-Luc Pelouard. Free-standing guided-mode resonance band-pass filters: from 1D to 2D structures. *Optics Express*, 20(12):13082, 2012.

[68] J H Schmid, W Sinclair, J García, S Janz, J Lapointe, D Poitras, Y Li, T Mischki, G Lopinski, P Cheben, A Delâge, A Densmore, P Waldron, and D-X Xu. Silicon-on-insulator guided mode resonant grating for evanescent field molecular sensing. *Optics Express*, 17(20):18371–80, 2009.

[69] Sangwan Sim, Doeon Lee, Minji Noh, Soonyoung Cha, Chan Ho Soh, Ji Ho Sung, Moon Ho Jo, and Hyunyong Choi. Selectively tunable optical Stark effect of anisotropic excitons in atomically thin ReS2. *Nature Communications*, 7(May):1–6, 2016.

[70] Yu Song, Siqi Hu, Miao Ling Lin, Xuetao Gan, Ping Heng Tan, and Jianlin Zhao. Extraordinary Second Harmonic Generation in ReS2 Atomic Crystals. *ACS Photonics*, 5(9):3485–3491, 2018.

[71] Andrea Splendiani, Liang Sun, Yuanbo Zhang, Tianshu Li, Jonghwan Kim, Chi Yung Chim, Giulia Galli, and Feng Wang. Emerging photoluminescence in monolayer MoS2. *Nano Letters*, 10(4):1271–1275, 2010.

[72] Michael Stührenberg, Battulga Munkhbat, Denis G. Baranov, Jorge Cuadra, Andrew B. Yankovich, Tomasz J. Antosiewicz, Eva Olsson, and Timur Shegai. Strong Light-Matter Coupling between Plasmons in Individual Gold Bi-pyramids and Excitons in Mono- and Multilayer WSe2. *Nano Letters*, 18(9):5938–5945, 2018.

[73] C. Sturm, D. Tanese, H. S. Nguyen, H. Flayac, E. Galopin, A. Lemaître, I. Sagnes, D. Solnyshkov, A. Amo, G. Malpuech, and J. Bloch. All-optical phase modulation in a cavity-polariton Mach-Zehnder interferometer. *Nature Communications*, 5(May 2013):1–7, 2014.

[74] J Torres, D Coquillat, R Legros, J P Lascaray, F Teppe, D Scalbert, D Peyrade, Y Chen, O Briot, M. Le Vassor d'yerville, E Centeno, D Cassagne, and J P Albert. Giant second-harmonic generation in a one-dimensional GaN photonic crystal. *Physical Review B*, 69(8):1–8, 2004.

[75] Abin Varghese, Dipankar Saha, Kartikey Thakar, Vishwas Jindal, Sayantan Ghosh, Nikhil V. Medhekar, Sandip Ghosh, and Saurabh Lodha. Near-Direct Bandgap WSe2/ReS2 Type-II pn Heterojunction for Enhanced Ultrafast Photodetection and High-Performance Photovoltaics. *Nano Letters*, 20(3):1707–1717, 2020.

[76] Ruggero Verre, Denis G. Baranov, Battulga Munkhbat, Jorge Cuadra, Mikael Käll, and Timur Shegai. Transition metal dichalcogenide nanodisks as high-index dielectric Mie nanoresonators. *Nature Nanotechnology*, 14(7):679–683, 2019.

[77] P. M. Walker, L. Tinkler, M. Durska, D. M. Whittaker, I. J. Luxmoore, B. Royall, D. N. Krizhanovskii, M. S. Skolnick, I. Farrer, and D. A. Ritchie. Exciton polaritons in semiconductor waveguides. *Applied Physics Letters*, 102(1):1–5, 2013.

[78] G. Wang, X. Marie, B. L. Liu, T. Amand, C. Robert, F. Cadiz, P. Renucci, and B. Urbaszek. Control of Exciton Valley Coherence in Transition Metal Dichalcogenide Monolayers. *Physical Review Letters*, 117(18):1–5, 2016.

[79] Gang Wang, Alexey Chernikov, Mikhail M. Glazov, Tony F. Heinz, Xavier Marie, Thierry Amand, and Bernhard Urbaszek. Colloquium: Excitons in atomically thin transition metal dichalcogenides. *Reviews of Modern Physics*, 90(2):21001, 2018.

[80] Jun Wang, Marco Clementi, Momchil Minkov, Andrea Barone, Jean-François Carlin, Nicolas Grandjean, Dario Gerace, Shanhui Fan, Matteo Galli, and Romuald Houdré. Doubly resonant second-harmonic generation of a vortex beam from a bound state in the continuum. *Optica*, 7(9):1126, sep 2020.

[81] Qi Wang, Liaoxin Sun, Bo Zhang, Changqing Chen, Xuechu Shen, and Wei Lu. Direct observation of strong light-exciton coupling in thin WS_2 flakes. *Optics Express*, 24(7):7151, 2016.

[82] S S Wang and R Magnusson. Theory and applications of guided-mode resonance filters. *Applied optics*, 32(14):2606–2613, 1993.

[83] Shaojun Wang, Songlin Li, Thibault Chervy, Atef Shalabney, Stefano Azzini, Emanuele Orgiu, James A. Hutchison, Cyriaque Genet, Paolo Samorì, and Thomas W. Ebbesen. Coherent coupling of WS2 monolayers with metallic photonic nanostructures at room temperature. *Nano Letters*, 16(7):4368–4374, 2016.

[84] Zhaorong Wang, Rahul Gogna, and Hui Deng. What is the best planar cavity for maximizing coherent exciton-photon coupling. *Applied Physics Letters*, 111(6):061102, 2017.

[85] Zhaorong Wang, Bo Zhang, and Hui Deng. Dispersion engineering for vertical microcavities using subwavelength gratings. *Physical Review Letters*, 114(7):1–6, 2015.

[86] James L Webb, Lewis S Hart, Daniel Wolverson, Chaoyu Chen, Jose Avila, and Maria C Asensio. Electronic band structure of ReS2 by high-resolution angle-resolved photoemission spectroscopy. *Physical Review B*, 96(11):1–8, 2017.

[87] Guohua Wei, Teodor K Stanev, David A Czaplewski, Il Woong Jung, Nathaniel P Stern, Guohua Wei, Teodor K Stanev, David A Czaplewski, and Il Woong Jung. Silicon-nitride photonic circuits interfaced with monolayer MoS2 Silicon-nitride photonic circuits interfaced with monolayer MoS 2. 091112(2015), 2017.

[88] C. Weisbuch, M. Nishioka, A. Ishikawa, and Y. Arakawa. Observation of the coupled exciton-photon mode splitting in a semiconductor quantum microcavity. *Physical Review Letters*, 69(23):3314–3317, 1992.

[89] Fengcheng Wu, Timothy Lovorn, and A. H. Macdonald. Topological Exciton Bands in Moiré Heterojunctions. *Physical Review Letters*, 118(14):1–6, 2017.

[90] Fengcheng Wu, Timothy Lovorn, and A. H. Macdonald. Theory of optical absorption by interlayer excitons in transition metal dichalcogenide heterobilayers. *Physical Review B*, 97(3):1–10, 2018.

[91] Sanfeng Wu, Sonia Buckley, John R. Schaibley, Liefeng Feng, Jiaqiang Yan, David G. Mandrus, Fariba Hatami, Wang Yao, Jelena Vučković, Arka Majumdar, and Xiaodong Xu. Monolayer semiconductor nanocavity lasers with ultralow thresholds. *Nature*, 520(7545):69–72, 2015.

[92] Yu Ye, Zi Jing Wong, Xiufang Lu, Xingjie Ni, Hanyu Zhu, Xianhui Chen, Yuan Wang, and Xiang Zhang. Monolayer excitonic laser. *Nature Photonics*, 9(11):733–737, 2015.

[93] Hualing Zeng, Junfeng Dai, Wang Yao, Di Xiao, and Xiaodong Cui. Valley polarization in MoS 2 monolayers by optical pumping. *Nature Nanotechnology*, 7(8):490–493, 2012.

[94] Long Zhang, Rahul Gogna, G. William Burg, Jason Horng, Eunice Paik, Yu Hsun Chou, Kyounghwan Kim, Emanuel Tutuc, and Hui Deng. Highly valley-polarized singlet and triplet interlayer excitons in van der Waals heterostructure. *Physical Review B*, 100(4):1–6, 2019.

[95] Long Zhang, Rahul Gogna, Will Burg, Emanuel Tutuc, and Hui Deng. Photonic-crystal exciton-polaritons in monolayer semiconductors. *Nature Communications*, 9(1):1–8, 2018.

[96] Shuai Zhang, Qiuyu Shang, Wenna Du, Jia Shi, Zhiyong Wu, Yang Mi, Jie Chen, Fengjing Liu, Yuanzheng Li, Mei Liu, Qing Zhang, and Xinfeng Liu. Strong ExcitonPhoton Coupling in Hybrid InorganicOrganic Perovskite Micro/Nanowires. *Advanced Optical Materials*, 6(2):1–9, 2018.

[97] Tao Zhang, Bei Jiang, Zhen Xu, Rafael G. Mendes, Yao Xiao, Linfeng Chen, Liwen Fang, Thomas Gemming, Shengli Chen, Mark H. Rümmeli, and Lei Fu. Twinned growth behaviour of two-dimensional materials. *Nature Communications*, 7:1–7, 2016.

[98] Jiaxin Zhao, Rui Su, Antonio Fieramosca, Weijie Zhao, Wei Du, Xue Liu, Carole Diederichs, Daniele Sanvitto, Timothy C.H. Liew, and Qihua Xiong. Ultralow Threshold Polariton Condensate in a Monolayer Semiconductor Microcavity at Room Temperature. *Nano Letters*, 21(7):3331–3339, 2021.

[99] Bo Zhen, Chia Wei Hsu, Yuichi Igarashi, Ling Lu, Ido Kaminer, Adi Pick, Song-Liang Chua, John D. Joannopoulos, and Marin Soljačić. Spawning rings of exceptional points out of Dirac cones. *Nature*, 525(7569):354–358, 2015.